A MEASUREMENT OF NEUTRINO INDUCED NEUTRAL CURRENT NEUTRAL PION PRODUCTION CROSS SECTION WITH THE NOvA NEAR DETECTOR

A THESIS

Submitted to the
FACULTY OF SCIENCE
PANJAB UNIVERSITY, CHANDIGARH
for the degree of

DOCTOR OF PHILOSOPHY

2019

DAISY KALRA

DEPARTMENT OF PHYSICS
CENTRE OF ADVANCED STUDY IN PHYSICS
PANJAB UNIVERSITY
CHANDIGARH, INDIA

DEPARTMENT OF PHYSICS
Centre of Advanced Study in Physics
PANJAB UNIVERSITY, CHANDIGARH-160 014 (INDIA)
Fax: ++91-172-2783336
Phone: ++91-172-2541741
EPABX: ++91-172-2534466, 2534446
Email: casphypu.ac.in

CORRECTION CERTIFICATE

It is certified that there were no specific corrections recommended by the examiner of **Ms. Daisy Kalra** in her Ph.D. thesis **"A MEASUREMENT OF NEUTRINO INDUCED NEUTRAL CURRENT NEUTRAL PION PRODUCTION CROSS SECTION WITH THE NOvA NEAR DETECTOR".** The thesis submitted by **Ms. Daisy Kalra** in the present form, is acceptable.

(Prof. Navdeep Goyal)
Dept. of Physics,
P.U., Chandigarh
(Chairman)

Chairperson
Department of Physics
Panjab University
Chandigarh-160014

Vipin Bhatnagar
(Prof. Vipin Bhatnagar)
Department of Physics
P.U., Chandigarh
(Supervisor)

Ashok Kumar
(Dr. Ashok Kumar)
Department of Physics
P.U., Chandigarh
Supervisor)

Acknowledgements

First and foremost I give thanks to God for his blessings that I am able to complete my work successfully. I am deeply thankful to my supervisors Prof. Vipin Bhatnagar & Dr. Ashok Kumar for their continuous support and valuable advice. Thank you for guiding me to the successful completion of this thesis. It was a great learning experience to work under their supervision.

Thank you to Vishwamitter Sir, for always giving me the right advice at the right time. Thank you for your valuable time and teachings.

I am thankful to the Chairman of Department of Physics at Panjab University for providing adequate facilities to work in the department and providing me with a golden opportunity to spend three years of my research period in Fermi National Accelerator Laboratory, USA. Many thanks to the technical, computing and purchase section staff of Department of Physics and HEP office at Panjab University.

I would also like to extend my sincere thanks to Dr. John W. Cooper. Thanks for being a friendly supervisor. I consider myself very fortunate for being able to work with a very encouraging scientist like him. Thanks for all the motivation and valuable suggestions throughout my research. Thanks for your patience and time.

I am deeply thankful to Dr. Jonathan M. Paley and Dr. Mathew Muether for all the knowledgeable discussions through out my research work. It has been a great pleasure to work with both of you. Thank you for all the help and support you gave me. Working with all of you is the most educational and enjoyable experience of my life.

Thank you, to the NOvA Beam Group and NOvA Near Detector Group, and especially to Giulia, Alex, Leo, Linda, Robert Hatcher, Duyang, Jeremy, Shih-kai, Pengfei for all the help.

Also, I owe my thanks to the NOvA spokespersons Dr. Peter Shanahan, Dr. Mark Messier and Dr. Patricia Vahle and all the members of NOvA collaboration including physicists, engineers and technicians who work hard, day and night, to make it *successful. Thank you Etta and Stefani for taking care of all the arrangements in the lab.*

Thank you, to the Department of Science and Technology for the support given to the IIFC program.

I am thankful to my colleagues at Panjab University: Kanishka, Manisha, Ani, Ankita, Aman, Raman, Ruchi, Monika who helped me in one way or the other. I would also like to thank my friends whom I have met at Fermilab during my three and a half year of stay, Zuzana, Shiqi, Diana, Kanika, Erika, Cindy, Biswaranjan, Matt, Jose, Gavin, Reed and Alan.

Special thanks go to Manbir, Gary, Sofia, Ruchi, Jyoti, Cheryl, Chehlo, Simar for making five years of my Ph.D life so colorful and enjoyable.

Thank you, to Albert and his late wife Sonya, whom I have met in Fermilab. Thanks for loving me unconditionally. Thanks for always welcoming me into your home.

I am incredibly thankful for the constant support provided by my family throughout my academic and personal life. Thank you for your love and encouragement.

I thank my brother Chandan for his constant support in all phases of my life. Thank you so much for always being there whenever I need anything. This thesis would have been simply impossible without your support.

In retrospect, there are so many great people to give thanks to. Without them I would not have been able to come this far or complete this thesis. Though I cannot print out all the names, it is worthy noting that many great people helped me in different ways along this journey. I thank them all here.

May the Almighty God bless all of you.

Date: **(Daisy Kalra)**

Abstract

The NOvA experiment is a long baseline neutrino oscillation experiment that uses two functionally identical detectors. The NOvA near detector is situated at Fermilab and the NOvA far detector is located 810 km away in northern Minnesota. The NOvA near detector is used to study the production cross section of neutral current π^0 events. These events represent an important background for the experiments looking for electron neutrino appearance. So, it is important to constrain this background. The flux-averaged neutral current π^0 production cross-section is reported. We also report the differential cross-section w.r.t the final state neutral pion kinematics. Additionally, simulation studies are carried out where we look systematically at various ways to improve the neutrino yield for the NOvA off-axis experiment.

This work has been done in collaboration with the NOvA experiment but the analyses and results presented in this thesis are my contribution.

Contents

List of Figures

List of Tables

Chapter 2

Neutrino Interactions

Neutrinos interact via exchange of $W^{\pm}$ and Z^0 boson which are named as CC and NC interactions respectively. The study of neutrino interactions has always been a challenging task because of its tiny cross section. Cross section is defined as the probability of neutrino interaction in a target material. Studying and understanding these interactions are very important as they play a vital role in making precise measurement of neutrino oscillation parameters [32]. The uncertainties associated to the neutrino interactions cross section are amongst the dominant uncertainties on the neutrino oscillation results. So, to reduce the level of uncertainties to a few percent the neutrino experiments make these measurements. Most of the long baseline experiments for oscillation studies such as NOvA (detector details are in chapter 3) use two detector technology where near detector (ND) is used to measure the neutrino un-oscillated flux due to its close proximity to the target source and far detector (FD) is used to study the oscillated beam. Starting with a beam of almost pure muon neutrinos, the number of neutrinos N_{ν_e} at FD is given by:

$$N_{\nu_e}^{FD} \sim P_{\nu_\mu \to \nu_e} \frac{\sigma_{\nu_e}^{FD} \epsilon_{\nu_e}^{FD}}{\sigma_{\nu_\mu}^{ND} \epsilon_{\nu_\mu}^{ND}} N_{\nu_\mu}^{ND}, \tag{2.1}$$

where $P_{\nu_\mu \to \nu_e}$ is the appearance probability, $\sigma_{\nu_e}^{FD}$ ($\sigma_{\nu_\mu}^{ND}$) is the ν_e (ν_μ) interactions cross section, $\epsilon_{\nu_e}^{FD}$ ($\epsilon_{\nu_\mu}^{ND}$) is the efficiency of reconstructing ν_e (ν_μ) events in FD (ND) and $N_{\nu_\mu}^{ND}$ is the number of ν_μ at ND.

The larger uncertainties on the neutrino interactions cross section would impact the far detector prediction of $N_{\nu_e}^{FD}$. Though, most of the uncertainties get canceled in the ratio of FD to ND because of having similar detector technology for both of the detectors but not all of them. So, understanding the neutrino interactions cross section could help reduce the uncertainties on the neutrino oscillation measurements and thus able to make a precise measurement of the oscillation parameters (Δm^2, δ_{CP} and θ_{13}) which is the main goal of the current and future generation neutrino oscillation experiments.

2.1 Neutrino-nucleus (ν-N) interactions

Most of the neutrino oscillation experiments detect neutrinos via ν-nucleus interactions. Since nucleus is composed of nucleons so when an energetic beam of neutrinos, with energy in range of 0.1-20 GeV, collide with a fixed target then ν interacts with nucleons in the nucleus. There are several neutrino experiments that make cross-section measurements in this energy range to reduce the uncertainties on the existing measurements [16]. NOvA is one of them that focus in 1-3 GeV energy region. In this intermediate energy range, neutrino interactions with the nucleons inside the nucleus are broadly classified into two types: elastic and inelastic interactions.

1. **Elastic interactions:** Neutrinos can elastically scatter off an entire nucleon and result in an ejection of the target nucleon (or multiple nucleons). The interaction happens via exchange of Z^0 boson (NC interaction).

   In case of CC interactions, where neutrinos have sufficient energy to create an associated lepton, these are termed as Quasi-Elastic (QE) interactions. The

Feynman diagrams to represent the Elastic and QE interactions are shown in Figure 2.1.

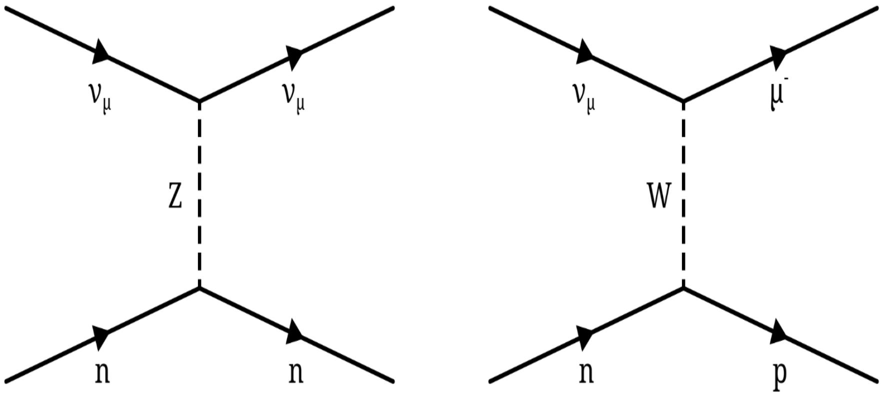

Figure 2.1: Feynman diagrams showing elastic (left) and quasi-elastic (right) interactions.

2. **Inelastic interactions:** At higher energies neutrinos undergo inelastic interactions. These are through the resonance (RES) production in the low momentum transfer region and deep inelastic scattering (DIS) in the high momentum transfer region.

   In the RES production, neutrinos can excite the target nucleon to a resonance state (baryonic resonance) which then decays to nucleons and mesons most often a pion (or multiple pions). At even higher energies, E>10 GeV, it is possible for neutrinos to probe an individual quark constituents. This type of interaction is termed as DIS where neutrino can scatter off any of the quarks inside the nucleon and results in hadronic shower. The Feynman diagrams to represent the resonance and DIS interactions are shown in Figure 2.2.

However, most of the neutrino oscillation experiments use targets made up of heavier nuclei, bound state of nucleons. So, the processes are quite complicated in reality. Earlier, experiments used deuterium as a target in some of the neutrino

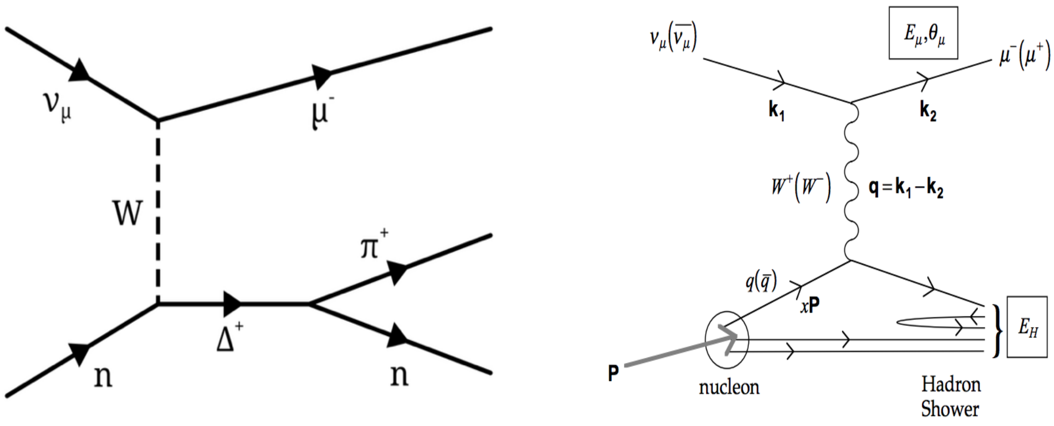

Figure 2.2: Feynman diagrams showing the inelastic interactions through the resonance (RES) production (left) and deep inelastic scattering (DIS) (right).

experiments but the measurements were statistically limited. So, to obtain higher interaction rates, particularly in the FD, the experiments make use of the heavier nuclei such as Carbon, Oxygen (Water), Argon, Iron. But the fact that the nucleons are contained within the nucleus significantly complicates the interaction observed in the detector.

The simpler model to explain the interactions within the nucleus is the “Fermi Gas” model which assumes the nucleus as a degenerate gas of nucleons. Nucleons inside the nuclear potential are constantly moving around imparting a boost to the interacting system that is not very well known and that results in rapid change in the energy and the direction. The energy and the direction of nucleons w.r.t the incoming neutrino further affects the kinematics of any interaction and their cross section. This effect is dominant at the lower neutrino energies where momentum transfer is low. Unfortunately, the initial momentum spectra of nucleons is not very well known. Most of the experiments in the past had used relativistic fermi gas (RFG) [33] model a.k.a. Global Fermi Gas model, the simple approach where nucleus is treated as a box of constant nuclear density. The modern approach used by the current generation experiments make use of “Spectral functions (SF)” (Local Fermi Gas model) [34] where nuclear density is defined as a function of distance from the center of nucleus which then affects the momentum distribution. The momentum distributions for the RFG and SF are shown in Figure 2.3.

As the target with which neutrino interacts also include correlated nucleon pairs. So, the momentum distribution can be further modified by taking into account the short-range correlations between the nucleons [35]. When the nucleons are very close to each other then the strong short-range forces increase their momentum thus modifying the momentum distribution.

After the neutrino interacts with the nucleus, the produced final state particles then propagate out through the nucleus where they undergo several strong interactions with other nucleons in the nuclear environment. These are referred to as "Final State Interactions (FSI)" and they significantly change the momentum/energy and direction of the final state particles. This effect is more important at lower neutrino energies and can be largely ignored at the higher neutrino energies where DIS dominates. These interactions include elastic and inelastic re-scattering, charge exchange, absorption (mesons, mostly pions, get absorbed in the nuclear medium and never escape the nucleus). It changes the type, number and kinematics of the final state particles. So, the particles that leave the nucleus can be altogether different than the ones produced at the interaction vertex.

All of these nuclear effects can significantly alter the topology of a particular interaction and so are very important to understand for making any cross-section measurement.

Figure 2.4 shows our current knowledge of the total neutrino and anti-neutrino interactions cross section as a function of neutrino energy. The neutrino cross sections are well measured in the high energy region but not in the low energy region. This is due to lack of high statistics data in this energy region. The situation even worsens in case of anti-neutrino cross sections due to low statistics and larger background contamination. These days there are many experiments like MINERvA, T2K, SciBooNE, MicroBooNE going on to make a measurement in the intermediate energy region in greater detail. The region of interest for the NOvA is 1-3 GeV where, the

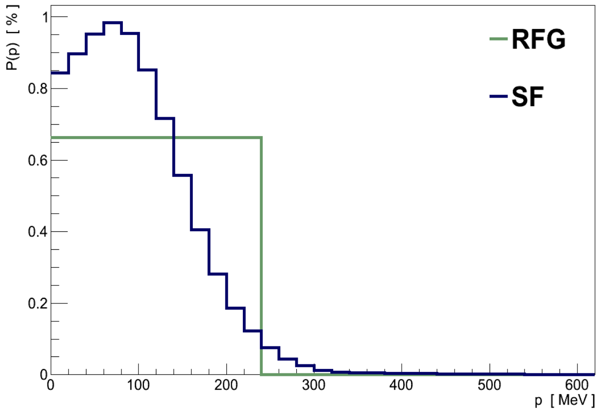

Figure 2.3: The momentum distributions of nucleons with relativistic Fermi-gas (RFG) model and spectral function (SF).

Elastic/QE, RES and DIS processes are competing with each other. As a result of which, the products of neutrino interactions include a variety of final states including pions, kaons and collection of mesons. A proper understanding of the final state particles is important to understand the nuclear effects as it holds the information of the type of interaction.

The next section lays out the details of neutrino induced NC π^o production on

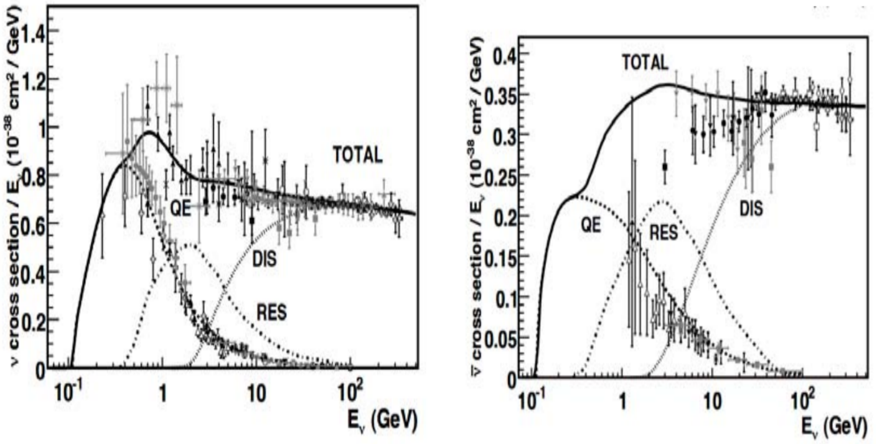

Figure 2.4: Total neutrino (left) and anti-neutrino (right) CC interaction cross section as a function of energy.

which the detailed analysis has been performed. There are various Monte Carlo generators used to model these neutrino interactions but here we specifically discuss the GENIE Monte Carlo generator [36] which is used in the NOvA Experiment.

2.2 Neutrino Induced NC π^o Production

Neutrino induced NC interactions with a π^o in the final state represents a significant background in the experiments that look for ν_e appearance such as NOvA. A ∼10% uncertainty on the NC background for the NOvA ν_e appearance is dominated by π^o production [37] as is shown in Figure 2.5. There are a very few measurements of the NC π^o production cross-section that exists with large uncertainties. So, it is important to constrain this background. Neutral pion production in the region of interest of NOvA is dominated by RES interactions followed by DIS and coherent interactions.

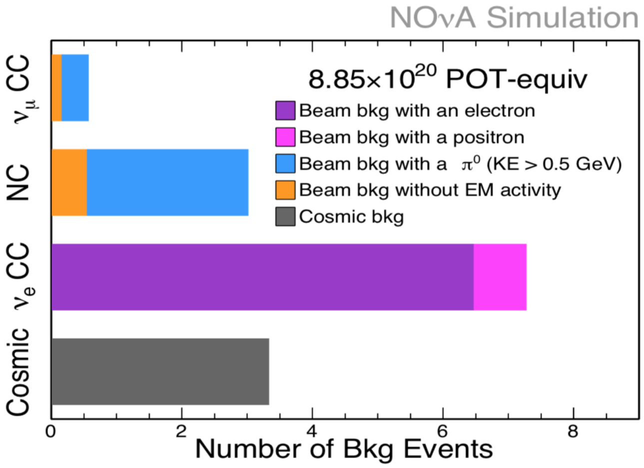

Figure 2.5: Plot shows the NOvA ν_e appearance backgrounds.

2.2.1 Resonant pion production:

The dominant process for the neutral pion production is through resonance production where nucleon is excited to the baryonic resonance state (Δ^{++} resonance) which then decays to nucleon and mesons (mostly pions). Resonance interactions dominate for the neutrinos of energy range 0.5-3.0 GeV. There are four neutrino and anti-neutrino induced NC channels that produce π^o in final state:

$$\begin{aligned} &\nu_\mu p \rightarrow \nu_\mu p \pi^o \\ &\bar{\nu_\mu} p \rightarrow \bar{\nu_\mu} p \pi^o \\ &\nu_\mu n \rightarrow \nu_\mu n \pi^o \\ &\bar{\nu_\mu} n \rightarrow \bar{\nu_\mu} n \pi^o . \end{aligned} \tag{2.2}$$

The model used in GENIE to describe the resonant π^o production is Rein and Sehgal (RS) model [38]. The production cross section of a single resonance is given as:

$$\frac{d\sigma}{dq^2 d\nu} = \frac{1}{32\pi m_N E_\nu^2} . \frac{1}{2} \sum_{spins} |\mathcal{M}(\nu\mathcal{N} \rightarrow \nu\mathcal{N}^*|^2 \left[\frac{1}{2\pi} . \frac{\Gamma}{(W - m_{N^*})^2 + \Gamma^2/4} \right], \tag{2.3}$$

where the factor in squared brackets is a Breit-Wigner function for a resonance of mass m_{N^*}, width Γ and observed mass W and $|\mathcal{M}|$ represents the amplitude that contains the dynamics of the process which in this case is described as an interaction of two currents, hadronic current (J_L^μ) and leptonic current (J_μ^N) such as:

$$\mathcal{M}(\nu\mathcal{N} \rightarrow \nu\mathcal{N}^*) = \frac{G_F \cos\theta_C}{\sqrt{2}} J_L^\mu J_\mu^N , \tag{2.4}$$

$$\mathcal{M}(\nu\mathcal{N} \rightarrow \nu\mathcal{N}^*) = \frac{G_F \cos\theta_C}{\sqrt{2}} [\bar{u}_\nu(k') \gamma^\mu (1 - \gamma_5 u_\nu(k))] \langle \mathcal{N}^* | \, J_\mu^N \, | \mathcal{N} \rangle , \tag{2.5}$$

where $G_F \cos\theta_C$ is the weak coupling constant.

2.2.2 Deep Inelastic Pion Production

The neutrinos with enough energy can scatter off an individual quark inside the nucleon and produce mesons mostly pions. Thus, the interactions at DIS scale are capable of revealing the internal structure of the target. An example of the Feynman diagram for DIS interaction is shown in Figure 2.2 (right). DIS processes, in general, are described by three dimensionless kinematic variables - Energy transfer (ν), Inelasticity (y) and Bjorken scaling variable (x) which are written as:

$$\begin{aligned} \nu &= \frac{p.q}{M} \\ y &= \frac{p.q}{p.k_1} \\ x &= \frac{Q^2}{2p.q}, \end{aligned} \tag{2.6}$$

where p is the four-momentum of the stuck nucleon, q is the momentum difference that is carried by the exchange boson, M is mass of the nucleon and Q^2 is negative square of four-momentum transferred ($-q^2$). The momentum carried by the particles and their direction are shown in Figure 2.2 (right). These equations are derived specifically for the CC-DIS interactions. In NC interactions, where the neutrino is not reconstructed, all the information of the event must be in the hadron shower. The kinematic quantities are identical to the CC case up to small effects due to muon mass [39].

The inclusive cross-section using the variables defined above is written as [40]:

$$\frac{d^2\sigma}{dxdy} = \frac{G_F^2 M E_\nu}{\pi(1+Q^2/M_Z^2)^2}\left[A.2xF_1(x,Q^2) + BF_2(x,Q^2) \pm C.xF_3(x,Q^2)\right], \tag{2.7}$$

where

$$A = \frac{y^2}{2}$$

$$B = (1 - y - \frac{Mx.y}{2E}) \tag{2.8}$$

$$C = y(1 - \frac{y}{2}).$$

In equation 2.7, G_F is the Fermi's weak coupling constant, M_Z is the mass of Z^0 boson and +(-) sign in the last term refers to the neutrino (anti-neutrino) interactions. $F_i(x, Q^2)$, i=1, 2, 3, are the dimensionless nucleon structure functions which carry information about the internal structure of the target.

2.2.3 Coherent Pion Production

In the Coherent process, a neutrino interacts with an entire nucleus as a whole instead of its individual nucleons and results in the production of neutral mesons (mainly π^o) such as:

$$\nu_l A \to \nu_l \pi^o A. \tag{2.9}$$

The coherent pion production is mainly characterized by a small momentum transfer (Q^2) to the nucleus which would not be sufficient to break the nucleus into its fragments. These low (Q^2) interactions produce events with a very forward going pion w.r.t the incoming neutrino direction. GENIE uses RS model to describe the cross section of the coherent pion production. In RS model, the differential cross section is written w.r.t Bjorken variable (x), inelasticity (y) and Lorentz invariant quantity t and is given as [41]:

$$\frac{d^3\sigma(\nu A \to \nu A\pi)}{dxdydt} \sim \frac{G_F^2}{2\pi^2} f_\pi^2 E(1-y) \frac{1}{16\pi}[\sigma_{tot}^{\pi\mathcal{N}}]^2(1+r^2)\left(\frac{m_A^2}{Q^2+m_A^2}\right)^2 e^{-b|t|}F_{abs}, \quad (2.10)$$

where G_F is fermi constant, f_π represents pion decay constant, E is neutrino energy, $\sigma_{tot}^{\pi\mathcal{N}}$ is the total cross section of the scatterer, r is nuclear radius and $e^{-b|t|}F_{abs}$ represents the nuclear form factor. There is also a propagator term $(1+Q^2/m_A^2)^{-2}$ with m_A =1 GeV which is included to extrapolate the cross section for the non-zero values of Q^2.

RS model used many approximations to derive the cross-section formula which makes this model simple and elegant. Due to its simplicity, this model is widely used for different nuclei and pion energies. It is worth mentioning that several improvements were made in this model which includes the non-vanishing muon mass terms for $Q^2 < 0.1GeV^2$ which further affects only CC channel [41].

2.2.4 Existing Measurements

There exist a very few measurements for the NC π^o production cross section. Most of these measurements are reported in the form of ratios of NC to CC cross section. Table 2.1 shows the ratio measurements for the resonant NC π^o production cross section to their CC counterparts.

SciBooNE has reported the ratio measurement of inclusive NC π^oproduction to the total CC cross section using a polystyrene target (C_8H_8) [47]:

$$\frac{\sigma(NC\pi^o)}{\sigma(\nu_\mu CC)} = 0.077 \pm 0.005_{stat} \pm 0.005_{syst}. \quad (2.11)$$

Additional measurement comes from K2K experiment where the ratio of NC single

Table 2.1: Cross-section ratio measurement of the RES NC π^o production to its CC counterpart.

Experiment	Target	Channel	Value	Reference
ANL	H_2, D_2	$\frac{\sigma(\nu_\mu p \rightarrow \nu_\mu p \pi^o)}{\sigma(\nu_\mu p \rightarrow \mu^- p \pi^+}$	0.51±0.25	[42]
ANL	H_2, D_2		0.09±0.05	[43]
GGM	propane/freon		0.22±0.04	[44]
GGM	propane/freon	$\frac{\sigma(\nu_\mu p \rightarrow \nu_\mu p \pi^o)+\sigma(\nu_\mu n \rightarrow \nu_\mu n \pi^o)}{2\sigma(\nu_\mu n \rightarrow \mu^- p \pi^o}$	0.45±0.11	[45]

π^o production cross section to the total CC cross section is reported [46]:

$$\frac{\sigma(NC1\pi^o)}{\sigma(\nu_\mu CC)} = 0.064 \pm 0.001_{stat} \pm 0.007_{syst}. \tag{2.12}$$

MiniBooNE has provided the first absolute cross section for NC π^o production on CH_2 target using neutrino and anti-neutrino beam with energy peaked at 808 MeV and 664 MeV respectively [48]:

$$\begin{aligned} \sigma(\nu_{induced}) &= (4.76 \pm 0.05_{stat} \pm 0.76_{syst}) \times 10^{-40} cm^2/nucleon \\ \sigma(\bar{\nu}_{induced}) &= (1.48 \pm 0.05_{stat} \pm 0.23_{syst}) \times 10^{-40} cm^2/nucleon. \end{aligned} \tag{2.13}$$

MiniBooNE has also reported the differential measurements w.r.t π^o kinematics [48].

Recently, T2K has reported a measurement of the single π^o production rate in NC neutrino interactions on water [49] as well as ratio of measured to the expected production rate with mean neutrino energy 0.6 GeV:

$$\begin{aligned} \text{Measured Signal Events} &= 106 \pm 41_{stat} \pm 69_{syst} \\ \frac{Measured}{Expected} &= 0.68 \pm 0.26 \pm 0.44. \end{aligned} \tag{2.14}$$

2.3 Summary

In this chapter, the basics of neutrino-nucleon and neutrino-nucleus interactions are discussed. The GENIE theoretical models for the NC π^o production cross section, on which the analysis is performed, are discussed along with the existing measurements for this channel. In this thesis, NC π^o production cross section is measured using the NOvA near detector so in the next chapter, the experimental details of the NOvA detectors are discussed.

Chapter 3

The NOvA Experiment

The NOvA experiment is a long baseline experiment designed to study ν_e appearance and ν_μ disappearance with two detectors, the NOvA near detector (ND) at Fermilab and the NOvA far detector (FD) situated 810 km away in northern Minnesota. The NOvA uses an almost pure beam of ν_μ, with an energy peaked around 2 GeV, produced at Fermilab. The primary physics goals of the NOvA experiment is to resolve neutrino mass ordering/hierarchy problem, search for the CP violating phase (δ_{CP}), determine the θ_{23} octant as well as precise determination of oscillation parameters by measuring neutrino appearance and disappearance probability using the equations 1.9, 1.10 and 1.11 from chapter 1. This chapter lays out the experimental details of the NuMI beam-line based NOvA detectors.

3.1 The NuMI beam-line

The NOvA experiment makes use of the NuMI neutrino beam which is an intense beam of neutrinos (ν_μ) of variable energy ranging from 2-20 GeV. It was originally built to provide neutrinos to the MINOS experiment [50] that studied neutrino oscillations in both disappearance and appearance channels. A variety of different other neutrino experiments e.g MINERvA [51], ArgoNeuT [52] and MINOS+ [53]

also use the NuMI neutrino beam.

The NuMI is a tertiary beam resulting from the decay of many short-lived particles such as pions and kaons which are produced inside the NuMI target. In this section, the details of the NuMI neutrino beam production are discussed.

3.1.1 Fermilab Accelerator Complex

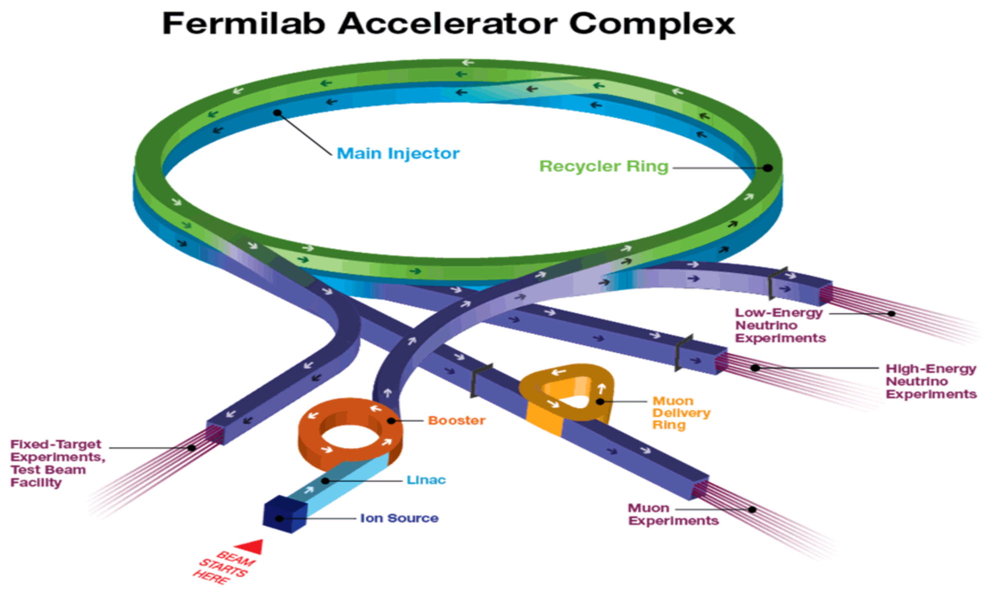

Figure 3.1: A schematic diagram of Fermilab Accelerator Complex.

In Fermilab's Accelerator Complex as shown in Figure 3.1, a series of accelerators (Linear Accelerator (LINAC), Booster, Recycler and Main Injector (MI)) work together in association to produce an energetic beam of protons [54]. Two main accelerator rings, the Booster and the MI, produce two primary proton beams - a low energy (8 GeV) proton beam from the Booster and a high energy (120 GeV) proton beam from the MI. Protons are originally produced as H^{-1} ions which are accelerated and bunched together to form a beam inside radio frequency generator. The LINAC accepts the particle beam at 750 keV and accelerates it up to 400 MeV to inject it into the Booster. The Booster further accelerates the beam to produce a low energy primary proton beam at 8 GeV. Protons from the Booster are then transferred to the MI via Recycler storage ring. One of the MI tunnel that was previously used as an anti-protons storage ring is now converted to proton ring so as to use it as a pre-injector to the MI. Protons in the MI are then accelerated to 120 GeV, a high energy primary proton beam from where they are extracted and bent towards the target station. The beam direction was originally defined using Global Positioning System (GPS) [55]. The beam in this configuration delivers a beam power of 350 kW [55]. Several improvements are made for NuMI and NOvA to increase the beam power to 700 kW and are mentioned below.

1. **Reduction of the MI cycle time:** The MI cycle time was reduced from 2.2 seconds to 1.33 seconds by adding two additional RF cavities that increased the accelerator rate of the proton beam [54].

2. **Slip Stacking Technique:** This technique allows the number of protons per cycle to be increased by adopting a different way to feed the proton beam into the MI and is done using two RF systems. This method is used to inject the protons from the Recycler storage ring to the MI where six batches, each with 4×10^{20} protons, are injected from the Booster to the Recycler one after the other followed by six more but in different orbit which differs by their momentum. Once all the six batches have twice the number of protons, the beam is then extracted in a single turn from the Recycler to the MI where the beam is accelerated to 120 GeV.

3.1.2 Production of the NuMI beam

Figure 3.2 shows a sketch of the NuMI beam-line where a high energy (120 GeV) primary proton beam, extracted from the MI, hits the NuMI target which is made up of graphite. Before colliding with the target, the beam passes through a specially designed device made up of graphite, referred to as the baffle. The beam then collides with the NuMI target resulting in the production of many short-lived secondary particles such as pions and kaons. These particles are focused by a set of two magnetic horns, Horn1 and Horn2. The focused secondary particles are directed towards a decay pipe filled with He where these particles decay to muons and ν_μ. The beam then passes through a beam absorber and rock material that removes the remaining muons, hadrons and other charged particles and leave an almost pure neutrino beam.

In the end, we get an almost pure beam of neutrinos (anti-neutrinos) with positive (negative) horn current. Depending on the polarity of horn current, there are two beam configurations - forward horn current (FHC, +200kA) and reverse horn current (RHC, -200kA) (details are in next chapter). In the FHC beam configuration, NuMI produces an almost pure beam of ν_μ - 94.1 % (93.8 %) composition of ν_μ for the NOvA FD (ND). The wrong sign contamination from $\bar{\nu}_\mu$ is 4.9% (5.3%) for the NOvA FD (ND) and from $(\nu_e + \bar{\nu}_e)$, composition is 1.0%(0.9%) for the NOvA FD (ND).

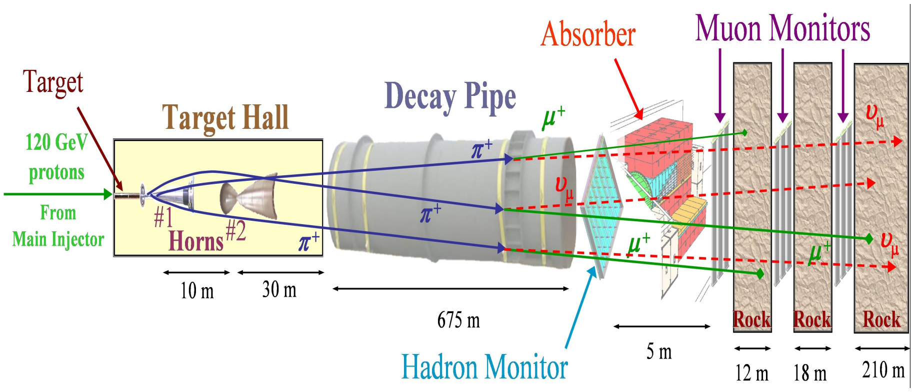

Figure 3.2: A sketch of the NuMI beam-line. A proton beam from the MI hits the target from the left side.

In the RHC beam configuration, where the NuMI produces an anti-neutrino enhanced beam, the wrong sign contamination from the ν_μ is 11.3% (11.7%) for the NOvA FD (ND).

It is very important to operate the detectors both in FHC and RHC beam configurations, to collect the data in neutrino and anti-neutrino mode, for accurately measuring the neutrino oscillation parameters and resolving the various neutrino puzzles [56].

3.1.3 An Off-Axis Concept

The NOvA detectors are placed 14.8 milliradians off-axis from the NuMI neutrino beam [54]. The off-axis choice is made studying the decay kinematics of pions and kaons. In the rest frame, these hadrons decay isotropically and produce mono-energetic neutrinos ($\pi, K \rightarrow \mu + \nu$) and their energy in the lab frame is calculated using relativistic kinematics and is shown below:

$$E_\nu = \frac{1 - (m_\mu/m_\pi)^2 E_\pi}{1 + \gamma^2 \tan^2\theta} \tag{3.1}$$

Using small angle approximation and the rest mass of muon and pion, the above equation can be re-written in the following way:

$$E_\nu = \frac{0.43 E_\pi}{1 + \gamma^2\theta^2} \tag{3.2}$$

where θ is the angle between incoming meson and outgoing neutrino, E_π is the energy of pion and $\gamma = \frac{1}{\sqrt{1-\beta^2}}$.

If the detector is placed on-axis for $\theta = 0$, E_ν increases with E_π as per equation 3.2. However, E_ν is relatively flat across a broad range of pion energies with the off-axis location of the detector and is illustrated in Figure 3.3 (left). The chosen NOvA off-axis position of 14.8 milliradians selects quasi mono-energetic neutrino beam of 2 GeV in energy, where it gives the highest probability of oscillations at the NOvA FD

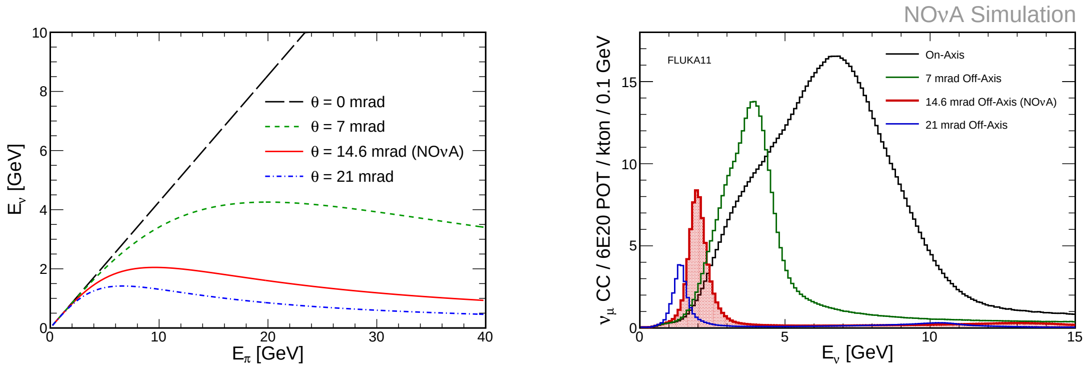

Figure 3.3: (Left) The energy of the neutrinos produced at an angle θ relative to the pion direction as a function of pion energy. (Right) The neutrino true energy spectra for ν_μCC interactions, for the NOvA FD positioned at various angles w.r.t the NuMI neutrino beam.

with a baseline of 810 km and is shown in red spectrum in Figure 3.3 (Right) [54].

Furthermore, two significant backgrounds are reduced by choosing an off-axis position for the detectors. The first is the neutral current background where the outgoing lepton is not observed. The topology of NC events where a π^o decays to two photons ($\pi^o \rightarrow \gamma\gamma$) can fake the electron showers produced by ν_e CC events. As neutrinos carry much of the event energy away, higher energy neutral current events can shift down into the expected signal region. With the off-axis narrow band beam in the signal region (1-3 GeV energy range) with a reduced high energy tail, much of the neutral current background shifts below the signal region as shown in Figure 3.4 [54].

Another important background is the intrinsic ν_e component of the NuMI neutrino beam which comes from the muon and pion decay. These neutrinos have broad energy distribution described by three-body decay kinematics relative to the $\nu_\mu' s$ produced by two-body decays and is shown in Figure 3.4 [54]. The relative narrow signal of ν_e appearance compared to the ν_e beam, when the detector is off-axis, is an additional advantage.

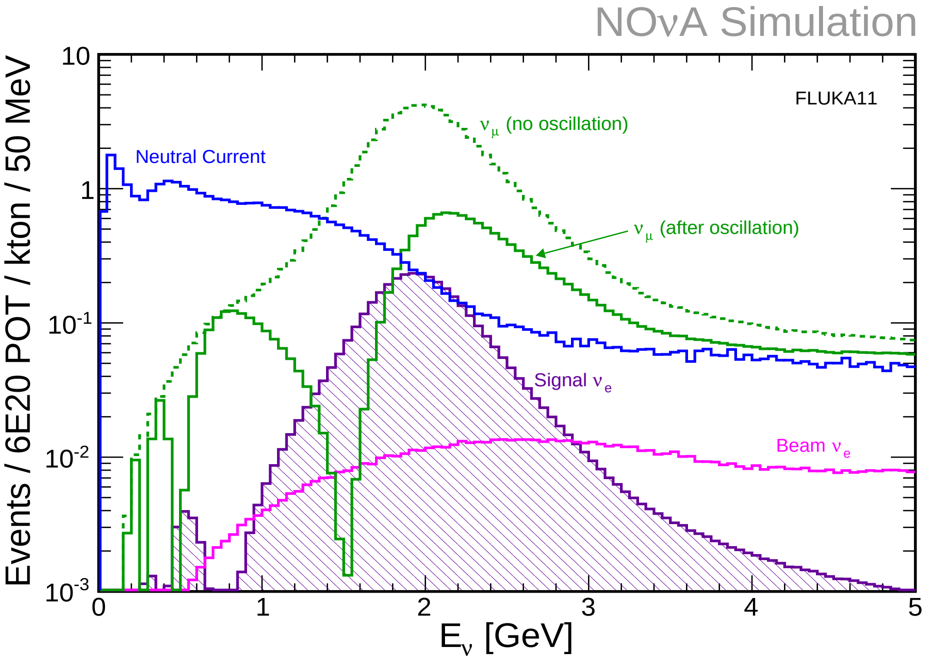

Figure 3.4: Simulated energy distributions for the ν_e oscillation signal, intrinsic beam ν_e events, NC events and ν_μ CC events with and without oscillations.

3.2 The NOvA Experimental Details

The NOvA experiment studies neutrino oscillations using two functionally identical detectors. The NOvA ND is located 1.2 km away from the target station at Fermilab and the NOvA FD is located 810 km away in northern Minnesota, a schematic of which is shown in Figure 3.5. Both the detectors are located off-axis from the NuMI neutrino beam (shown as a solid yellow line in the Figure). Since both the detectors are functionally identical, this feature helps to reduce the beam/flux related systematics in the oscillation measurements as also seen in equation 2.1 from chapter 2.

The basic unit of the NOvA detectors is a polyvinyl chloride (PVC) plastic cell which is filled with liquid scintillator. There is an emission of scintillation light when a charged particle passes through the medium and is collected by wavelength shifting (WLS) fibers. The light is then routed to the avalanche photo-diode (APD) for further read-out by the use of electronics. This is the basic design of the NOvA detectors and below the specifications for the NOvA ND and FD are described.

The NOvA PVC cells are extruded in the form of tube-like cells with a cross-section of 4 cm × 6 cm (cell width × cell depth) as shown in Figure 3.6. The cell width and depth defines the granularity of the NOvA detectors. Throughout the cells, there is a highly reflective material titanium dioxide, TiO_2, that is 90% reflective for 430 nm wavelength light. The pairs of 16 cell extrusions are glued together to form a module with 32 cells and these modules provide structural support for the detectors. The modules are stacked to form a "plane", which is simply a layer of cells. There are alternate planes of horizontally and vertically oriented cells that allows for the 3D reconstruction of particle position. Vertical planes form the "top-view" (XZ view) of the detector and horizontal planes form the "side-view" (YZ view) of the detector.

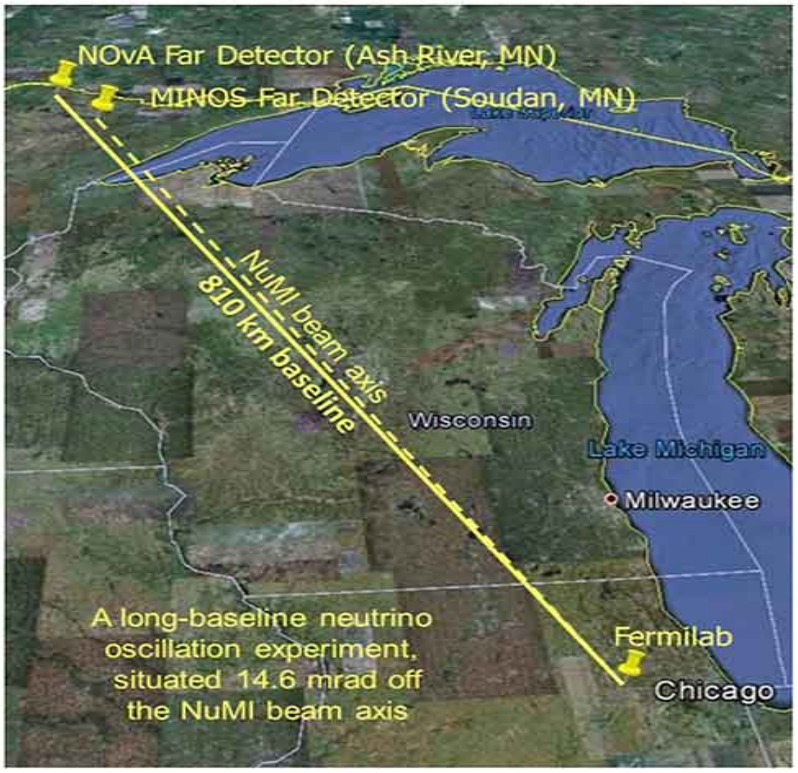

Figure 3.5: Figure showing locations of the NOvA ND and FD. The NOvA ND is located at Fermilab and the NOvA FD is located 810 km away in northern Minnesota.

Further, a larger unit ”block” is formed by gluing 32 planes together.

The PVC plastic cell extrusions are filled with liquid scintillator, that comprises 62% of the total mass of the NOvA detectors. The NOvA scintillator is 92.63% mineral oil and 5.23% pseudocumene, a scintillating agent, 0.14% PPO (waveshifter) and 0.0016% bis-MSB (waveshifter). The scintillator also contains an anti-static agent, 0.001% Stadis-425, that helps to prevent risk of fire hazard from charge build-up and sparking during filling. Additionally, Vitamin E is added as an anti-oxidant to prevent yellowing of scintillator [54]. When a charged particle passes through a cell scintillation light is produced in the near ultraviolet region (360-390 nm), shifted to the visible region of 400-450 nm with the use of wave-shifters.

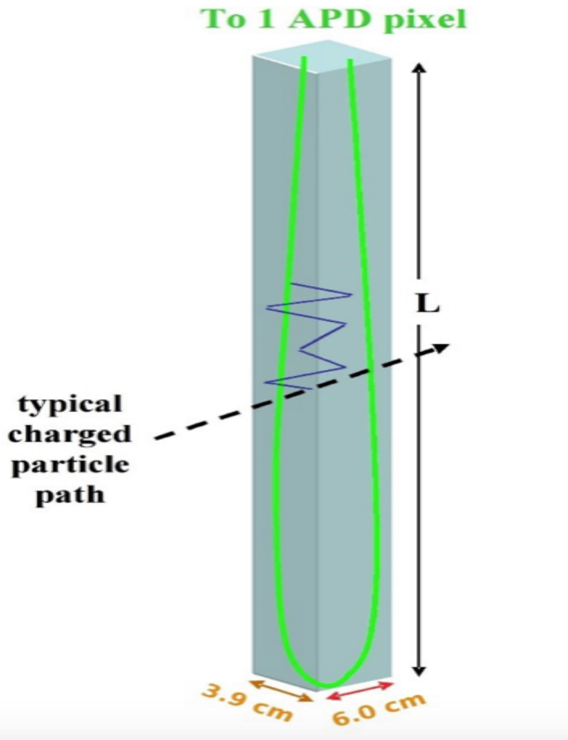

Figure 3.6: Figure showing a plastic PVC cell with a wavelength shifting fiber, that is looped at end inside the cell.

Each cell contains a fine (0.7 mm radius) double-clad Kuraray WLS fiber that is looped at the bottom down the entire length of a cell in U shape and is shown in green color in Figure 3.6. The fiber captures the light in violet-blue range and emits

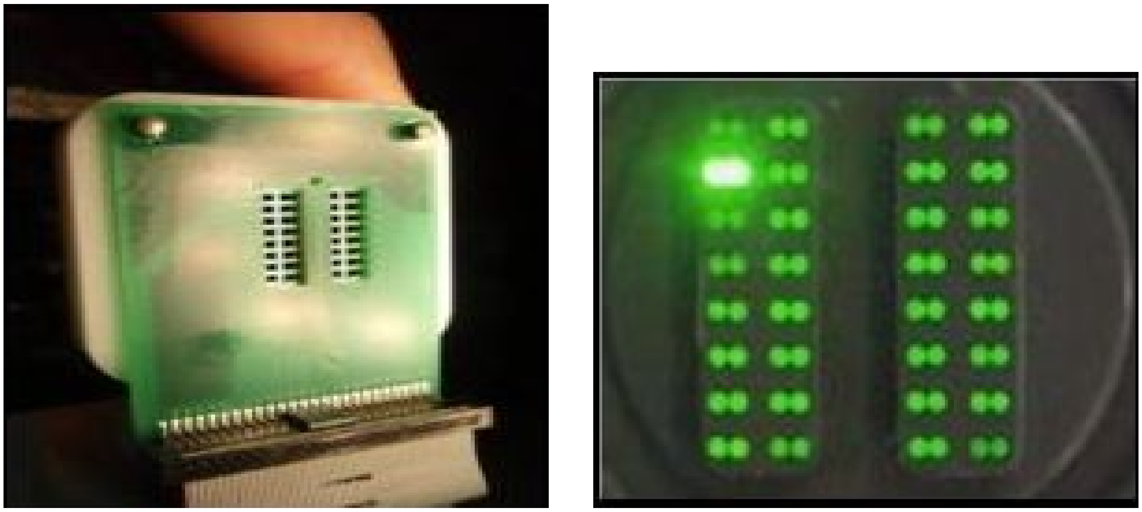

Figure 3.7: (Left) A picture of 32-pixel avalanche photo-diode used to collect scintillation light via wavelength shifting fibers. (Right) A picture showing that both ends of fiber are read-out by a single APD pixel.

in the blue-green range (450-600 nm). Both the fiber ends in a single cell are read out by a single pixel of 32-pixel APD to improve the collection efficiency [54].

The NOvA's photo-detector, APD, for the read-out purposes is manufactured by Hamamatsu and was chosen because of its high quantum efficiency, 85%, in the green region [54]. The high quantum efficiency is required to observe a weak light signal from the longer cells, 15.5 m long, especially in the NOvA FD. The APD's are operated for a gain of 100 using an applied voltage of 375V. The thermal noise is reduced by keeping the APD's at -15^{o}C. The surface of APD's is coated with a thin and transparent layer of paralene to isolate it from humidity and there is a continuous supply of dry nitrogen gas through the APD housings to keep ice from forming on the surface. Each NOvA APD is a 32-pixel APD where each pixel reads out a single cell. The amount of light collected by the APD is determined by the combined effects of the scintillator, PVC cell extrusions and the wavelength-shifting fibers.

The signal from the APD is further amplified using sensitive, low noise electronics designed for NOvA. The amplified signal from the APD is read-out by the front end board (FEB) which converts it into digital hits above a certain threshold. There is one FEB per APD. The hit information from the 64 FEB's is collected by a single data concentrator module (DCM). The DCM collects hits in the form of microslice (the data is condensed into 50 microsecond blocks). The DCM sends all the collected hit information in the form of millislice (hits collected in a 5 millisecond time window) to a single buffer node. The data stays in the buffer farm for 20 minutes before being erased from memory before any trigger decision is made. The system has 3 seconds to decide whether to keep the hits on the basis of a trigger algorithm to save the required information for permanent processing [57].

The NOvA detectors are low Z (85% Carbon and 14% Hydrogen), highly active tracking calorimeters which are able to differentiate between muons (long tracks), electrons (electromagnetic (EM) showers) and pions (leave a gap before decaying to gammas) and is illustrated in Figure 3.8. The NOvA's design allows for very good EM shower reconstruction to tag ν_e, the primary goal of NOvA (ν_e appearance). The typical electron showers traverse 10-80 planes whereas, the photons traverse app. 6 planes before converting which is important for the background rejection.

3.2.1 The NOvA far detector

The NOvA FD (See Figure 3.9) is located in Ash River, northern Minnesota 810 km away from the NuMI target at Fermilab. The detector is placed 14 milliradians off the NuMI beam axis. As the NOvA FD is located on the surface, so it uses a concrete shielding (concrete and loose barite (barium loaded) rocks) to reduce the effect of the cosmic rays. The barite is a high-Z material that is effective in shielding photons. The NOvA FD volume is $15.6 \times 15.6 \times 60\ m^3$ with an alternating planes of horizontal and vertical modules. The total detector mass is 14 kilotons (62% liquid scintillator). It contains 12 modules per plane, where 32 planes form one block. There are a total of 28 blocks in the FD. The electronics were instrumented in the diblocks (consisting of 64 planes). Each diblock has 12 DCMs and each DCM has 64 FEB's.

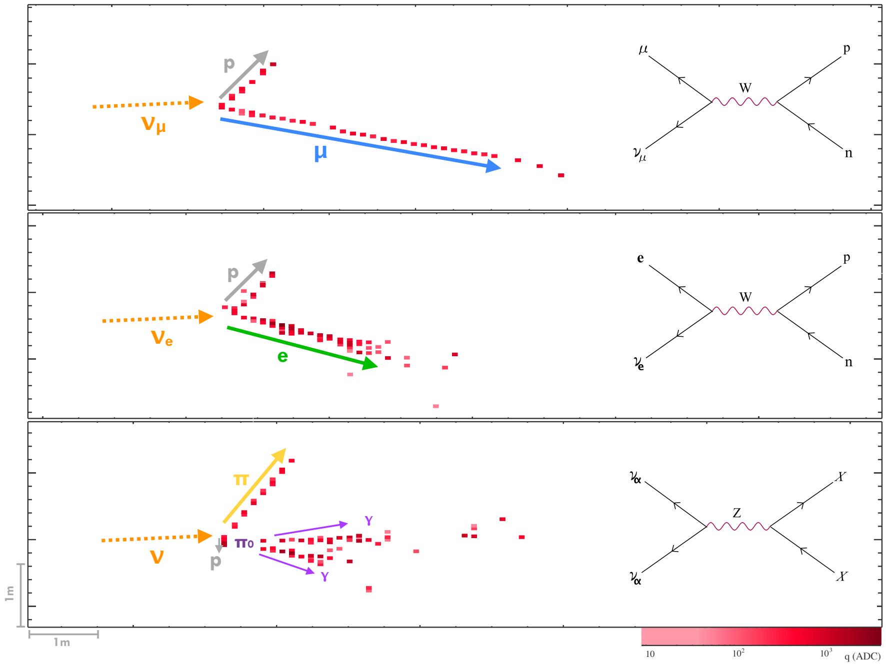

Figure 3.8: Figure showing the neutrino interactions in the NOvA detectors. Top panel shows a ν_μ CC interaction which is identified by a long muon track (shown by blue arrow). Middle panel shows a ν_e CC interaction which is identified by an electron shower. Below panel shows an NC interaction, where a π^o decays to two photons that shower electromagnetically.

3.2.2 The NOvA near detector

The NOvA ND (See Figure 3.10) is located at Fermilab 1 km away from the NuMI target. The detector is placed 14 milliradians off the beam axis and is located 100 meters underground. The detector is functionally identical to the FD and consists of the same modules but differ in length. The NOvA ND has two parts, 12.8 m long active region and 3.1 m long muon catcher located at the downstream end. The detector volume is $3.9 \times 3.9 \times 12.6\ m^3$ with a total detector mass of 193 tons (45% is liquid scintillator and 27% is steel in the muon catcher). The active region consists of 192 planes with 3 modules. The electronics were instrumented in 3 diblocks. Each diblock has two DCMs for the vertical plane and two for the horizontal plane but with different number of FEB's. One DCM in each view is fully occupied with 64 FEBs and the another is with 32 FEBs. The muon catcher region has 22 planes and

Figure 3.9: An image of the NOvA FD. It is worth pointing to the person standing on the catwalk on the right side of the figure which gives reader sense for the scale of the detector.

is made up of steel plates. The main purpose of the muon catcher is to stop muons and improve containment.

As the NOvA ND is located close to the target source, it has high statistics and thus provides an excellent opportunity for the measurement of various neutrino interactions mainly cross-section measurements.

3.3 Calibration

Calibration is done to convert the recorded signals, recorded by APD, into physically meaningful units for instance MeV or GeV. To calibrate the NOvA detectors, cosmic ray muons are used because they provide a source of uniform energy across the detectors [58]. Also, the energy deposition by the stopping muons can be precisely measured using Bethe-Bloch formula. Calibration in the NOvA detectors is done in

Figure 3.10: An image of the NOvA ND where the detector's top view is visible.

two steps, Relative calibration and Absolute calibration.

Relative calibration corrects for attenuation, attenuation of light while traversing the WLS fibers. The main purpose of relative calibration is to express the amount of energy deposited in the detectors and registered by APD in comparable units. However, Absolute calibration expresses the energy deposits in physically meaningful units of energy (GeV). For both types of calibration, NOvA uses cosmic ray muons that are collected recording the signals from periodic time windows asynchronous to the beam spill. Beam spill is defined as the 10 microsecond time window within which neutrino interactions from the beam occur. The muons that stop inside the detector provide a most reliable energy deposition for better energy calibration and these stopping muons are identified by their decay to Michel electrons ($\mu \rightarrow e^- + \bar{\nu}_e + \nu_\mu$). The details of the two phases of calibration are discussed in [58].

3.4 Simulation

The NOvA simulation occurs in various stages. It starts with the NuMI beam-line simulation followed by the neutrino interaction simulation and detector simulation. Below, we describe briefly these steps one by one.

1. **Beam simulation:** NOvA uses GEANT4 package [59] to simulate the NuMI beam-line geometry. The simulation begins with the interaction of 120 GeV protons with the graphite target and a subsequent interaction of the secondary particles (mainly hadrons), focusing of the particles and their decay to neutrinos.
   To correct for the hadron production mis-modeling in the NuMI beam-line simulation, NOvA uses an external package called Package to Predict the FluX (PPFX) [60]. PPFX determines the neutrino flux using all relevant data for the NuMI beam from hadron production experiments. A weight is applied to each event in Monte-Carlo to correct for the flux.
   The output of beam simulation is stored in the flux files that contain all the relevant information of the neutrinos (ν flavor, energy, momentum) and their parents. These files are created for both the FHC and RHC beam configurations.

2. **Neutrino interaction simulation:** NOvA uses an improved GENIE model [61] to simulate the neutrino (anti-neutrino) interactions. In the NOvA FD events, there is a major contribution of cosmic ray background which is simulated using CRY package [62]. The flux files produced after the beam simulation are input to the GENIE and CRY packages where a list of particles that are produced in the neutrino interactions is created.

3. **Detector simulation:** The NOvA detector simulation is handled by GEANT4 where the particle list produced after the neutrino interactions is

passed through the detector to produce energy deposits [63]. A list of energy deposits is then passed through the front end simulation where the energy deposited is converted into the scintillation light that gets captured by the WLS fibers to APD to produce digitized waveforms.

The end product of the simulation chain is a ROOT [64] output file, the format of which matches with the data file with an additional truth information.

3.5 Reconstruction

The NOvA collects raw data (or cell hits) in 550 microsecond time window for the entire detector. From all the collected events, the events that occur in the beam spill are considered as the signal events. The remaining events, that occur outside the beam spill, are considered as noise which are used for background determination. As the NOvA FD is located on the surface there is a significant background from the cosmic rays. For the oscillation analysis an accurate reconstruction of neutrino interactions is desired for the precise measurement of neutrino energy, flavor and type of interaction. On the other hand, for the NOvA ND there are multiple neutrino interactions in each event, due to its close proximity to the target, that needs to be identified. An accurate identification of particle content of each interaction is required for making a cross-section measurement with the NOvA ND. Reconstruction of events (simulated and data) in the NOvA detectors is done in various steps and are briefly described here:

1. The first step in the reconstruction chain is "Slicing" which makes use of "Slicer4D" algorithm [65] to sort the calibrated data into space-time slices. The cell hits that are causally linked (space-time correlated) are clustered together to form "Slices". The main purpose of this module is to separate the

signal hits from the noise and a subsequent separation of signal hits into a cluster of hits that originated from different sources. Slicing is done in the two detector views, XY and YZ view.

2. After clustering the hits in each view of the detector, the next step is to find a global vertex which is called as Vertexing. It is done by first identifying the lines which are clearly visible in the data using a modified Hough Transform [66], [67]. This algorithm fits the cells in a slice to the Hough lines which represent the major/global features in our events. Then, the hough transform algorithm results are used by another module called "ElasticArms" algorithm to find the neutrino primary interaction vertex [68].
3. The vertex information from the ElasticArms is used by another package named as "Fuzzy-KVertex" which clusters the hits into prongs. A prong in the NOvA terminology is defined as a collection of cell hits with a starting point and direction. The end goal of this reconstruction chain is to produce an interaction vertex and a list of prongs associated with that vertex [69].

4. Then, the tracks from individual slices are reconstructed using "Kalman algorithm" [70]. The goal of tracking is to trace the trajectory of individual particles that deposit energy in the detector. The Kalman algorithm takes the cluster of hits formed from the slicer algorithm as an input and construct tracks in both the detector views (XZ and YZ) separately. This is widely used to identify muons that leave long tracks in the detector.

The combination of these reconstruction methods used by the NOvA have proven to be an effective means of identifying particles of interest and reconstructing their kinematics. The efficiency of this process is further enhanced through the use of more advanced techniques such as machine learning and computer vision.

NOvA has developed a robust event identification technique using deep learning methods particularly "Convolutional Visual Network (CVN)" [71]. CVN was developed to identify neutrino interactions based on their topology. CVN was trained on approximately 4.7 million simulated neutrino interactions. Four separate CVN classifiers are developed based on the interaction types, ν_μ CC, ν_e CC, ν_τ CC and ν NC. These classifiers give a score 0 to 1 to an event, where 0 is most likely background events and 1 is for signal events and more details are in chapter 5.

Also, CVN was trained to identify the particle types where the network was trained on the five different particles (electron, gamma, muon, pion and proton).

Having the deep learning techniques to identify the events in the NOvA detectors increased the efficiency by 30% which has resulted in an effective 30% increase to our neutrino event yield [71].

3.6 Summary

The experimental details of the NOvA experiment are discussed. The NOvA experiment with a baseline of 810 km study neutrino oscillations in appearance and disappearance channels. There are various puzzles for instance the neutrino mass hierarchy, value of θ_{23} if it is maximal or not, CP-violation in lepton sector and existence of sterile neutrinos, which NOvA hopes to resolve. The experiment has collected data both in neutrino and anti-neutrino mode and is currently taking data again in neutrino mode.

As a part of this thesis, simulations are performed to optimize the neutrino and anti-neutrino event yield for the NOvA detectors and are described in details in the next chapter.

Chapter 4

Off-axis Beam Studies for NOvA

In this chapter, simulation studies are performed to optimize neutrino and anti-neutrino event yield for the NOvA detectors. As shown in Figure 4.1, the NOvA FD observed a very few events with an exposure of 6.05×10^{20} protons on target [72]. So, more neutrino and anti-neutrino event yield is required to have more events in the FD. This has been the main motivation for the work done in this chapter.

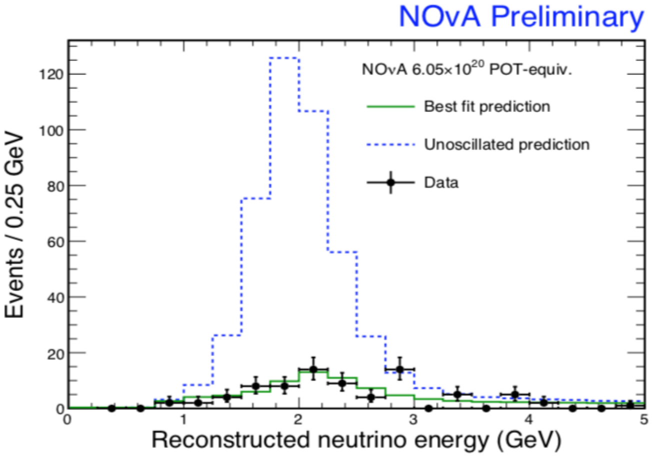

Figure 4.1: Figure shows the un-oscillated events and the events at the NOvA FD.

4.1 Introduction

The simplest view of the event yield for neutrino experiments is given by the following equation:

$$N \propto (POT)(M), \tag{4.1}$$

where POT is the number of protons on target and M is the mass of the neutrino detector. For the NOvA, this equation is modified to emphasize additional information as shown in the following equation:

$$N \propto (\text{beam power})(t)(\nu \text{ per proton}) \times (M)(\epsilon) \tag{4.2}$$

The number of protons on target is beam power multiplied by the running time (t) of the experiment and illustrates the importance of increasing the beam power to 700 kW. The detector mass is also modified in equation 4.2 by the detector efficiency (ϵ) for finding the events of interest. For a Segmented Scintillator detector like NOvA, ϵ for the ν_μ CC and ν_e CC events is 25-40% and 55-60% respectively [73], [74] and [75]. The term ν per proton is the efficiency of the NuMI target and horn system to produce useful neutrinos in the NOvA detector. If one could realize 10% more ν per proton on target, the event yield of the experiment would be 10% higher just as if the experiment had a detector of 10% larger mass or a proton beam of 770 kW. So, this is a crucial factor.

In this chapter, we look systematically at ways which might increase the ν per proton yield of the NuMI target and horn system in the energy range of interest to the NOvA experiment i.e. 1-3 GeV. The wrong sign contamination and ν_e contamination in the beam is also studied.

An immense amount of simulation work to optimize the neutrino and anti-neutrino event yield by re-configuring the NOvA target and horn system is performed as a part of this thesis. So, before discussing the simulation results it is important to first describe the NuMI beam-line components and software framework used for the simulations.

4.2 The NuMI beam-line components

A sketch of the NuMI beam-line is shown below in Figure 4.2. In the previous chapter, the production of neutrino beam from the NuMI beam-line was discussed briefly. In this section, the details of all the beam-line components are described.

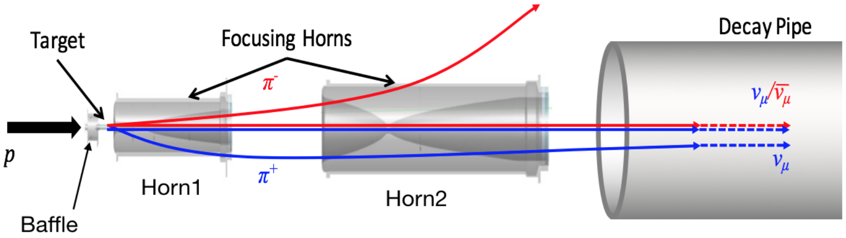

Figure 4.2: A sketch showing the NuMI beam-line components which shows the production of the ν_μ beam in the FHC beam configuration where the positively charged pions are focused by the horns to produce neutrino enhanced beam.

4.2.1 Baffle

The baffle is a specially designed device which is installed upstream of the target as shown in Figure 4.2 . It is made up of graphite and encased in an aluminum (Al) tube. The baffle is designed so as to withstand the full intensity of the beam (with 700 kW beam power) and if mis-steering (in the form of excessive heat) is detected then it degrades mis-steered beam enough that the target and horns are not damaged.

4.2.2 The NOvA target

The target used for the NOvA experiment is made up of graphite material and encased in a target casing made up of Al, a sketch of the same is shown in Figure 4.3.

The graphite is ZXF-5Q from Poco graphite and has a density of 1.78 gm/cc [76]. The NOvA target consists of 48 graphite segments (fins) and 2 Budal monitors. Each graphite fin is 24 mm long along the beam direction, 7.4 mm wide and 63 mm high. The total height of one graphite segment is 150 mm and the free distance, where the beam interacts, is 63 mm and the remaining part is buried in between the supporting structure, that supports the target. All the fins are placed with equal gaps of 0.5 mm. The gaps help to reduce the mechanical stress in the target material [54]. The interaction of proton beam with the target generates heat which needs to be removed so as to avoid any damage to the target. For this purpose, the cooling water runs along the target through a helical groove machined at the outer surface of target casing, which is made up of a heavy-wall pipe.

For the beam monitoring purposes, the upstream end of the target has two additional graphite fins which are called Budal monitors. They are electrically isolated from the rest of the target and are used to scan the beam position [76]. Thus, the total target seen by the beam is 50 fins or ∼122 cm of graphite material.

Proton interaction with the target results in the production of many short-lived secondary particles such as pions, kaons that are focused by a focusing system consisting of two horns and is described in the following subsection.

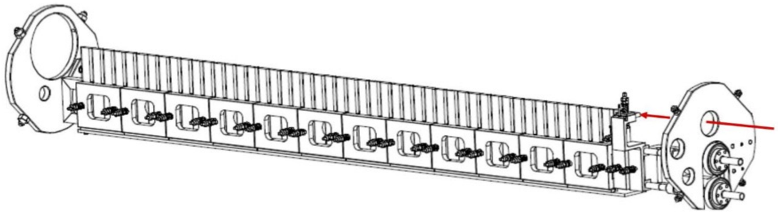

Figure 4.3: Sketch of the NOvA target consisting of 48 graphite segments and two Budal monitors (right end). The primary proton beam runs through the target from right to left (red arrow).

4.2.3 The Focusing system - Magnetic horns

The secondary mesons produced in the target are focused by a set of two parabolic magnetic horns, Horn1 and Horn2, located downstream of the target as shown in Figure 4.2. The horns are made up of Al [76]. The idea of using two horns is to improve the neutrino flux by better focusing the secondary particles in the beam direction. Some of the low (high) energy mesons get over-focused (under-focused) by the Horn1 are then focused by the Horn2 thus increasing the efficiency of the focusing system by about 50%.

The NuMI horns were designed to sustain currents of up to 200 kA producing a field of up to 3 T inside the horn field region. As discussed briefly in the previous chapter, the horns select the charge sign of the secondary particles produced in the target. Positive horn current (+200 kA) focuses the positively charged particles such as π^+, K^+ as shown in Figure 4.2 that decay in flight to give an almost pure beam of neutrinos (ν_μ). This beam configuration is referred to as the FHC beam configuration. On the other hand, negative horn current (-200 kA) focuses the negatively charged particles such as π^-, K^- to give an anti-neutrino enhanced beam and is referred to as the RHC beam configuration. So, the horn polarity is the deciding factor for the production of either neutrino rich or anti-neutrino rich beam. There is a deposition of heat due to the beam and pulsed current which is removed using nozzles that spray water continuously on the inner conductor of the horns.

The upstream end of the Horn1 is placed at origin (MCZERO) [76] and is considered as a reference to define the position of other beam components. For instance, the downstream end of the NOvA target is placed at -20 cm w.r.t the Horn1. Similarly, the position of the Horn2 is also defined w.r.t the Horn1. For the NOvA run, Horn2 is placed at 19.18 m w.r.t the Horn1. The relative separations of the two horns determine the energy profile of the neutrino (anti-neutrino) beam that is produced. In the current beam design, the Horn2 can be placed at either of the three different positions - 10 m, 23 m and 37 m w.r.t the Horn1, corresponding to the low energy

(LE), medium energy (ME) and high energy (HE) Horn2 configuration [55]. The LE and ME Horn2 positions are shown in Figure 4.4. The NuMI horns for the NOvA experiment are in the ME configuration.

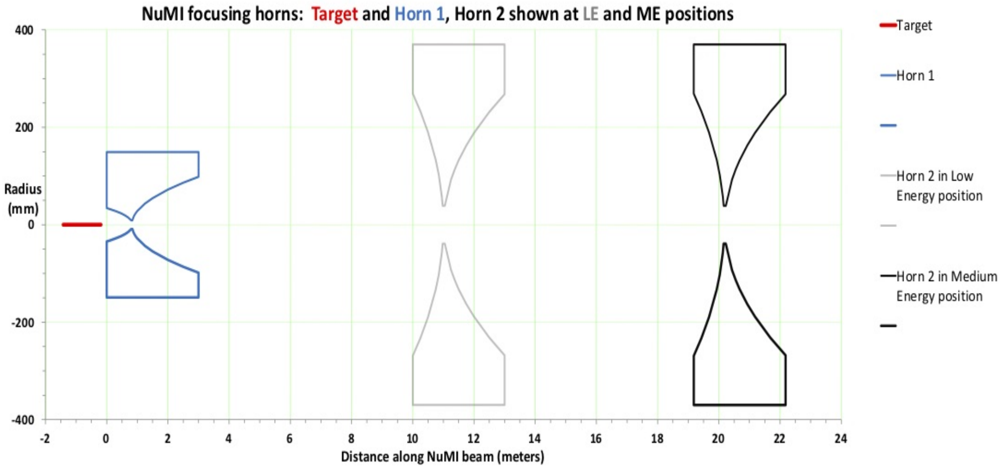

Figure 4.4: The NuMI target fins (red) as seen from above with the two focusing horns. Horn1 (blue) starts at MCZERO. Horn2 is shown in ME (black) and LE (gray) positions. Note that the vertical axis is in millimeters, while the horizontal axis is in meters.

4.2.4 Decay Pipe, Hadron Absorber and Muon Shield

The particles that are focused by the horns then enter into the 675 m long decay pipe (steel pipe) as shown in Figure 3.2. The decay pipe is filled with Helium at 0.9 atm pressure. The particles propagate in this low density environment and decay to give tertiary mesons, charged leptons and neutrinos or anti-neutrinos, depending on the horn polarity.

The beam then passes through the NuMI absorber as shown in Figure 3.2 which is a massive aluminum, steel and concrete structure that stops the hadron component of the beam allowing the neutrinos and some of the mesons to pass through it. The absorber core is surrounded by the Duratek steel blocks and a layer of concrete shielding that absorbs low energy neutrons.

The remaining muons in the NuMI beam, with momentum above 3-4 GeV, after the absorber are ranged out in the so-called muon shield, which simply consists of 240 m of solid dolomite rock.

4.3 Software Framework

4.3.1 FLUGG

FLUGG is a Monte Carlo (MC) simulation package [77] that integrates GEANT4 [79] geometry description into FLUKA code [78]. GEANT4 geometry includes details of beam-line components like target, horns, decay pipe, hadron absorber and muon monitors. FLUKA code can efficiently access GEANT4 geometry and simulate the interactions and decays of particles as they propagate and interact with material and each other.

The simulation begins with defining primary proton. When the primary proton enters the target region, its initial properties are recorded and are used for all the particles which come from this proton. While in the target, the proton presumably interacts, producing potentially many secondary particles. As these secondaries leave the target volume, their properties are stored. All the later generations of particles following from a particular target parent keep reference to the target parent's entry. This way, when we get a neutrino we have the information about the particle that produced it as it left the target.

For the beam simulation studies discussed in the upcoming sections, the versions used are as follows:

- FLUGG 2009_3
- FLUKA.2011.2c.0

For Momentum from threshold to 5 GeV/c: The FLUKA hadron nucleus inelastic

interactions are described in terms of resonance production and decay up to a few GeV. For this the PEANUT model is used [77]. At higher energies, a model based on Dual Parton Model (DPM) [78] takes over. DPM is a particular quark/parton string model and provides reliable results up to several tons of TeV.
For this study, beam spot size is kept at 1.1 mm, horn current is set to 200 kA and 5M POT are used.

4.3.2 G4NuMI

G4NuMI [80] is a pure GEANT4 based simulation of the beam-line. G4NuMI and FLUGG simulation packages share the same GEANT4 geometry of the NuMI beam-line components. A simple model of incoming proton beam is used as a source of initial particles. The primary output represents the decays of secondaries that give rise to neutrinos. The GEANT4 version along with the physics list are:

- GEANT4 version : v4_9_6_p03b
- Physics List : FTFP_BERT. The FTFP model implements high energy inelastic scattering of hadrons by nuclei using the FRITIOF model of B. Andersson et al. It forms QCD strings by pairing a parton from the projectile hadron with a parton from a target nucleon. The strings are then excited by momentum exchange which can result in diffraction of the target or projectile or both. The FTFP model may be applied to incident nucleons, pions, kaons and hyperons from 3 GeV to several TeV. The Bertini-style (*_BERT*) cascade implements the inelastic scattering of hadrons by nuclei. Nucleons, pions, kaons and hyperons may be used as projectiles in this model.
  This list uses BERT style cascade for hadrons < 5 GeV and FTF (FRITIOF) model for high energies (>∼ 10 GeV).
- Beam spot size, number of POT and horn current is kept same as in FLUGG.

4.4 Errors on the Neutrino Event Yields

The objective of this study is to find the errors associated with the event yields that are obtained with G4NuMI. There are two effects that can result in the errors - the number of POT in the simulation, and the effect of the importance weights assigned by the simulation package. The statistical errors scale like the square root of the number of POT. An additional error due to the importance weights is not known. So, to add the statistical error bars to the event yields the study is performed by generating 1000 samples where each sample corresponds to 500k POT. The samples are divided into different sub samples (files) to check the statistical mean and RMS value and are obtained for the NOvA ND and FD which is shown in Table 4.1. In the first column, each file corresponds to the 500k POT. That means 10 files and 100 files have 5M and 50M POT respectively.The results have stable means and the RMS of the distributions get smaller as the number of samples is increased which is expected.

Figures 4.5 and 4.6 show the distribution of ν_μ and ν_e mean and RMS, for the various samples, obtained for the NOvA ND and FD. FD numbers are scaled by a factor of 10^6.

To understand the RMS behavior of the events obtained for the NOvA ND and

Table 4.1: Mean and RMS of the G4NuMI event yields obtained for the NOvA ND and FD in sets containing different numbers of POT.

	ND Mean		ND RMS		FD Mean		FD RMS	
Number of files	ν_μ	ν_e	ν_μ	ν_e	ν_μ	ν_e	ν_μ	ν_e
5	76.99	0.52	0.24	0.027	88.65	0.62	0.22	0.028
10	76.96	0.51	0.20	0.017	88.67	0.61	0.21	0.018
25	76.96	0.52	0.12	0.009	88.66	0.61	0.13	0.009
50	76.96	0.52	0.09	0.007	88.67	0.61	0.10	0.007
75	76.95	0.52	0.07	0.005	88.69	0.61	0.09	0.005
100	76.96	0.51	0.06	0.004	88.68	0.61	0.07	0.004
150	76.93	0.52	0.02	0.003	88.66	0.61	0.02	0.003
200	77.01	0.52	0.01	0.002	88.62	0.61	0.004	0.002
1000	76.96	0.52			88.66	0.61		

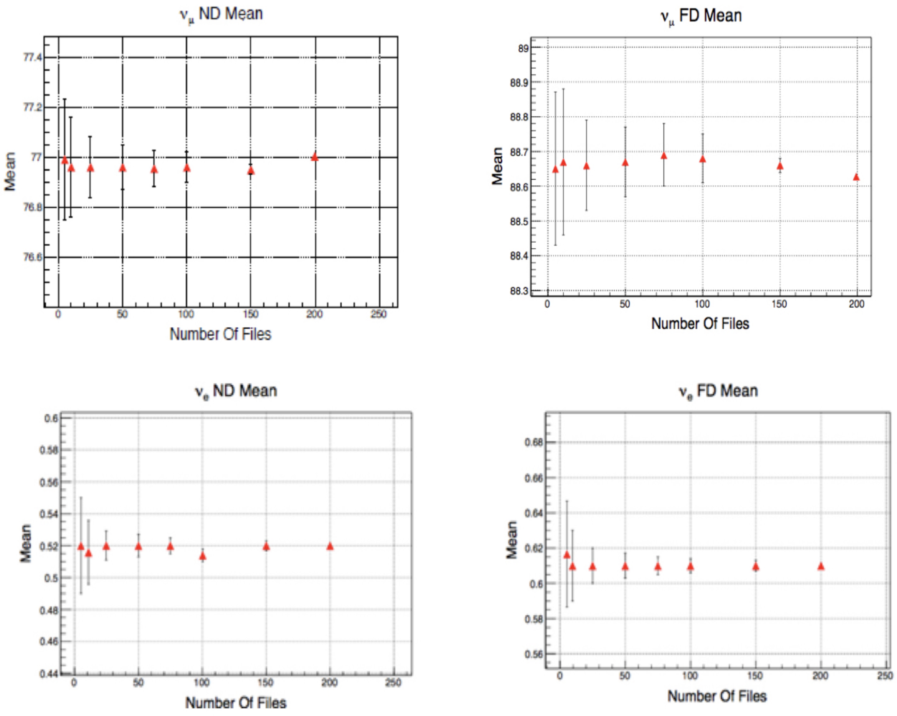

Figure 4.5: Mean of ν_μ events (upper row) and ν_e events (lower row) vs number of files for the NOvA ND and FD with G4NuMI.

FD, data points have been compared using fitting function $a/\sqrt{x}$ and is shown in Figure 4.7 (left). The RMS value of the points with higher statistics (150 and 200 files) is smaller than expected, indicating that some process beyond simple statistics is at work for low numbers of files (low POT).

The G4NuMI RMS points are next fit to $1/\sqrt{N}$ only at the 150 and 200 file points, then the residual of this fit to the data is extracted and is shown in Figure 4.7 (right). As with FLUGG [81], one observes larger errors at low number of files than a simple fit based on statistics. There appears to be an excess error mechanism for files below 100 (= 50M POT). The RMS values as shown in Table 4.1 are used to assign an uncertainty to the event yield at NOvA ND and FD. The typical number of files used throughout this chapter are 10 files per point with each file is having 500k POT. For 10 files per point or 5M POT, the estimated uncertainties on the mean values are very small as shown below in Table 4.2. These % errors for 10 files

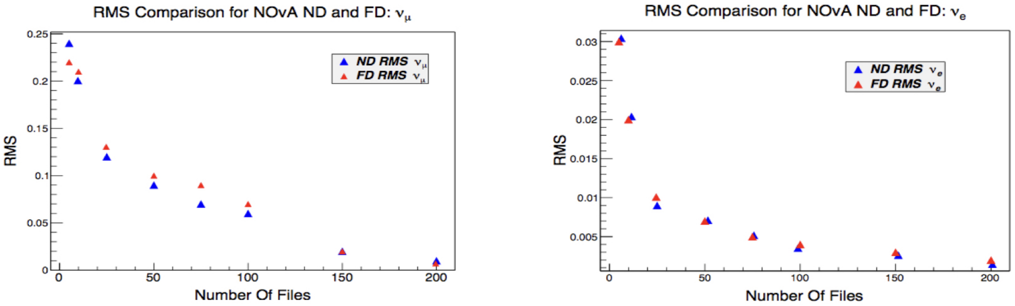

Figure 4.6: G4NuMI RMS of ν_μ events (left) and ν_e events (right) vs number of files for the NOvA ND and FD.

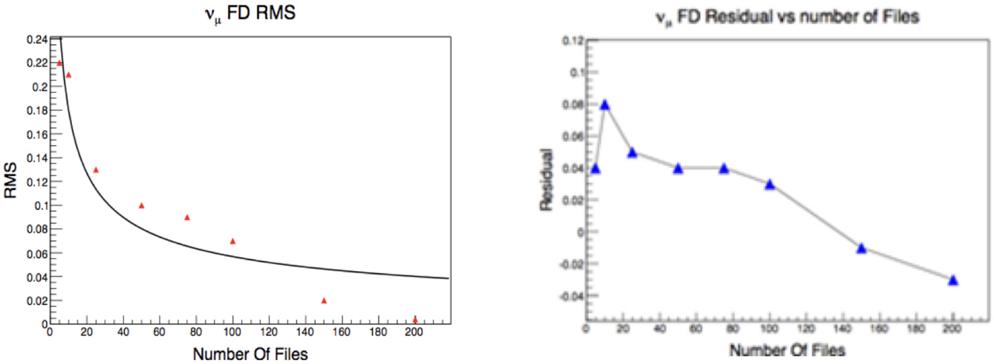

Figure 4.7: (Left) Example fit of G4NuMI RMS values of the NOvA FD events. (Right) Example plot of the difference between the data points (G4NuMI points) and a $1/\sqrt{N}$ fit constrained at 150 and 200 files.

are very similar to the values found with FLUGG [81].

Though the G4NuMI and FLUGG results are very similar, there are some differences in the number of events. One such example is shown below in Table 4.3 where we compare the G4NuMI and FLUGG ν_μ results on simulating 5M POT. The difference is 3.9% for both the ND and the FD for ν_μ events in the FHC mode. Similar trend is seen for the RHC beam configuration [81].

These two simulation packages use the same GEANT4 geometry so the differences might come from the difference in event generation of particles in p-Carbon collisions at 120 GeV. These differences can be used as a measure of the systematic errors. These two simulators share same geometry which could still have additional systematic error. These are large systematics far outweighing the statistical errors

Table 4.2: Typical errors on event yields in G4NuMI with 10 files (5M POT).

Detector	ν flavor	Event yield	G4NuMI % error (5M POT)
ND	ν_μ	76.96	0.25%
ND	ν_e	0.51	3.9%
FD	ν_μ	88.67×10^{-6}	0.24%
FD	ν_e	0.61×10^{-6}	3.3%

discussed above in this section and neither simulation program has any claim to being more correct than the other.

Table 4.3: Comparison of FLUGG and G4NuMI ν_μ results in FHC mode. The FD results have been multiplied by a factor of 10^6.

Source	ν_μ events in ND (1-3 GeV)	ν_μ events in FD (1-3 GeV)
G4NuMI	76.96	88.67
FLUGG	79.98	92.12
FLUGG/G4NuMI	1.039	1.039

4.5 Target and Horn Optimization Study

This section discusses the target and horn optimization studies which might increase neutrino per proton yield for the NOvA detectors. As discussed in [73], longer NOvA targets show no gain in neutrino event yield. In this section, the impact of shorter targets, with Horn2 in ME and LE positions, on neutrino event yield for the NOvA ND and FD is discussed. The neutrino event yield reported in the following subsection is in the energy range of 1-3 GeV and is normalized to 6×10^{20} POT. Neutrino event yield at the NOvA FD is additionally multiplied by a factor of 10^6.

4.5.1 Shorter Targets with Horn2 in ME position, G4NuMI

The standard NOvA target consists of 48 graphite fins with two Budal monitors. We compare the number of events obtained in the FHC and RHC beam configurations for targets with different number of fins using G4NuMI. We investigate if there is a maximum in the distribution of the number of events with respect to the number of fins in the target. The horns are in ME position and the target position is unchanged. Starting from a target with 48 fins, the fins are removed in steps of 4 fins at a time starting from the upstream end, as shown in Figure 4.8. The position of the two Budal monitors follow the fin position and they are placed in front of the most upstream fin in every configuration. For this study, 5M POT are simulated. Figure 4.9 shows the variation of the neutrino event yield with various target configurations in the FHC mode for the NOvA ND and FD (off-axis case). The peak in ν_μ yield is found with 40 fins target configuration. Figure 4.10 shows the variation in event yield in RHC mode and the peak is also with 40 fins target. Table 4.4 shows the number of events in FHC and RHC beam configuration only for 48 fins and 40 fins target. The number of events for all the other target configurations are available in [83].

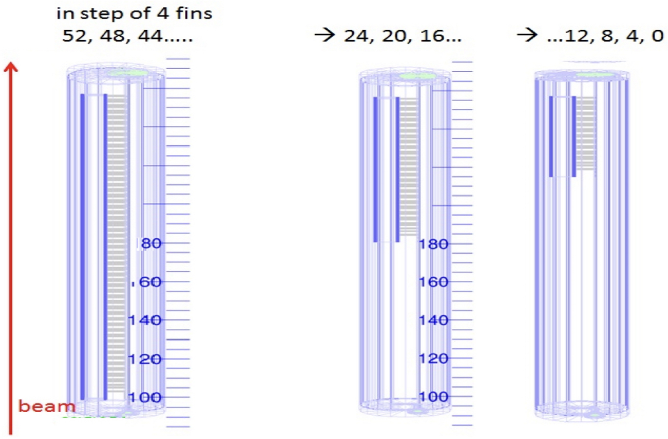

Figure 4.8: Geometry showing the different target configurations by removing the graphite fins from upstream end of the target.

Figure 4.11 shows the neutrino (left) and anti-neutrino (right) energy spectra comparison for 48 and 40 fins target configuration for the NOvA FD with Horn2 in ME position. A slight increase in the neutrino yield is seen around the peak

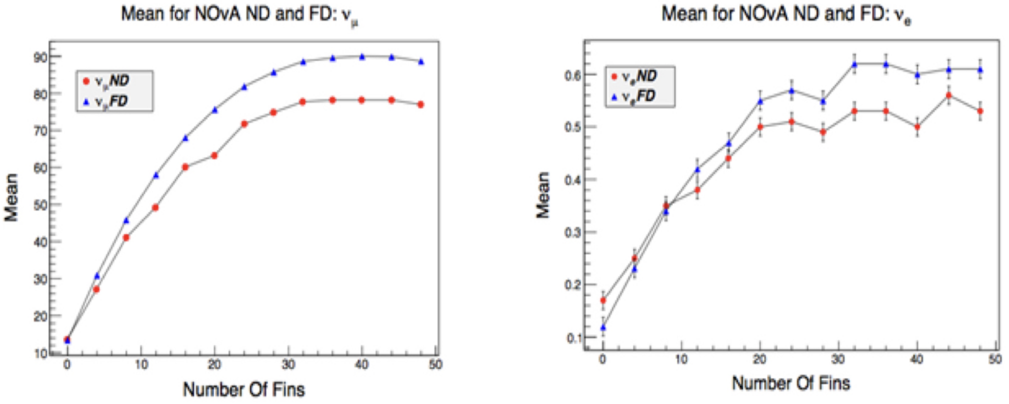

Figure 4.9: G4NuMI ν_μ (left) and ν_e (right) event yield variation on changing the target fin configuration for the NOvA ND (red) and FD (blue) in the FHC beam configuration with Horn2 in ME position.

Table 4.4: 48 and 40 fin G4NuMI event yields in the range 1-3 GeV for NOvA ND and FD, for FHC and RHC beam configurations, with Horn2 in ME position.

	NOvA FHC		NOvA FHC		NOvA RHC		NOvA RHC	
	ν_μ		$\bar{\nu}_\mu$ & ν_e+$\bar{\nu}_e$		$\bar{\nu}_\mu$		ν_μ & ν_e+$\bar{\nu}_e$	
No. of fins	ND	FD	ND	FD	ND	FD	ND	FD
48	76.88	88.71	1.5 & 0.53	1.6 & 0.61	30.84	35.57	3.38 & 0.19	3.74 & 0.23
40	78.16	90.03	1.6 & 0.50	1.7 & 0.61	31.48	36.25	3.71 & 0.19	3.97 & 0.23
% change (40/48 fins)	1.7	1.5	6.6 & -6	6.2 & 0	2.1	1.9	11 & 0	6 & 0

region with 40 fins target configuration. It is important to note that the peak is still at 2 GeV, where the probability of oscillation is maximum for the NOvA off-axis experiment. The ν_μ event yields increases by 1.5% for the FD in FHC and by 1.9% in RHC when the target is shortened from 48 to 40 fins. At the same time FD beam contaminations for 40 fins is unchanged for FHC, while for RHC the $\bar{\nu}_e$ beam contamination is unchanged and the ν_μ beam contamination increases by 6% (but only by 0.6% relative to the $\bar{\nu}_\mu$ primary beam component).

The similar study performed with FLUGG [81] program shows a peak in neutrino event yield with 36 fins target configuration.

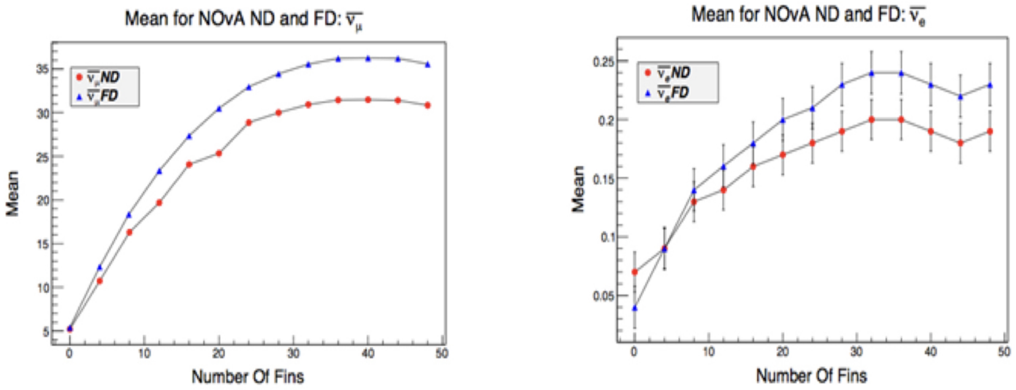

Figure 4.10: G4NuMI $\bar{\nu}_\mu$ (left) and $\bar{\nu}_e$ (right) event yield variation on changing the target fin configuration for the NOvA ND (red) and FD (blue) in the RHC beam configuration with Horn2 in ME position.

4.5.2 Shorter Targets with Horn2 in LE position, G4NuMI

In this section, neutrino event yield with various target configurations as done in the previous subsection is studied by placing Horn2 in LE position. The target position is unchanged.

The number of CC+NC events, in 1-3 GeV energy range, obtained in FHC and RHC beam configurations for targets with different configurations using G4NuMI are reported in Table 4.5. Here also we investigate for the maximum in the neutrino event yield with respect to the number of fins in the target. Again, 5M POT are simulated for both the FHC and RHC beam configuration.

Figure 4.12 shows the variation of the neutrino event yield as the number of target fins is increased from 4 to 48 in the FHC (left) and in RHC (right) beam configuration for the NOvA ND and FD. In this case, 36 fins target configuration gives the maximum ν_μ event yield in the NOvA FD. This is slightly different from the peak yield found at 40 fins in the ME mode in previous subsection, but the peak is fairly flat. The number of events for all the other fins target configurations are listed in [83].

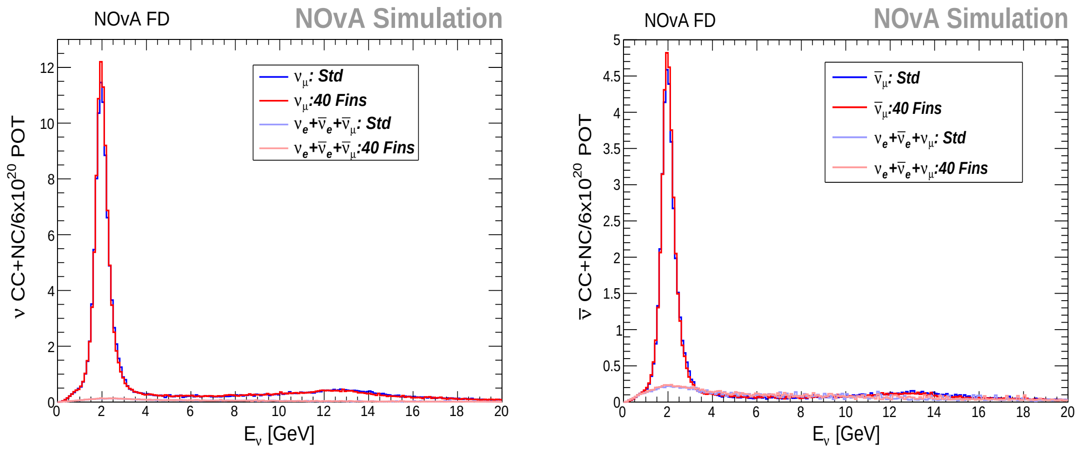

Figure 4.11: G4NuMI ν (left) and $\bar{\nu}$ (right) energy spectra for 48 and 40 fins target for the NOvA FD with Horn2 in ME position. The wrong sign contamination together with ν_e beam contamination (Light blue and pink) for both the target configurations are shown.

Table 4.5: 48 and 36 fin G4NuMI event yields in the range 1-3 GeV for NOvA ND and FD, for FHC and RHC with Horn2 in LE position.

	NOvA FHC		NOvA FHC		NOvA RHC		NOvA RHC	
	ν_μ		$\bar{\nu}_\mu$ & ν_e+$\bar{\nu}_e$		$\bar{\nu}_\mu$		ν_μ & ν_e+$\bar{\nu}_e$	
No. of fins	ND	FD	ND	FD	ND	FD	ND	FD
48	69.62	81.42	1.6 & 0.47	1.7 & 0.54	28.04	32.71	3.53 & 0.18	3.80 & 0.21
36	71.48	85.35	1.8 & 0.51	1.9 & 0.57	28.64	34.24	4.07 & 0.21	4.34 & 0.23
% change (40/48 fins)	2.7	4.8	12.5 & 11.7	6.2 & 6	2.1	4.7	15 & 17	14 & 10

Figure 4.13 shows the neutrino (left) and anti-neutrino (right) energy spectra comparison for 48 and 40 fins target configuration for the NOvA FD with Horn2 in LE position. As in ME case, a slight increase in event yield with 40 fins target configuration is seen around 2 GeV. The primary beam ν_μ event yields increase by 4.8% for the FD in FHC and by 4.7% in RHC when the target is shortened from 48 to 36 fins.

At the same time FD ν_e beam contamination for 36 fins remains goes up by 6% (only 0.04% of the ν_μ primary beam) for FHC. For RHC the $\bar{\nu}_e$ background increases by 10% and the ν_μ background increases by 14% (these are respectively only 0.05% and 1.6% of the $\bar{\nu}_\mu$ primary beam).

The increase here in event yield is comparatively more than that seen in the ME

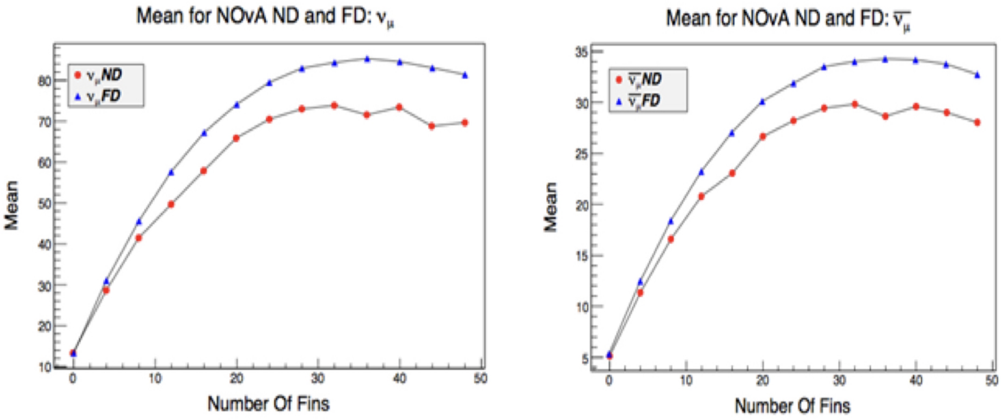

Figure 4.12: Number of events, for the FHC and RHC, in 1-3 GeV for different target configurations for the LE position of Horn2.

configuration in Table 4.4.

The similar study performed with FLUGG [81] shows a peak in neutrino flux with 36 fins target configuration.

4.6 Study of Parent Pion Kinematic Variables

From the studies in the previous section and [81], it is found that FLUGG predicts a 4-5% larger neutrino yield than G4NuMI in FHC mode, but G4NuMI predicts a 3.5% larger yield than FLUGG in RHC mode for different target and horn configurations. This section looks at various kinematic variables of NOvA neutrino parent pions and compares G4NuMI distributions with FLUGG distributions, in an effort to expose any basic differences between these simulation programs which might lead to the asymmetric FHC / RHC behavior.

4.6.1 Comparing G4NuMI and FLUGG

To understand the differences in the neutrino event yield predicted by G4NuMI and FLUGG, momentum distributions of the parent pions (pions that produce 1-3 GeV

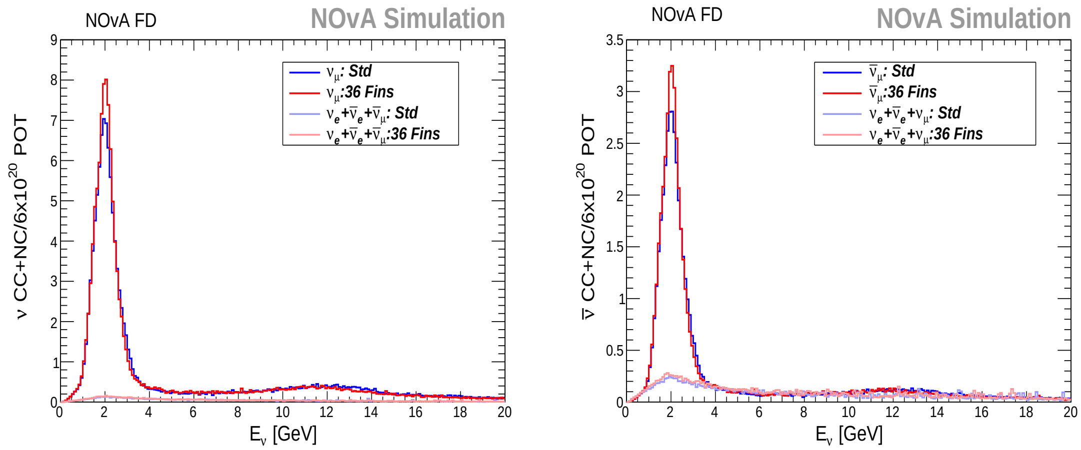

Figure 4.13: G4NuMI ν (left) and $\bar{\nu}$ (right) energy spectra for 48 and 40 fins target for the NOvA FD with Horn2 in LE position. The wrong sign contamination together with ν_e beam contamination (Light blue and pink) for both the target configurations are shown.

neutrinos) are studied. Figure 4.14 shows the longitudinal momentum (p_Z) and transverse momentum (p_T) distributions for positive pions that produce 1-3 GeV neutrinos seen by the NOvA. The p_Z and p_T region of interest for pions producing neutrinos is about 5 - 11 GeV and 200 - 400 MeV respectively.

Figure 4.15 (upper row) shows the p_Z distributions for all the positive and negative

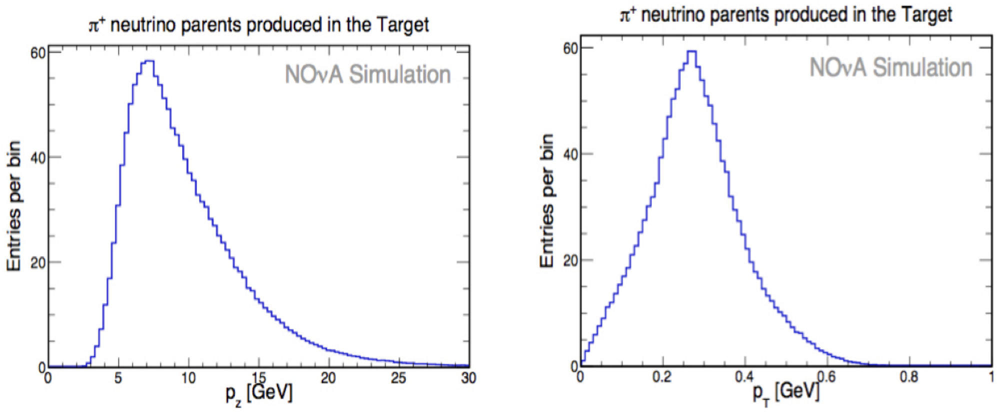

Figure 4.14: p_Z (left) and p_T (right) spectra for parent pions, which give ν_μ in 1-3 GeV energy range.

pions that exit the target volume using G4NuMI and FLUGG simulations. The spectra are somewhat different above 50 GeV but look fairly similar, at this scale, in the region of interest. The ratios of FLUGG to G4NuMI for both cases are shown in Figure 4.15 (lower row) where the region of interest (5 - 11 GeV) is highlighted. The dotted red lines indicate a 10% difference in the FLUGG / G4NuMI ratio.

Similarly, the p_T distributions for π^+ and π^- exiting the target volume are studied using G4NuMI and FLUGG simulations and are shown in Figure 4.16 (upper row) along with the FLUGG/G4NuMI ratio plots in the lower row. The dotted red lines indicate a 10% difference in the FLUGG / G4NuMI ratio and the dotted green lines indicate a 20% difference.

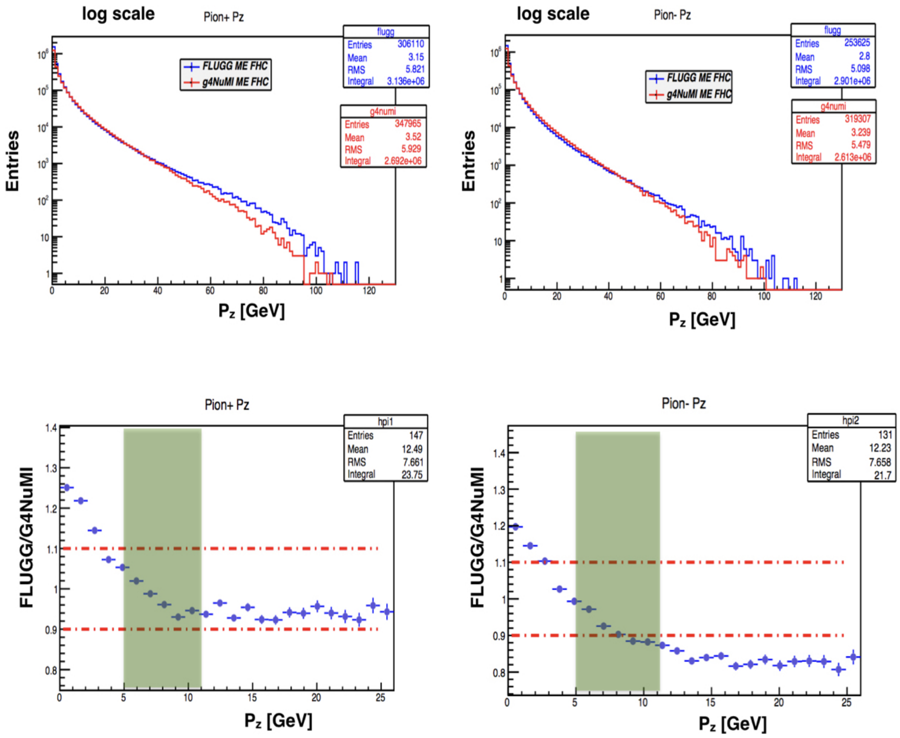

Figure 4.15: (Upper row) p_Z for all the pions (π^+ (left) and π^- (right)) exiting the NOvA target as simulated by FLUGG (blue) and G4NuMI (red). (Lower row) FLUGG / G4NuMI ratio vs p_Z with the region of interest overlay in light green.

The differences between the ratios for π^+ and π^- as seen in the ratio plots in Figure 4.15 (lower row) and Figure 4.16 (lower row) are likely connected to the

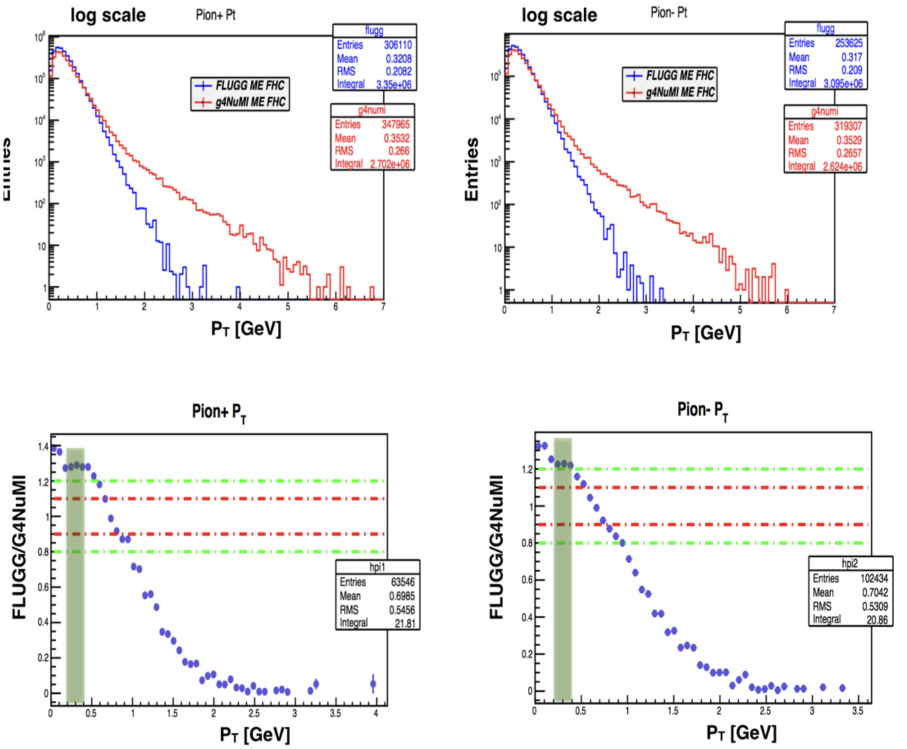

Figure 4.16: (Upper row) p_T for all pions (π^+ (left) and π^- (right)) exiting the NOvA target as simulated by FLUGG (blue) and G4NuMI (red). (Lower row) FLUGG / G4NuMI ratio vs p_T with the region of interest overlay in in light green.

different neutrino event yields predicted by G4NuMI and FLUGG. Overall, Pion production in these two variables is surprisingly different between these two simulators.

4.6.2 Comparing Distributions from the Upstream 12 fins with the Downstream 12 fins in 48 fins NOvA target

From the studies performed in [81], we found that target material closer to the Horn1 produces more neutrino events in 1-3 GeV energy range than the target material far upstream of the Horn1. This subsection digs deeper into the reasons for the difference by comparing pion p_T and p_Z distributions from the last part of target to those from the first part of the target [85].

The standard NOvA target consists of 48 graphite fins and 2 Budal monitors. Here, we compare the momentum distribution of the parent pions coming out of the target with 12 far fins (fins far away from Horn1, upstream part of the target) to those of the target with 12 closer fins (fins closer to the Horn1, downstream part of the target) as shown in Figure 4.17. Both the target configurations have two Budal monitors situated at upstream of the 12 fins.

We compare the p_Z and p_T distributions (See Figure 4.18) of the parent pions, pions that produce neutrinos in 1-3 GeV energy range, using the target with 12 far fins (green) and 12 closer fins (blue). The distributions show a clear difference between the two target configurations in the region of interest (5-11 GeV for p_Z and 0.2-0.4 GeV for p_T) where the target with closer fins configuration shows a gain in the event yield as compare to the target with far fins.

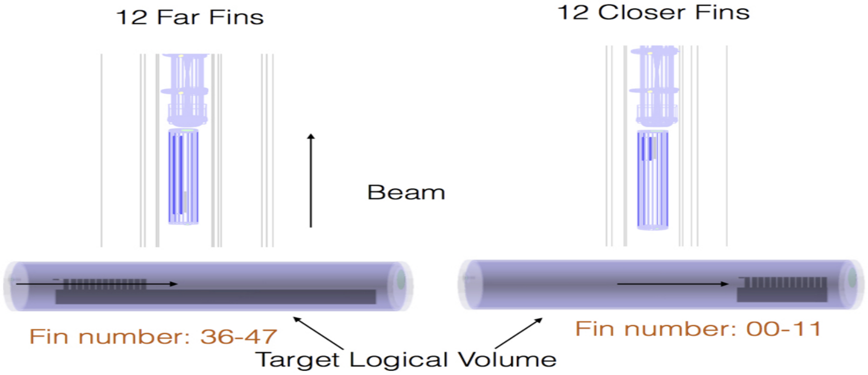

Figure 4.17: Geometry for the NOvA target with different configuration.

In addition, we look at the scatter plots for p_Z vs p_T and is shown in Figure 4.19 for 12 far fins target (left) and 12 closer fins target (right). Figure shows clearly the restricted p_T range for far fins whereas closer fins target configuration covers large p_T range.

We can conclude from the above distributions that the closer fins get more events at low momentum and covers large p_T range in comparison to the far fins target configuration. A quantitative estimation is obtained by comparing the inte-

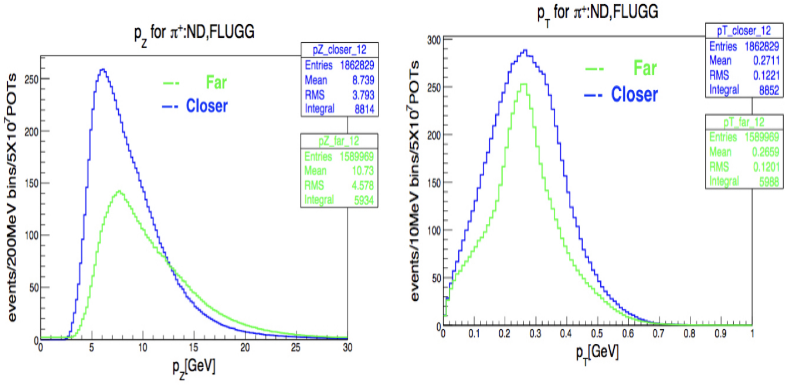

Figure 4.18: Distributions of p_Z (left) and p_T (right) of the parent pions for target with two different configurations, 12 closer fins target (blue) and 12 far fins target (green).

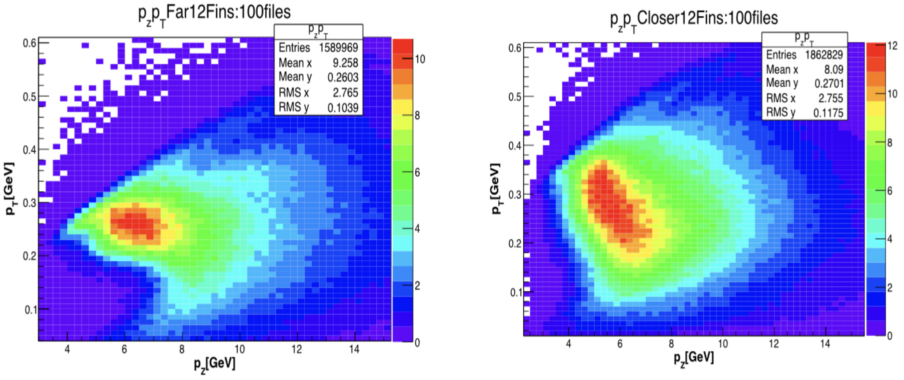

Figure 4.19: p_Z vs p_T distribution of the parent pions using the target with 12 far fins (left) and 12 closer fins (right).

gral from the two different configurations where we have 50% more events from the target with closer fins as compare to the far fins target and hence add much neutrino yield for the NOvA off-axis as compared to the far fins.

4.7 An Amazing Simulation Result

The studies shown in Section 4.5 showed an increase in neutrino yield in the NOvA detectors using shorter targets where the fins were removed from the upstream end of the NOvA target. This increase is observed for both the FHC and RHC beam configurations. Figure 4.20 show that the neutrino yield for 24 fins is about the same as that for 48 fins. In the ME mode, 24 fins give about 93% of the yield of 48 fins. Similarly, In the LE mode, 24 fins give about 97% of the yield of 48 fins [81]. This holds for the NOvA FD and ND yields, for both FHC and RHC, and for both FLUGG and G4NuMI simulations. This is an astounding and unexpected result. The upstream half of the NOvA target is almost useless for off-axis production of neutrinos. This is also reflected in the previous Subsection 4.6.2 where the studies showed that the downstream part of the target gives ∼50% more neutrinos as compared to the upstream part of the target.

These results include the effects of secondary interactions in the target and consequently parent pions of neutrinos come from different places in the target for 48 and 24 fins. If we focus only on primary proton interactions it is easy to calculate the fraction of protons that do not interact at all in the different targets. The NOvA target including the Budal monitors is 50 fins (48 + 2) and about 2.5 interaction lengths of graphite. Using the form e^{-L} (L is in interaction lengths), $e^{-2.5} = 0.08$. In a 26 fins (24 + 2) target, $e^{-1.3} = 0.27$. So in the 50 fins target only 8% of the protons get to the beam dump without interaction, while in a 26 fins target 27% of

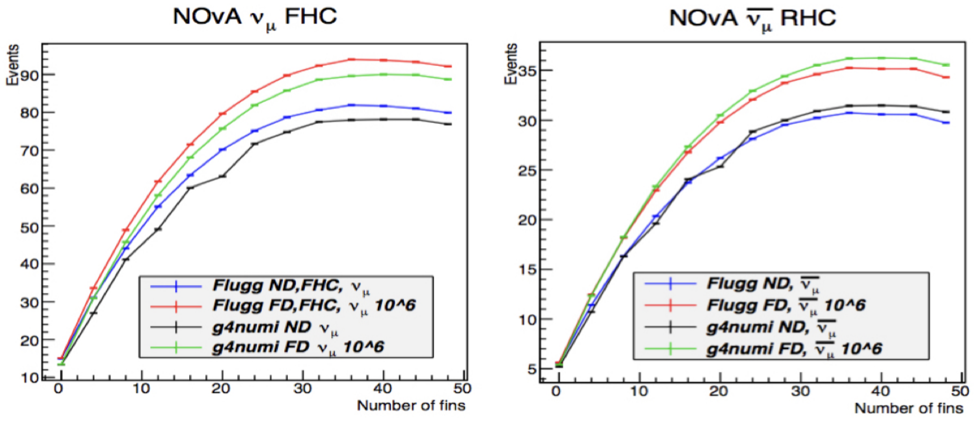

Figure 4.20: Variation in neutrino event yield for changing the number of target fins with Horn2 in ME position for the FHC (left) and RHC (right) beam configurations.

the protons get to the beam dump without interacting.

It seems one effect of the longer target is to protect the beam dump by causing 19% of the proton beam to interact in the first element of the NuMI beam. This means the 700 kW beam has effectively only 567 kW useful for off-axis neutrino production. We need to explore different places we might put the other 24 fins (from the upstream end) so as to enhance off-axis neutrino production.

The studies done in [82] showed that the optimum place to put another 24 fins is inside the Horn1. Next, we discuss briefly various designs for the NOvA target that might help in increasing neutrino yield in the NOvA detectors.

4.8 Design of a New NOvA Target

The studies in the previous section motivated for a new target design that extends inside the Horn1. It is worth mentioning that the standard NOvA target ends at about -20 cm relative to MCZERO and also it can not be inserted inside the Horn1. So, different target designs are explored.

There are five different targets which are designed and simulated to see the effect on neutrino yield in the NOvA detectors as compared to the Standard NOvA target. Here, all the different target designs are introduced and more technical details on the target designs can be found in [82]. The simulation is performed using FLUGG (Version: $FLUGG : 2009\_3$ $FLUKA : fluka2011.2c.4.$).

Figure 4.21 is the XY/beam view of five targets and the standard NOvA target. All the targets are drawn on the same scale.

1. **An Ideal Rod:** The first target design is an Ideal Rod (as shown in Figure 4.21) which is an idealized concept that may not be used in reality in the experiment but can be simulated. The target is made up of one elongated graphite fin and is 122 cm long with the same fin width and height of 7.4

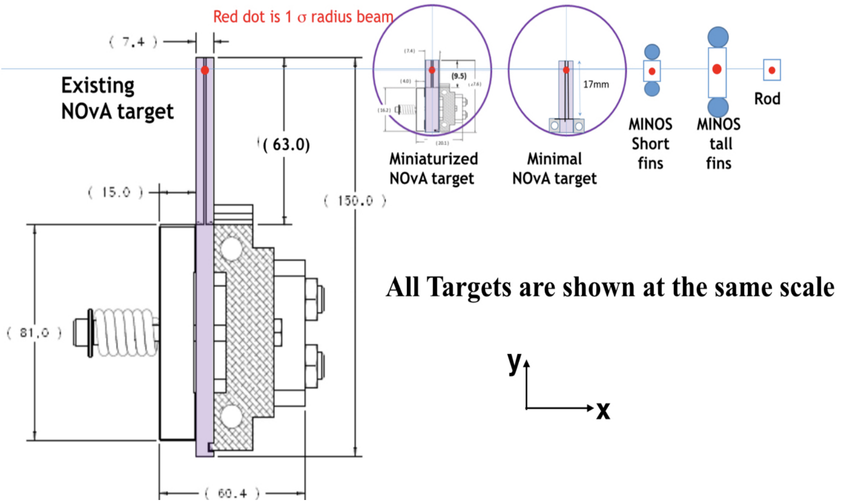

Figure 4.21: A picture showing all the targets at the same scale in XY or Beam view.

mm [82].

2. **The MINOS design:** The second target design is almost similar to the MINOS target design and is shown in Figure 4.21. It is made up of 49 graphite fins and an additional Budal monitor. The total target length is 122 cm. Each fin is 7.4 mm wide and 18 mm high [82].

3. **A MINOS concept with vertically shorter fins:** The third simulated target design is also like MINOS but with vertically shorter fins (See Figure 4.21). Otherwise it has the same features as in the above mentioned MINOS design. Here, the fin height is changed from 18 mm to 7.4 mm keeping everything else exactly the same and at the same position [82].

4. **A Miniaturized NOvA target:** The fourth simulated design is a Miniaturized NOvA target that is a composite target design where we use half of the standard NOvA target with 24-fins (upstream part of a Miniaturized NOvA target) and another half with 24-fins (upstream part of a Miniaturized NOvA target) is just the squeezed version of the standard NOvA target design that

has been shrunk down vertically so that it can be inserted inside Horn1. Both these target parts together form a Miniaturized NOvA target of length 122 cm [82]. In the downstream target part, fin width is kept the same as in the upstream target part that is 7.4mm whereas, fin height is changed from 63 mm to 9.4 mm with the total target height of 19.5 mm. A picture of this target is shown in Figure 4.21.

5. **A new Minimal NOvA target:** The last target design is a Minimal NOvA target that again is a composite target design where we use half of the standard NOvA target with 24-fins (upstream part of a Minimal NOvA target) and the other half with 24-fins (downstream part of a Minimal NOvA target) is a new design or modified version of the standard NOvA target design. In the downstream target part, fin width is 7.4mm whereas, fin height is changed from 63 mm to 17 mm with the total target height of 19.5 mm. The free distance, where the beam interacts, is more in this target design as compared to the Miniaturized target. In this new design, the placement of the cooling tubes is also different as both the tubes go around the target fins [82].

Figure 4.22 shows the YZ view of these targets.

4.8.1 Simulation Results of various targets

First, all the five targets are simulated placed at -20 cm relative to MCZERO using FLUGG software. The neutrino event yield in energy range 1-3 GeV is then compared to the standard NOvA target event yield and is shown below in Figure 4.23. The numbers at the top of each colored bar represents the neutrino event yield at the NOvA FD in the energy range 1-3 GeV which shows that the standard NOvA target (in red) is the best target design if positioned at -20 cm relative to MCZERO. Recall that the Rod is an ideal concept.

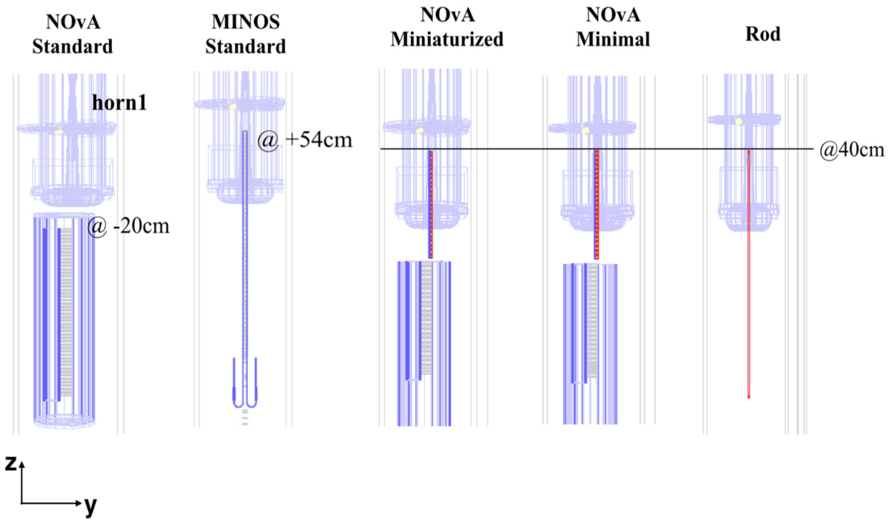

Figure 4.22: A picture showing all the targets in YZ view.

Next, the study similar to section 4.5 is performed to find the optimal target configuration and target position. For this purpose, MINOS design with vertically shorter fins is used as it can be inserted in the Horn1. Four different target configurations (24-fins (64 cm long target), 36-fins (93 cm long target), 48-fins (122 cm long target) and 60-fins (147 cm long target)) are simulated at different positions and results are shown in Figure 4.24. The event numbers represent the neutrino event yield at the NOvA FD in the energy range 1-3 GeV. It is found that, in this case, 48-fins (122 cm long) target is the best target configuration and gives the maximum neutrino event yield if placed at +40 cm (inside Horn1).

Next, all the above mentioned five targets are placed at +40 cm relative to MCZERO inside Horn1 and simulated using FLUGG to study the effect on neutrino event yield. The neutrino event yield at the NOvA FD in 1-3 GeV energy range is shown in the form of histogram below in Figure 4.25. It is found that the Minimal NOvA target is the best target design if placed at +40 cm w.r.t Horn1 where a gain of 11.4% in the neutrino event yield is observed as compared to the standard NOvA target event yield. Rod is an idealized concept.

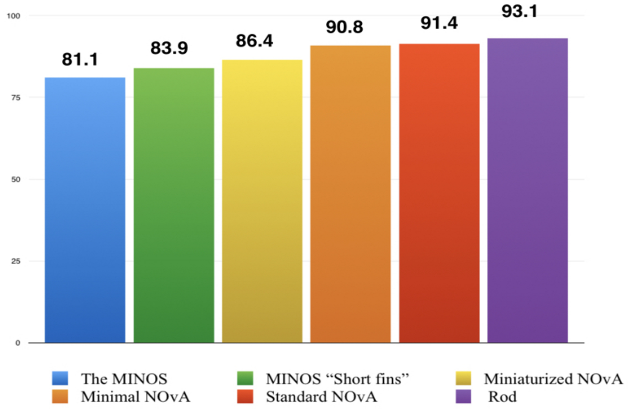

Figure 4.23: Histogram bars represent the neutrino event yield observed at the NOvA FD in the energy range 1-3 GeV.

4.8.2 Minimal NOvA target simulations with different configurations

In the previous section, it is shown that the Minimal NOvA target performs better as compare to all the other targets when placed at +40 cm w.r.t to Horn1. We next study the effect on the neutrino event yield using different target materials and Horn2 configurations with the Minimal NOvA target design only. All the targets discussed previously consist of the graphite fins. From the studies done in [81], targets with Be fins perform better than those with graphite fins with a gain of 3.58% in the neutrino event yield at the NOvA FD. That might be due to the relatively higher density of Be (1.878 g/cc) than the graphite (1.78 g/cc).

In this subsection, we check the effect on neutrino event yield at the NOvA ND and FD using graphite and Be fins Minimal NOvA target and compare the results with the existing standard NOvA target.

1. **Minimal NOvA target with Horn2 in Medium energy (ME) con-**

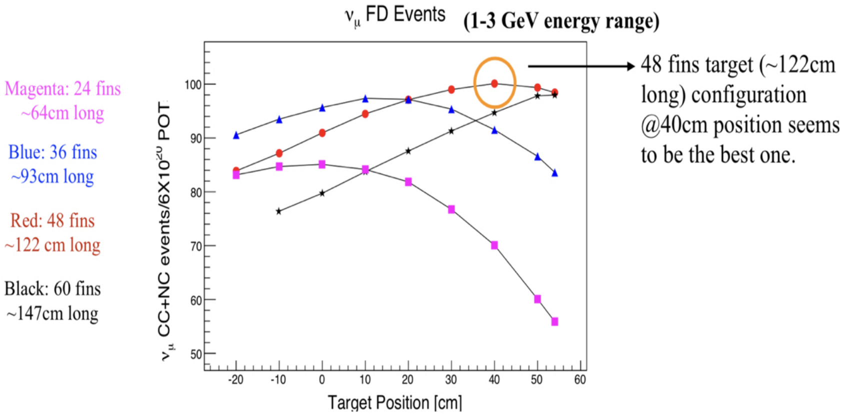

48 fins target (~122cm long) configuration @40cm position seems to be the best one.

Figure 4.24: Distribution of the neutrino event yield at the NOvA FD using different target configurations with target placed at different positions.

figuration The Minimal NOvA target with graphite or Be fins is simulated by placing Horn2 in ME configuration to see the effect on the neutrino event yield at the NOvA ND and FD. It is done for both the FHC and RHC beam configurations and results are shown below in Table 4.6.
Data in table shows that in ME Horn2 configuration both the graphite and Be fins Minimal NOvA targets give higher neutrino (and anti-neutrino) yield as compared to the standard NOvA target. The percent increase in the event yield with Minimal NOvA target w.r.t the standard NOvA target is also shown in the table. As shown in table, the graphite Minimal NOvA target gives 11.4% more neutrinos than the Standard NOvA target in FHC and 11.8% more in RHC. Be is 1.6% higher than graphite in FHC and Be is 4.6% higher than graphite in RHC. The background neutrino yields are also higher but remain small compared to the un-oscillated primary muon neutrino mode.

The NOvA FD FHC neutrino energy spectra for the Minimal NOvA target (for graphite and Be fins) to the standard NOvA graphite target in ME configuration is shown in Figure 4.26. Bottom panel shows the ratio of blue to red curve. There is a gain in events at the 2 GeV peak and a larger event gain

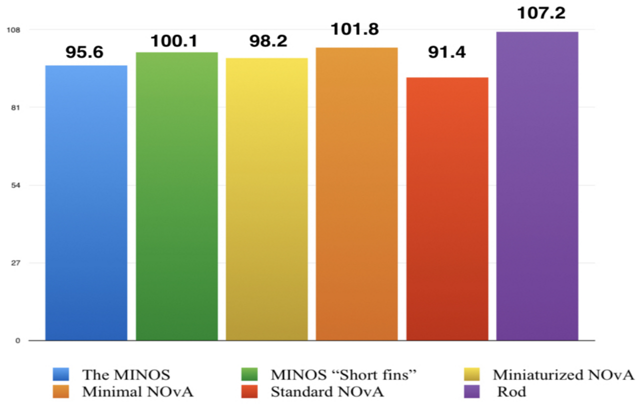

Figure 4.25: Histogram bars represent the neutrino event yield observed at the NOvA FD in the energy range 1-3 GeV.

Table 4.6: Table summarizes the simulation results of the Minimal NOvA target using graphite and Be fins target with Horn2 in ME position.

ME Horn2 configuration	**NOvA FHC**		**NOvA FHC**		**NOvA RHC**		**NOvA RHC**	
	ν_μ		ν_e+$\bar{\nu}_e$+$\bar{\nu}_\mu$		$\bar{\nu}_\mu$		ν_μ+ν_e+$\bar{\nu}_e$	
Target	ND	FD	ND	FD	ND	FD	ND	FD
Standard NOvA	79.2	91.4	2.03	2.2	30.06	34.70	3.7	4.1
Minimal NOvA [C, ME]	88.6	101.8	2.3	2.6	33.5	38.8	4.2	4.7
% change (New/Std)	11.8	11.4	13	18	11.4	11.8	13.5	14.6
Minimal NOvA [Be, ME]	89.9	103.3	2.2	2.5	34.9	40.4	3.8	4.4
% change (New/Std)	13.5	13.0	8	14	16.1	16.4	3	7

at 1-1.5 GeV than at the 2 GeV peak. The NOvA ND spectra and on-axis spectra is also studied and can be found in [86].

Similarly, the comparison is done for the RHC beam configuration and is shown in Figure 4.27.

2. **Minimal NOvA target with Horn2 in Low Energy (LE) configuration** In this subsection, simulation results of the Minimal NOvA target using graphite and Be fins with Horn2 in Low Energy (LE) configuration are presented. Simulations are performed for both the FHC and RHC beam configurations. Simulation results are shown in Table 4.7. Data in table shows that in LE Horn2 configuration both the graphite and Be fins Minimal NOvA targets

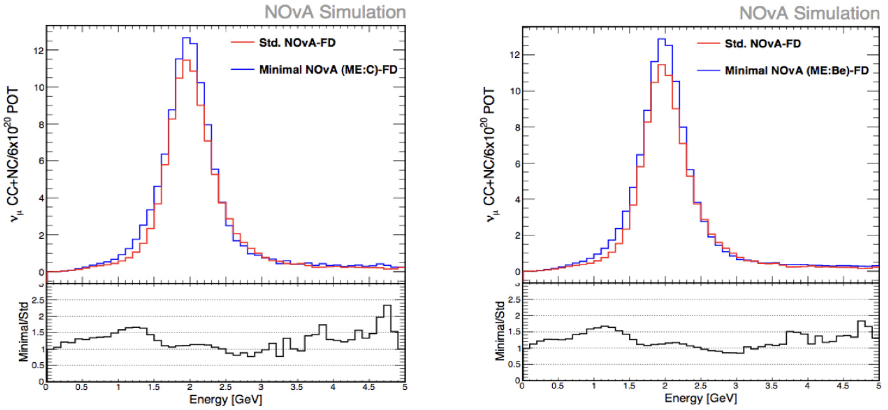

Figure 4.26: FHC neutrino energy spectra for the NOvA FD in the energy range 1-5 GeV for the Minimal NOvA target with graphite fins (left) and Be fins (right).

give higher neutrino (and anti-neutrino) yield when compared to the standard NOvA target in ME mode. This is expected since the Minimal NOvA target is inside Horn1 as it would be for the LE mode. As shown in table, the graphite Minimal target gives 15.9% more neutrinos than the Standard NOvA target in FHC and 17.9% more in RHC. Be is 1.3% higher than graphite in FHC and Be is 2.2% higher than graphite in RHC. The background neutrino yields are also higher but remain small compared to the un-oscillated primary muon neutrino mode.

Table 4.7: Table summarizes the simulation results of the Minimal NOvA target using graphite and Be fins target with Horn2 in Low Energy configuration.

LE Horn2 configuration	**NOvA FHC**		**NOvA FHC**		**NOvA RHC**		**NOvA RHC**	
	ν_μ		$\nu_e+\bar{\nu}_e+\bar{\nu}_\mu$		$\bar{\nu}_\mu$		$\nu_\mu+\nu_e+\bar{\nu}_e$	
Target	ND	FD	ND	FD	ND	FD	ND	FD
Standard NOvA	79.2	91.4	2.03	2.2	30.06	34.70	3.7	4.1
Minimal NOvA [C, LE]	92.9	106	2.5	2.7	36.0	40.9	4.5	5.1
% change (New/Std)	17.3	15.9	23	23	19.8	17.9	22	24
Minimal NOvA [Be, LE]	93.7	107.2	2.5	2.6	36.7	41.7	4.2	4.8
% change (New/Std)	18.3	17.2	23	18	22.0	20.1	14	17

The NOvA FD FHC neutrino energy spectra for the Minimal NOvA target

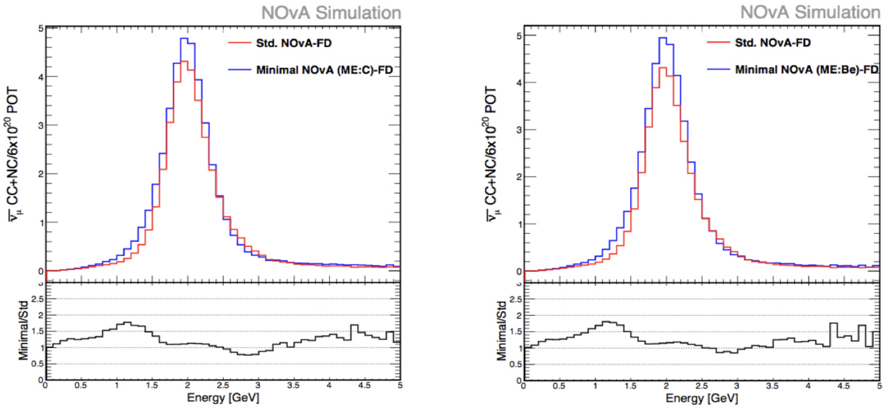

Figure 4.27: RHC anti-neutrino energy spectra for the NOvA FD in the energy range 1-5 GeV for the Minimal NOvA target with graphite fins (left) and Be fins (right).

(for graphite and Be fins) to the standard NOvA graphite target in LE configuration in Figure 4.28. There is a small loss in events at the 2 GeV peak and a large event gain by a factor of 3 at 1.2 GeV. The NOvA ND spectra and on-axis spectra is also studied and can be found in [86].

Similarly, the comparison is done for the RHC beam configuration and is

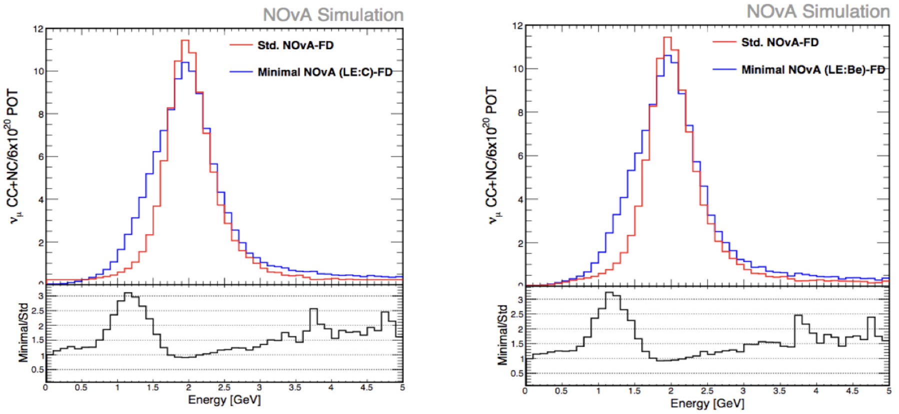

Figure 4.28: FHC neutrino energy distribution for the NOvA FD in the energy range 1-5 GeV for the Minimal NOvA target with graphite fins (left) and Be fins (right).

shown in Figure 4.29.

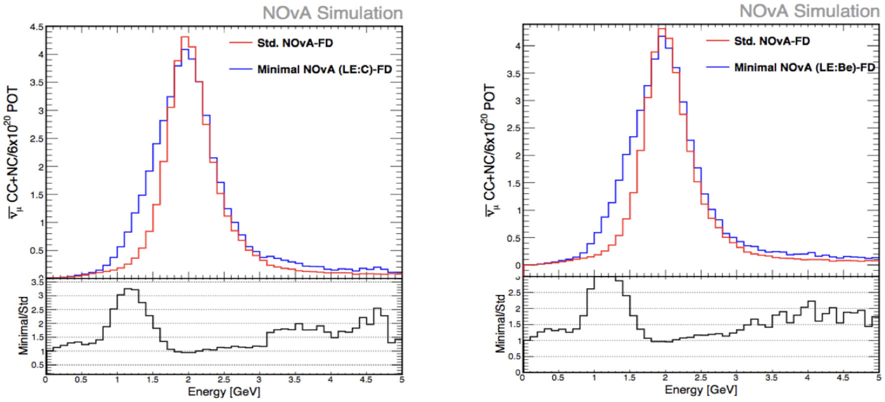

Figure 4.29: RHC anti-neutrino energy distribution for the NOvA FD in the energy range 1-5 GeV for the Minimal NOvA target with graphite fins (left) and Be fins (right).

4.9 The NOvA Target Upgrade for PIP-I+

PIP-I+, Proton Improvement Plan, aims to increase the NuMI intensity to 1.2 MW. Existing NuMI intensity is 700 kW and plan is to increase the intensity gradually to 900 kW and then 1.2 MW. This increased intensity requires a target that is robust at 1.2 MW. It has been estimated that a wider beam spot size with wider fins is required at 900 kW that may be to keep heat under control. Currently, the beam spot size is 1.1 mm with 7.4 mm wider graphite fins. Simulation study is performed, using FLUGG, by changing the NOvA target fin width to 9.0 mm and 10.6 mm with a wider beam spot size, 1.3 mm and 1.5 mm and the results are compared with that of the standard conditions. Figure 4.30 shows the picture of the NOvA target fin (graphite segment) with different fin widths.

Figure 4.31 shows the comparison of the 1-3 GeV neutrino events at the NOvA FD using wider fins and wider beam spot size with the Standard NOvA target conditions. Red curve is with 7.4 mm wide fins, blue curve is with 9.0 mm wide fins and black curve is with 10.6 mm wide fins in the NOvA target. All these curves are drawn using the simulation results obtained at the NOvA FD with three different beam spot sizes, 1.1 mm, 1.3 mm and 1.5 mm. With 900 kW NuMI intensity, target

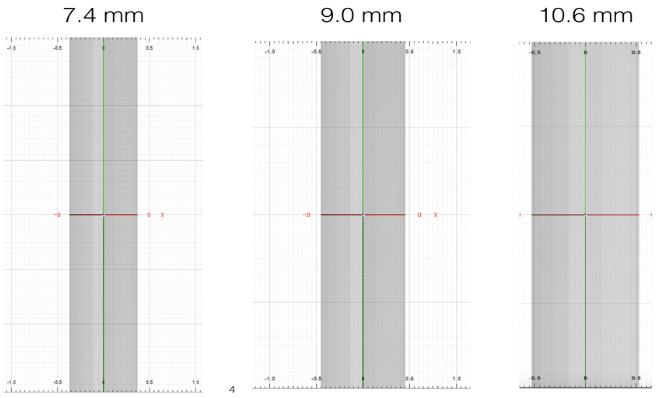

Figure 4.30: Picture of the NOvA target fin (graphite segment) with different fin widths.

needs 9.0 mm wider fins with 1.5 mm beam spot size, where the number of neutrino events at the NOvA FD is reduced by 3% as compare to that with the Standard NOvA target and are marked in the figure in black circle. This decrease in neutrino yield might be tolerable in comparison to 30% increase in the beam power.

Additional studies are performed by reducing the number of fins in the target with 9 mm wider fins and 1.5 mm beam spot size which showed that the shorter target with 40-fins is the optimum configuration [87]. The gain in neutrino yield is 5.7% w.r.t standard NOvA target.

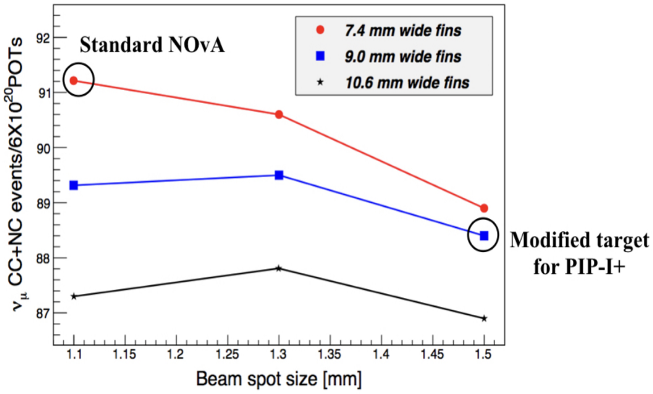

Figure 4.31: Neutrino events in the NOvA FD in energy range 1-3 GeV for the NOvA target with different fin widths and beam spot sizes.

4.10 Summary

In this chapter, the simulation studies which are done to investigate whether there can be a better target and horn configuration for the NOvA, with which better flux of neutrinos and anti-neutrinos can be achieved, are discussed. Shorter targets than the standard NOvA target are found to give more neutrinos. The efficiency of current (standard) NOvA target and horn configuration is studied and determined that the upstream half of the existing NOvA target is providing no additional off-axis neutrino yield. The study is performed with two simulation programs, G4NuMI and FLUGG, which exhibit differences that are summarized in Table 4.3.

Further, as a part of optimization study various new target designs are made and simulated and found the greatest gain in neutrino events from a new Minimal NOvA target design. This study is a part of the systematic study to run NOvA better in near future

Chapter 5

NC π^o Event Selection

This chapter lays out the procedure to select the NC π^o events. As mentioned in chapter 1, NC interactions where a π^o is produced in the final state represent an important background for the experiments looking for ν_e appearance as the neutral pion decaying to two photons may be misidentified as a single electro-magnetic shower.

The challenge is to reconstruct and identify the final state of an interaction to be able to identify the π^o's decay into electromagnetic (EM) showers. In this chapter, the details to select the NC π^o events are discussed.

5.1 Simulation, Reconstruction and Dataset details

NOvA uses GEANT4 to simulate the detector geometry and GENIE (v2-12-10b) [36] to simulate neutrino interactions. Each event in the simulated monte carlo (MC) sample is given a weight which corresponds to kPPFXFluxCVWeight * kXSecCVWgt2018. The former is the re-weighting variable that provides a correction for the hadron production mismodeling using all the relevant data for NuMI [88]. The latter is the cross-section reweighting variable [89] which is used since the default GENIE prediction is insufficient to describe the NOvA ND data. To account for the data excess, observed in the NOvA second run (from February 2014 to May 2016) [91], [61], relative to the GENIE's baseline prediction, a combination of weights is applied to each simulated event. These weights are used by NOvA across all the analysis.

As discussed previously in chapter 3, neutrino interactions in the NOvA ND are reconstructed into slices (clusters of cell hits that are closely related in space and time) [65]. The slices are examined to find the particle paths using a Hough transformation [67]. The information from the intersection of the paths is used to find a neutrino interaction vertex (a point where the primary neutrino interaction takes place). The clusters that correspond to the same shower are reconstructed as prongs. Thus, a prong is defined as a collection of cell hits with a starting point and direction. The prongs are sorted by energy which means the leading prong has most of the energy and is referred to as prong1 whereas, the second-most energetic prong is called prong2. Figure 5.1 shows a ND MC event display with two reconstructed prongs. The top rectangle (XZ view) is the detector view from above, the bottom (YZ view) is the view from side of the detector. The NuMI beam is coming in from the left side. Each pixel in these views is one PVC cell. The color here represents the charge deposited in the detector. The prongs are the 3d prongs, prongs that are matched in both the detector views.

The NOvA ND data are used to perform the cross-section measurement which is equivalent to 8.09×10^{20} protons on target (POT) exposure. The data used were collected over the period of $\sim$3 years from August 16, 2014 to February 20, 2017. The NuMI beam intensity during this period was gradually ramped up to 700 kW from 250 kW. It is important to mention that there are plans to further increase the intensity to 1.2 MW which will provide more POT exposure in near future. The simulation used is run and intensity matched, real conditions Monte-Carlo, where real data taking conditions are simulated using a set of simulation programs as dis-

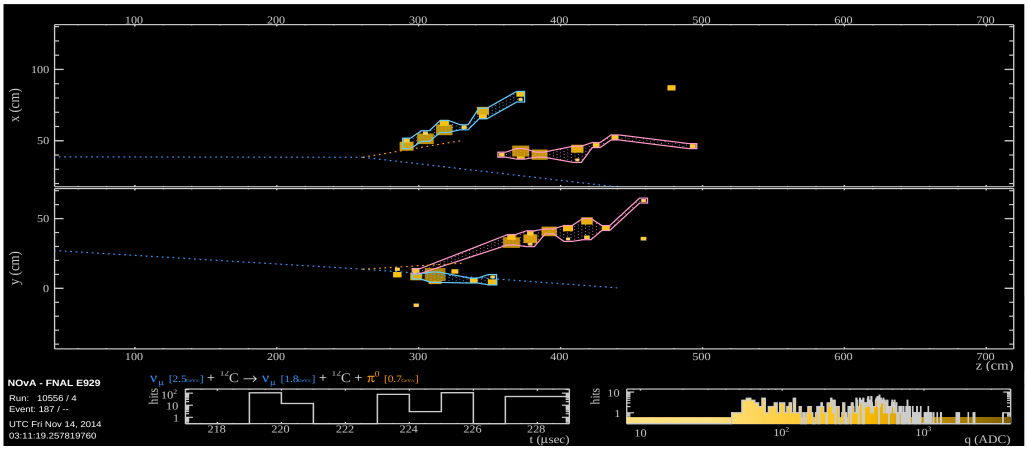

Figure 5.1: An event display that shows two reconstructed prongs in both the detector views, XZ and YZ view. The NuMI beam is coming in from the left side.

cussed in chapter 3. The simulated sample has ∼4x more statistics than data. So, all the distributions with simulated sample are normalized to 8.09×10^{20} POT which reflects the NOvA ND data POT.

5.2 Signal and Background

Signal for this analysis is defined as neutrino induced NC interactions with at least one π^o in the final state. A certain region of phase space is chosen based on the distribution of reconstructed π^o mass vs true π^o kinetic energy (K.E) as is shown in Figure 5.2. Most of the reconstructed signal events are above true K.E 0.1 GeV. For this reason, we set a threshold on true π^o K.E > 0.1 GeV in the signal definition.

Background comes from the neutrino induced CC interactions (CC background) and NC interactions (NC background). The CC background consists of interactions in which the outgoing μ is not identified, and can contain a π^o in the final state or not. The NC background consists of NC interactions without a π^o in the final state and with π^o below true K.E 0.1 GeV.

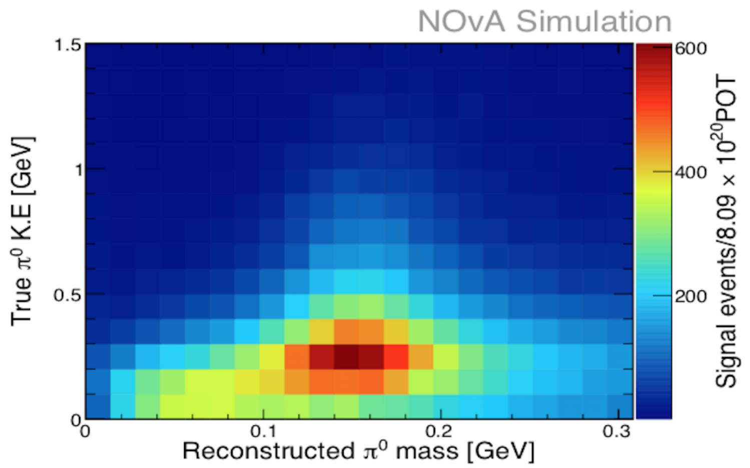

Figure 5.2: π^o true kinetic energy vs reconstructed π^o mass for the signal events.

5.3 Pre-Selection

Pre-selection starts by applying some quality cuts to select the events with number of slice hits above 15 where slice hits are the clusters of cell hits that are closely related in space and time [65]. Then, the reconstructed interaction vertex is required to be inside the NOvA ND fiducial volume and all showers must be contained. The fiducial and containment cuts, that are a part of pre-selection, are chosen based on data-MC comparison [92]. The fiducial bounds are:

$$\begin{aligned} -130 &< vtx.X[cm] < 160 \\ -150 &< vtx.Y[cm] < 120 \\ 225 &< vtx.Z[cm] < 950 \end{aligned} \tag{5.1}$$

Similarly, the bounds for the containment volume are:

$$\begin{aligned} -130 &< shw.stop.X[cm] < 140 \\ -150 &< shw.stop.Y[cm] < 150 \\ 300 &< shw.stop.Z[cm] < 1025 \end{aligned} \tag{5.2}$$

Pre-selection cuts also include the events with exactly two 3D prongs, which comprise 25% of the total signal events. The distribution of number of 3D prongs is shown in Figure 5.3 where, red colored bin represents the number of events with two 3D prongs.

We also include the oscillation analysis muonID (also called as Reconstructed muon identification (ReMId)) [93] in the pre-selection. MuonID/ReMId is a particle identification algorithm specifically based on muon tracks that has been developed to be used in the NOvA's ν_μ disappearance analysis. It selects muons from ν_μ charged current (CC) interactions and gives a value 0 to 1 to an event, where 1 is for CC-like events. Figure 5.4 (left) shows a distribution of ReMID for 2-prong events after fiducial and containment cuts. It shows good separation of CC events (background events in this analysis) from NC. To reject these background events, we choose a cut

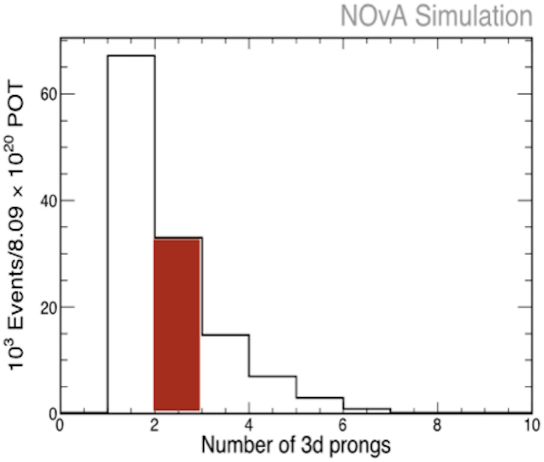

Figure 5.3: Distribution of number of 3d prongs is shown with the fiducial and containment cuts applied.

value on ReMId based on its figure of merit ($\text{FOM} = \text{S}/\sqrt{(}S+B)$, where S is signal events and B is background events) as shown in Figure 5.4 (right). The FOM is maximized at 0.36, so we include MuonID/ReMId < 0.36 in the pre-selection.

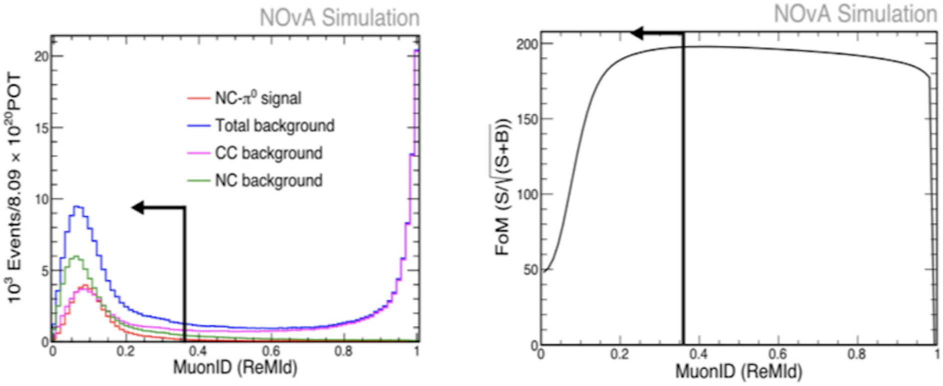

Figure 5.4: (Left) MuonID/ReMId variable distribution for the signal and background events. (Right) Distribution of figure of merit (FOM) evaluated from MuonID/ReMId distribution.

Thus, the pre-selection cuts for this analysis include quality cuts, fiducial, containment, events with 2 prongs and MuonID/ReMId < 0.36.

5.4 Event Selection

We develop an event identification algorithm to select the NC π^o events. It is based on a Multivariate algorithm called a Gradient Boosted Decision Tree (BDTG) [94]. The network is trained using the variables that characterize the electro-magnetic shower properties. Further, the variables associated to the leading prong (which has most of the energy) are selected as they showed comparatively better separation between the signal and background than the sub-leading prong variables.

Additionally, we use NOvA's event level Convolutional Visual Network (CVN) algorithm to identify neutrino interactions, based on their topology [95]. Four separate

CVN classifiers are developed based on the interaction types, ν_μ CC, ν_e CC, ν_τ CC and ν NC as also discussed in chapter 3. We include two of them amongst the input variables to train the BDTG. Various studies are performed to train this algorithm using different sets of variables [96], [97]. Finally, the algorithm used 9 input variables in the training phase which are mentioned below:

1. **Prong1 missing planes or Prong1 Maximum gap:** The number of planes without any hits from the leading prong. It is related to the feature that π^o leaves a gap before decaying to two photons that shower electromagnetically.
2. **Prong1 contiguous planes:** The number of continuous planes with hits from the leading prong.
3. **Prong1 width:** The width of the leading prong in cm.
4. **Prong2 dE/dx:** Average energy loss by the sub-leading prong in GeV/cm.
5. **Prong1 e-π^o LLL and Prong1 e-π LLL:** electron-π^o and electron-π log-likelihood for the longitudinal shower (LLL) where a measurement is performed plane by plane.
6. **Prong1 e-p LLT:** electron-proton log-likelihood for the transverse shower (LLT) where a measurement is performed cell by cell.
7. **CVN ν_μ CC:** In CC interactions, the final state has a muon and hadronic component where muon is characterized by long, low dE/dx track. The classifier gives a value 0 to 1 to an event where, 1 is for ν_μ CC like events. This classifier is chosen so as to get some separation of CC background from the rest.
8. **CVN ν NC:** In NC interactions, the final state has a neutrino which can not be detected and a visible hadronic component. The classifier gives a value 0 to 1 to an event where, 1 is for NC like events.

Distributions of input variables for the signal and background events are shown in Figure 5.5. All the plots are area normalized. The variables don't have much correlation with each other as is shown in the correlation matrices in Figure 5.6 that are generated from the multivariate algorithm itself. The correlation matrices are obtained separately for the signal and background events.

The output after BDTG training is obtained using the weights which are assigned to each of the input variables in the training phase and we call the output as NC π^o ID. The distribution of NC π^o ID for the signal and background events with pre-selection cuts is shown in Figure 5.7. It gives a nice separation between the signal and total background with signal (background) dominated towards the higher (lower) value of NC π^o ID. Another notable feature of the NC π^o ID is the reduced

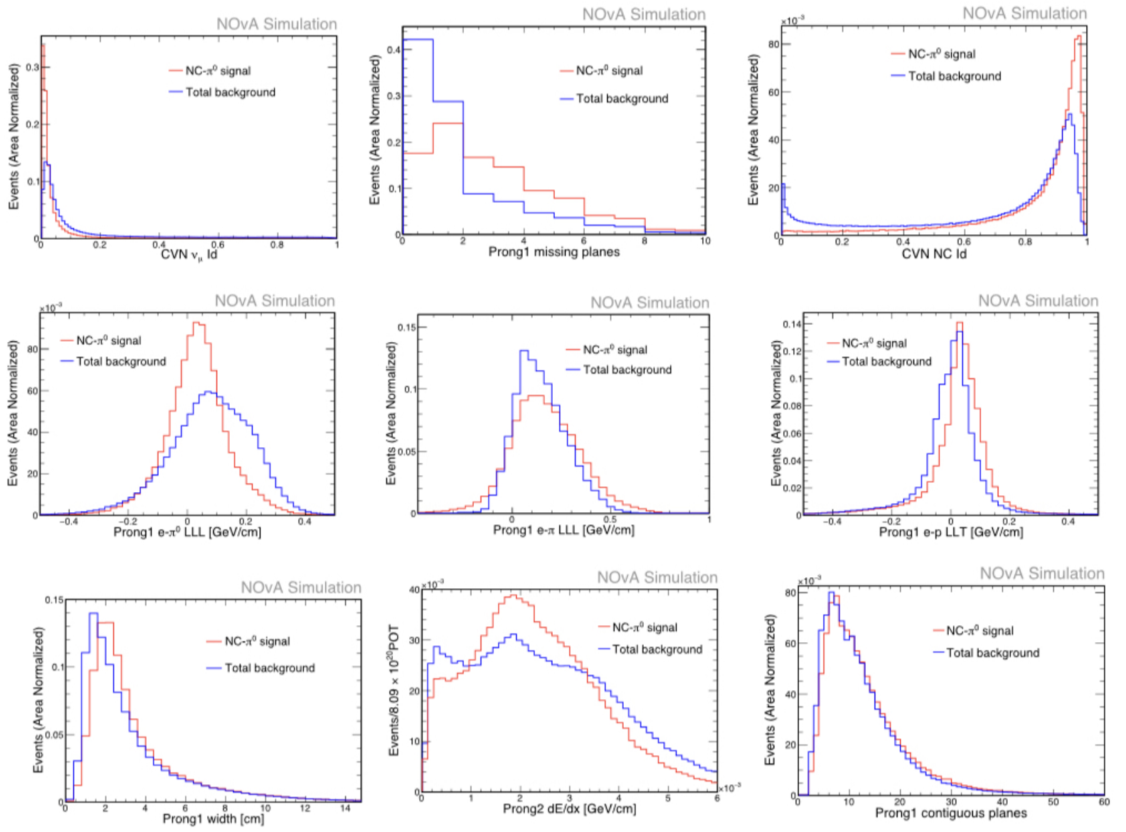

Figure 5.5: Distribution of input variables for the signal (Blue) and background (Red) events with pre-selection.

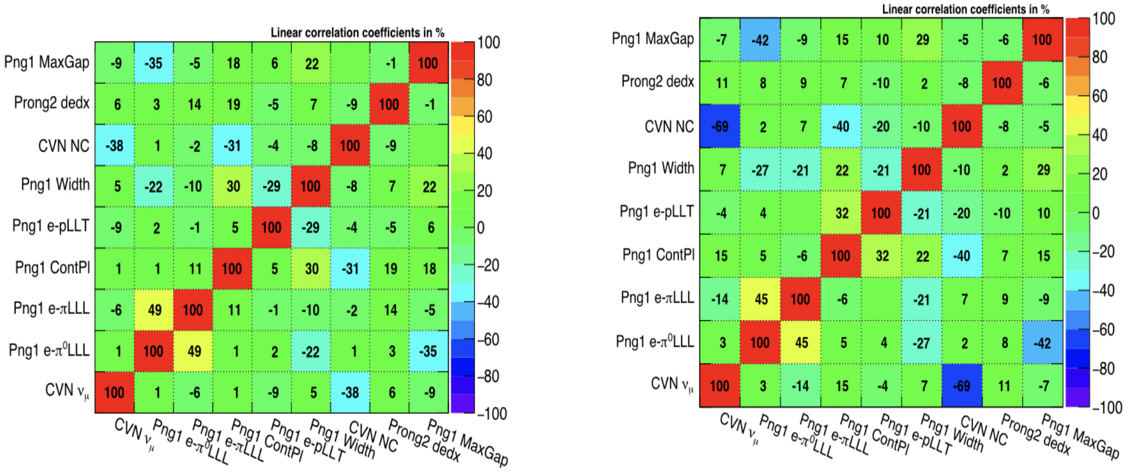

Figure 5.6: Correlation matrices for the signal (left) and background (right). Matrices represent the correlation among the input variables.

CC background in the signal dominated region as most of the CC-like events are populated towards lower values of NC π^o ID. An optimum cut value on NC π^o ID is chosen to select the NC π^o events with high purity.

The strategy for choosing a cut on the NC π^o ID is based on minimizing the fractional uncertainty on the total cross section. We start with the basic cross-section equation:

$$\sigma = \frac{N_{sel} - N_{bkgd}}{\epsilon \times \phi \times N_{target}}, \tag{5.3}$$

where N_{sel} and N_{bkgd} are the selected and background events respectively, ϵ is the efficiency, ϕ is the neutrino flux and N_{target} is the number of target nucleons. If we ignore uncertainties on the flux and assume the fixed number of targets, then the fractional uncertainty is given by:

$$\frac{\delta\sigma}{\sigma} = \sqrt{\frac{N_{bkg} + (\delta N_{bkg}^{syst})^2}{(N_{sel} - N_{bkg})^2} + (\frac{\delta\epsilon}{\epsilon})^2 + \frac{N_{sel}}{(N_{sel} - N_{bkg})^2}}, \tag{5.4}$$

where the first term on the right hand side accounts for statistical and systematic uncertainties on the background events, the second term is the fractional uncertainty

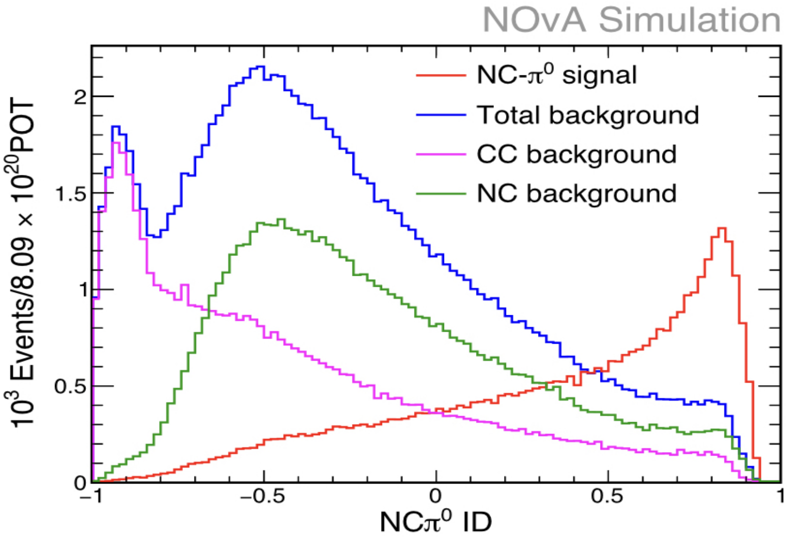

Figure 5.7: BDTG output, NC π^o ID, distributions for the signal (Red) and background (Blue) with pre-selection cuts. The total background is broken down into CC background (Magenta) and NC background (Green).

on the selection efficiency and the third term is statistical uncertainty on the selected number of events. The systematic samples used are detector response, cross section and flux systematics and more details on these are in the next chapter.

Figure 5.8 (left) shows the fractional uncertainty on the total cross section vs NC π^o ID cut value. The minimum is seen at around 0.9 cut value but as shown in Figure 5.7 there are not any signal events beyond 0.9. So, we look for the second minimum value for $\frac{\delta\sigma}{\sigma}$ curve which is obtained with NC π^o ID cut value at 0.6, where the fractional uncertainty on the cross section is 7.5%.

With the pre-selection and NC π^o ID > 0.6, the distribution of reconstructed π^o mass for the signal and background events is shown in Figure 5.8 (Right). Reconstructed π^o mass is calculated using equation 5.5:

$$M_{\pi^o} = \sqrt{2E_{\gamma 1}E_{\gamma 2}(1 - Cos\theta)} \tag{5.5}$$

where, $E_{\gamma 1}$ and $E_{\gamma 2}$ are the prong1 and prong2 energy and θ is the angle between two prongs.

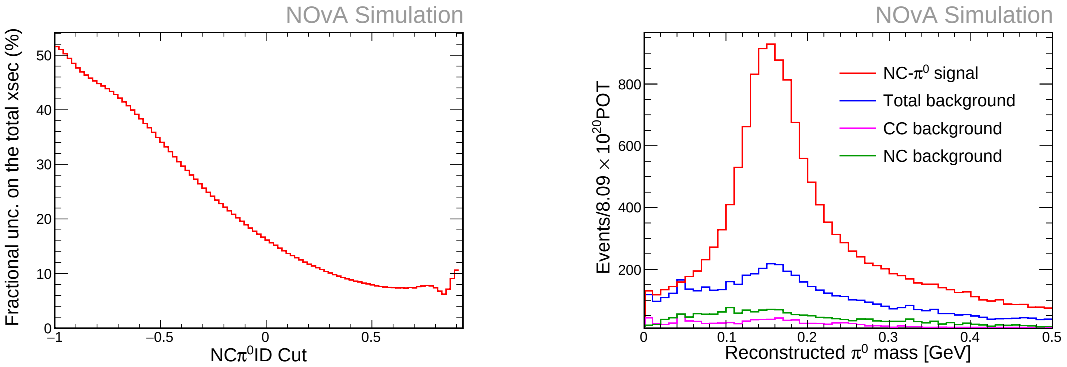

Figure 5.8: (Left) Fractional uncertainty on the total cross section vs NC π^o ID cut value. (Right) Distribution of π^o mass for the signal (Red) and total background (Blue) events with NC background (Green) and CC background components.

π^o mass distribution shows a very nice separation of the signal (red) from the total background (blue) with a clean π^o mass peak. The background is dominated by the NC interactions without π^o and with π^o below energy threshold, 0.1 GeV. The signal is dominated by 61% RES events along with 24% DIS events, 14% coherent and a small percent of QE events.

Table 5.1 shows the signal and background event counts at each cut level. The selection cuts reject 99.9% of the total background events w.r.t the background events in fiducial volume as shown in column 4 of the Table 5.1. It provides a pure signal with 77% purity and 5.6% efficiency. The efficiency is w.r.t the signal events in true fiducial.

Table 5.1: Event counts showing an impact of each cut on the signal and background events.

Cut	Signal (S)	Background (B)	B Rejection (%)	Efficiency(%)	Purity(%)
True fiducial	242155.34	2511619.2	-	-	-
Fid+Cont.	79910.37	858609.58	65.8	33	8.5
2-prongs	41194.71	228315.06	90.9	17	15.3
ReMId < 0.36	33294.37	85945.08	96.5	14	27.9
NC π^o ID > 0.6	13526.99	4108.27	99.9	5.6	76.7

5.5 Summary

The selection criteria used to select the NC π^o events of interest is discussed in detail. An event ID is developed to select a pure sample of NC π^o events. A cut on event ID, in addition to the pre-selection cuts, is able to reject 99.9% of the total background as seen in the previous section and a clean π^o mass peak is seen. Selecting events of interest is an important step in making a cross-section measurement. The details of measuring cross section are discussed in the next chapter.

Chapter 6

Cross-section Measurement

This chapter discusses the analysis details of measuring NC π^o production cross section as well as differential cross-section measurement. The event ID which was developed using multivariate algorithms in the previous chapter is the starting point of this chapter. It is used to estimate the signal and background which is a very important step in making the cross-section measurement. The true signal is then estimated using the unfolding matrix (U) that corrects the reconstructed quantities for detector resolution and smearing, and provides an estimate of signal content in true space. These are addressed taking all the systematics into account.

6.1 Signal and Background Estimation

The standard cross section equation is:

$$\sigma = \frac{N^{sel} - N^{bkgd}}{N_{Target}\phi\epsilon} = \frac{N^{sig}}{N_{Target}\phi\epsilon}, \tag{6.1}$$

where σ is the cross-section, N^{sel}, N^{bkgd} and N^{sig} are the numbers of selected events, background events and signal events respectively. N^{bkgd} and N^{sig} are estimated from the template fit that include all the systematics into account and is discussed in this section. N_{Target} is the number of target nucleons, ϕ is the flux, and ϵ is the signal selection efficiency and will be discussed later in this chapter.

The signal and background for this analysis are estimated using data-driven methods. The eventID, NC π^o ID, shows a good separation between the signal and background events (See Figure 5.7) which are dominated in different regions of phase space. The simulation describes shape of the NC π^o ID well which is verified by varying different GENIE knobs with systematic shift $\pm 1\sigma$ [98].

The signal and background estimation is done by fitting the total signal, NC background and CC background components of NC π^o ID to the fake-data. Fake data refers to 1/4 of the total MC with shifts and weights applied. The reason for choosing 1/4 of the total MC as fake-data is that it has POT equivalent to the data. A three parameter fit is chosen which will provide three normalization parameters for the signal, NC background and CC background. This information is further used to obtain the signal estimate to calculate the flux-averaged NC π^o production cross-section. The parameter values (the normalization for the three parameters) are determined by minimizing a chi-square which is defined as:

$$\chi^2 = (Data_i - MC_i)^T V_{ij}^{-1} (Data_j - MC_j), \tag{6.2}$$

where

$$MC_i = (par0 * (Signal)_i + par1 * (CCbkgd)_i + par2 * (NCbkgd)_i), \tag{6.3}$$

i runs over the number of NC π^o ID bins.

V_{ij} is the covariance matrix, a simple linear addition of statistical and systematic covariance matrices:

$$V_{ij} = V_{ij}^{stat} + V_{ij}^{syst}. \tag{6.4}$$

The statistical covariance matrix, V_{ij}^{stat}, is a diagonal matrix where each diagonal element is the statistical variance in the corresponding NC π^o ID bins such as:

$$V_{ij}^{stat} = \sigma_{MC}^2 + \sigma_{Data}^2. \tag{6.5}$$

The systematic covariance matrix, V_{ij}^{syst}, takes the systematic uncertainties in the NC π^o ID bins into account. The systematic samples used in this analysis are detector response, cross-section and flux systematics with systematic shift $\pm 1\sigma$. The errors from the systematic samples with $\pm 1\sigma$ shift w.r.t the nominal is calculated using the formula:

$$Error_i = \frac{|\sigma_i^{+1} - \sigma_i^{nominal}| + |\sigma_i^{-1} - \sigma_i^{nominal}|}{2}. \tag{6.6}$$

The number of events in the NC π^o ID are extrapolated to an arbitrary shift in each of the systematic samples calculated from the errors as defined in the above equation:

$$f_i = f_{nominal,i} + Error_i. \tag{6.7}$$

The covariance matrix elements are determined by throwing 1000 pseudo experiments where in each experiment, shift for each systematic is pulled randomly from gaussian distribution [99]. The covariance between the systematic uncertainties in the NC π^o ID bins is calculated using the following expression:

$$V_{ij}^{syst} =< f_i f_j > - < f_i >< f_j > . \tag{6.8}$$

For the minimization procedure, we use TMinuit package which is implemented in ROOT [64] and has many algorithms. Starting from the SIMPLEX algorithm to determine a starting point we then use MIGRAD, SEEK and MINOS that provide the best error estimates. The fit is performed in the bins with more than 20 events.

6.1.1 Fit results

First, the fitting procedure using a statistically independent fake-data sample, which is 1/4 of the total MC, is tested. Then, various weights and shifts are applied to the 1/4 of the total MC sample to generate different fake-data samples. For instance, the second fake-data sample is generated by shifting M_a NCRes component by $+1\sigma$ which should affect both the signal and background. Then, the signal and background components are weighted by +10% to generate two more fake-data samples. The fit takes covariance matrix, that takes covariance between the systematic uncertainties in the bins of NC π^o ID into account, as an input and is shown in Figure 6.1.

Table 6.1 shows the fit results with different fake-data samples and it gives expected results. For instance, signal weighted fake-data sample is affecting only the signal by +10% whereas, background weighted fake-data sample is affecting background components. However, M_a NCRes shifted fake-data sample affects both the signal and background. NC π^o ID distributions for the signal, background and total-MC

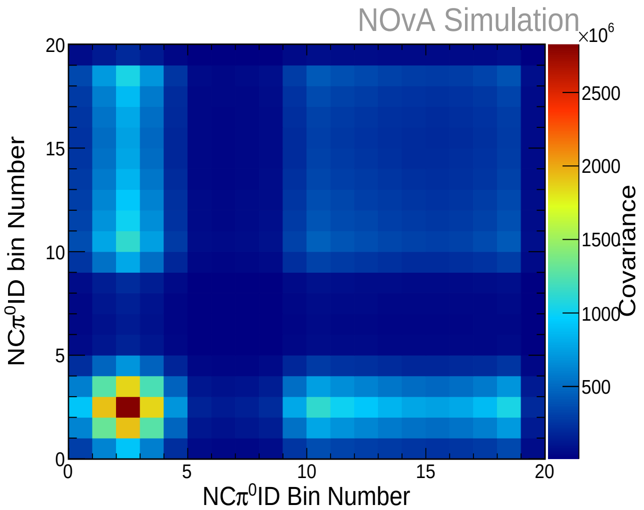

Figure 6.1: Covariance matrix is shown for the NC π^o ID bins that takes covariance between the systematic uncertainties into account.

before and after scaling are also compared [92]. The fit seems to perform very well and gives reasonable results with various fake-data samples. Same procedure will be used with the ND data to estimated the background and signal for making an absolute cross-section measurement.

Table 6.1: Table shows the normalizations determined by fit for the signal, CC-background and NC-background components.

Sample	Signal	CC bkgd	NC bkgd
Stat.Ind	0.98 ± 1.27%	0.99 ± 1.15%	1.01 ± 1.25%
M_aNCRes $+1\sigma$	1.38 ± 1.37%	0.99 ± 0.96%	1.21 ± 1.1%
Sig +10%	1.09 ± 1.3%	0.99 ± 1.1%	1.01 ± 1.3%
Bkg +10%	0.98 ± 1.6%	1.09 ± 1.4%	1.1 ± 1.8%

Since this analysis also plans to report differential measurement w.r.t the final state π^o kinematic variables, so the next step is to study the π^o kinematic variable distributions and estimate signal and background using the covariance matrix method as discussed in this section.

6.2 Kinematic Distributions and Analysis Bins

The distributions of π^o kinematic variables, π^o K.E and angle of π^o w.r.t beam direction ($cos\theta$), in reco and true space are compared as shown in Figure 6.2. These distributions are with the pre-selection cuts (Quality cuts, fiducial, containments, 2-prongs and MuonId<0.36 as discussed in Chapter 5).

Reco space refers to the distributions at detector level which pass all the reconstruction stages whereas, true space refers to the distributions at generator level. There are some differences between the reco and true π^o K.E as shown in Figure 6.2 (left) whereas, for $cos\theta$ (in right) they seem to match better.

The analysis bins for the π^o K.E and $cos\theta$ are chosen by studying the resolution

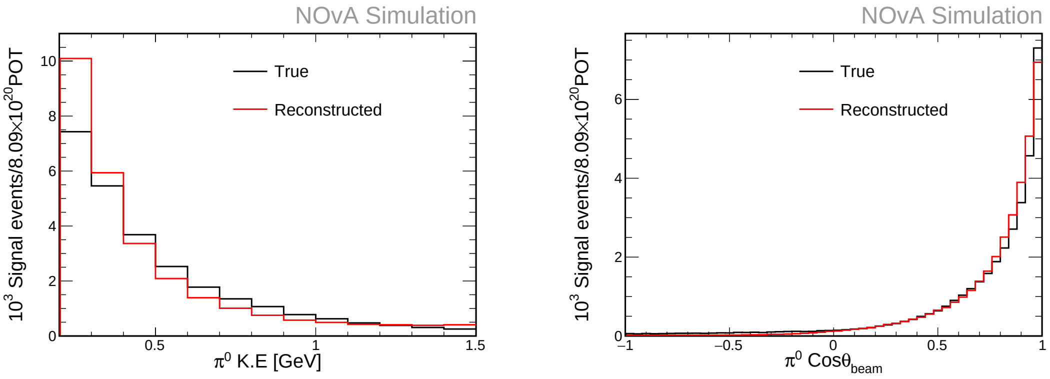

Figure 6.2: Distributions of π^o K.E (left) and π^o angle w.r.t beam (right) in reco and true space are shown with pre-selection cuts applied.

as shown in Figure 6.3 and statistics in each bin. The bins are required to be wide enough as resolution and there must be enough statistics in each of the analysis bins.

The following bin edges for the π^o K.E and π^o $cos\theta$ are chosen based on both resolution and statistics.

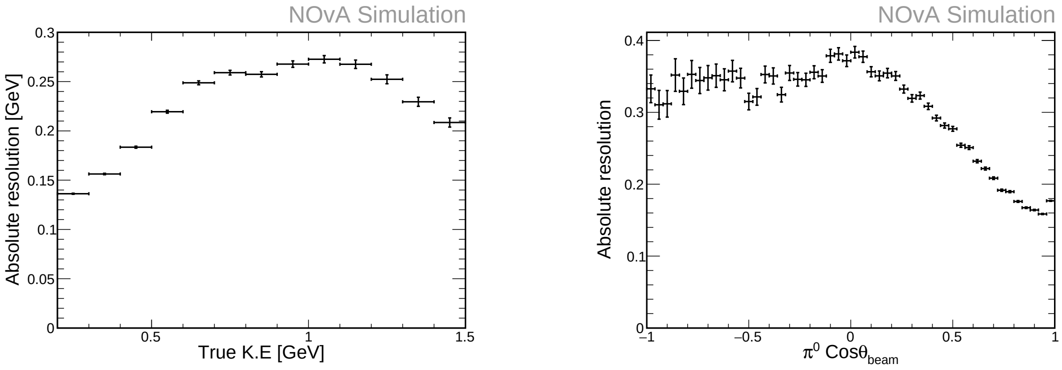

Figure 6.3: Absolute resolution in the bins of true π^o K.E (left) and π^o $cos\theta$ (right).

- π^o K.E: 0.2, 0.3, 0.4, 0.55, 0.8, 1.5
- π^o $cos\theta$: 0, 0.6, 0.8, 0.9, 1.0

The distributions of selected events for π^o K.E and $cos\theta$ are shown in Figure 6.4. The number of events in each bin are divided by the bin width and are normalized to 8.09× 10^{20} POT which reflects the ND data POT.

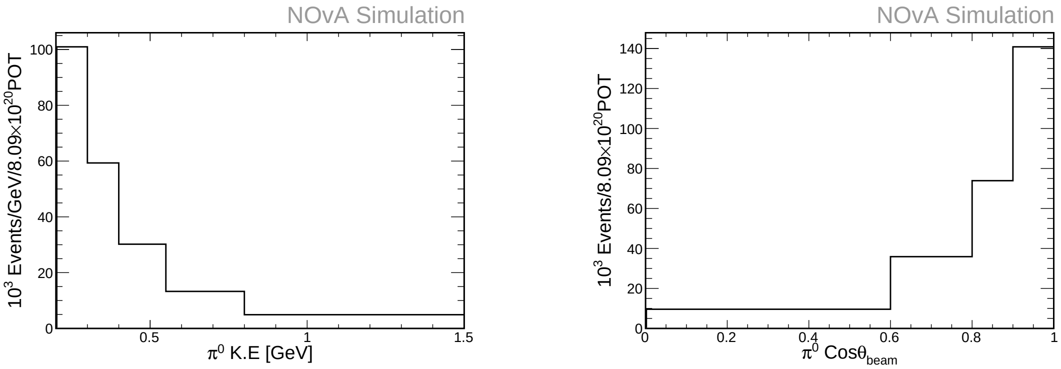

Figure 6.4: The distribution of events for π^o K.E (left) and π^o $cos\theta$ (right) is shown in the analysis bins. The events in each bin are divided by the bin width.

6.3 Signal and Background Estimation in the analysis bins

The differential cross section w.r.t the π^o kinematics is written as:

$$\frac{d\sigma}{dx} = \frac{U(N^{sel}(x) - N^{bkgd}(x))}{N_{Target}\phi\epsilon(x)dx}, \tag{6.9}$$

where x is the variable w.r.t which cross-section is measured. N^{sel} and N^{bkgd} are the numbers of selected events and background events respectively in the bins of x measured in reconstructed space. In this section, the signal and background in each of the analysis bins are estimated using data-driven methods as discussed in section 6.1. The parameter values (the normalization for the three parameters) are determined by minimizing a chi-square which is defined as:

$$\chi^2 = (Data_i - MC_i)^T V_{ij}^{-1}(Data_j - MC_j). \tag{6.10}$$

whereas all the details are discussed in section 6.1.
The covariance matrices, input to the fit, in all the bins of π^o K.E and π^o $cos\theta$ are shown in Figures 6.5 and 6.6 respectively.

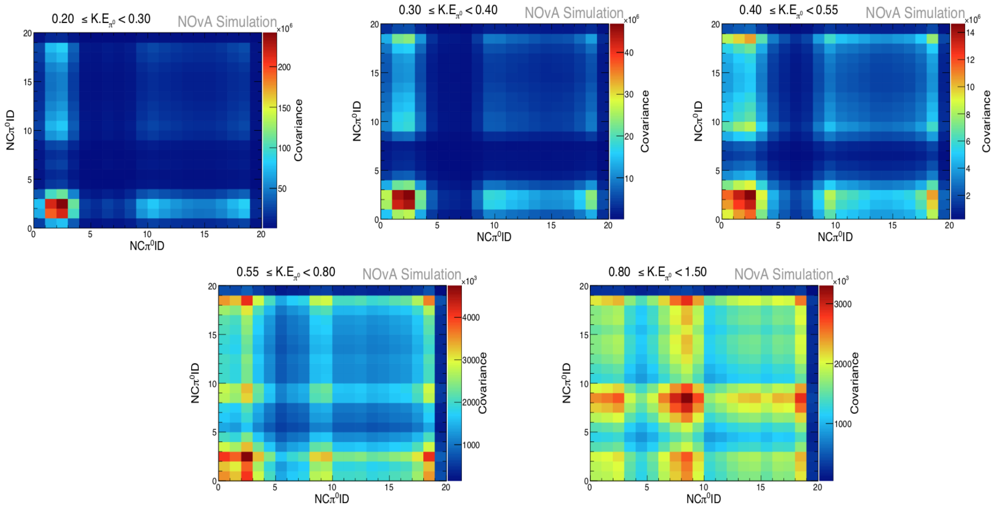

Figure 6.5: Figure shows the covariance matrix in π^o K.E bins. x-axis and y-axis are the NC π^o ID bin numbers.

6.3.1 Fit results in analysis bins

The fit is performed in the analysis bins taking covariance matrix into account. As discussed in section 6.1, fit is first performed using fake-data samples. For this study statistically independent fake-data sample, signal and background weighted fake-data samples are used (see section 6.1). NC π^o ID distributions in each of the π^o K.E and π^o $cos\theta$ bins are studied, for various fake-data samples, before and after the fit [92]. Figure 6.7 shows one such example of the NC π^o ID distributions for a single bin of π^o K.E and $cos\theta$ and compare the signal, background and total MC distribution of NC π^o ID before and after fit. The fit is performed using statistically independent fake-data sample obtained from 1/4 of the total MC.

Similarly, for signal and background weighted fake-data samples the fit results are used to study NC π^o ID distributions in each of the analysis bins [92]. Figures 6.8 and 6.9 show the NC π^o ID distributions for a single bin of π^o K.E and $cos\theta$ and compare the signal, background and total MC distribution of NC π^o ID before and after fit where fit is performed using signal weighted and background weighted fake-data samples respectively.

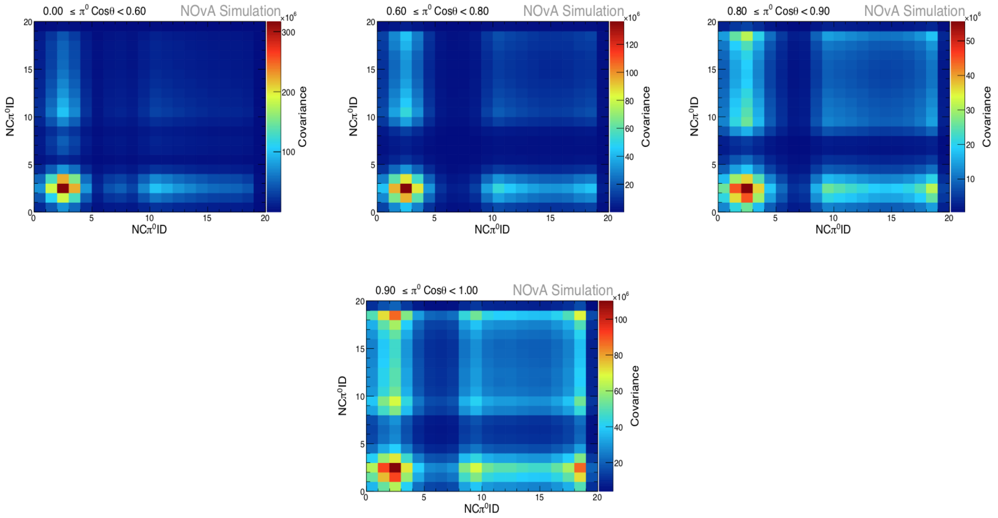

Figure 6.6: Figure shows the covariance matrix in π^o $cos\theta$ bins. x-axis and y-axis are the NC π^o ID bin numbers.

The fitting procedure is further checked with various other fake-data samples where systematic shifts are applied to 1/4 of the total MC and all of them gave reasonable results, details of which are found in [100].

6.4 Unfolding

Unfolding is used to remove the known detector effects which result in differences between the observations and expectations. Most of the measurements in high energy physics, mainly in the cross-section measurements, are based on the event counts which might have statistical fluctuations and moreover, the observables are measured with limited efficiency which results in the distorted or smeared distributions. Unfolding takes out these effects of smearing in order to obtain the true underlying distribution of an observable. There are various unfolding algorithms that work differently.

In this analysis, we unfold the background subtracted signal estimate using Iterative unfolding algorithm [101]. Response matrix, reco vs true observable quantity, is input to the unfolding algorithm which is shown in Figure 6.10 for π^o K.E and

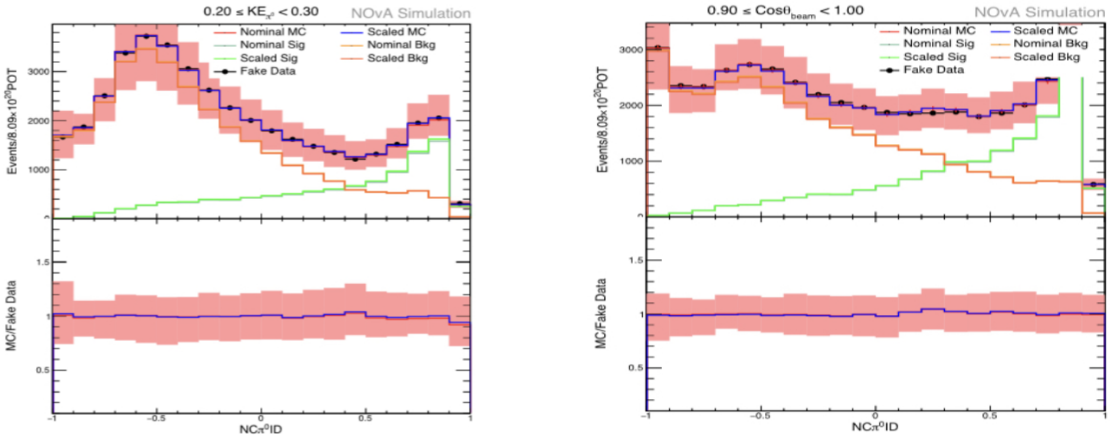

Figure 6.7: NC π^o ID distributions for the signal, background and total MC are shown in the first π^o K.E bin (left) and last π^o $cos\theta$ bin (right) before and after fit. The black points are for the statistically independent fake-data sample.

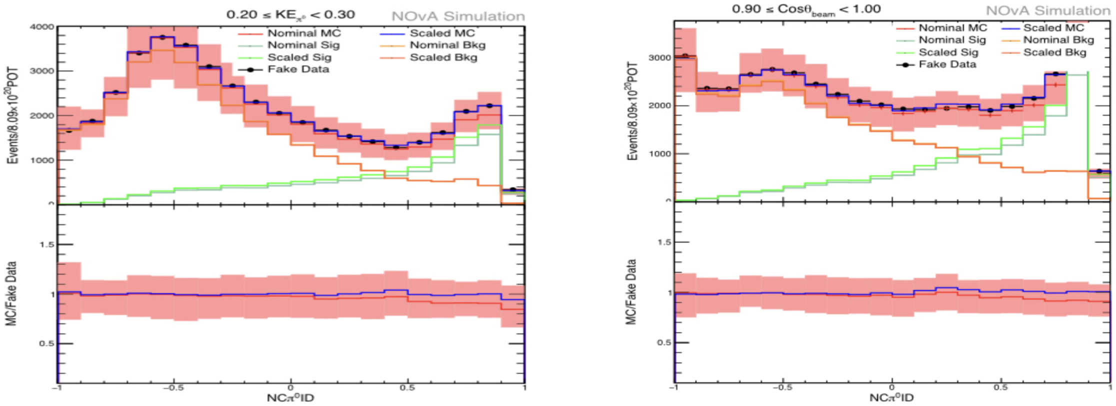

Figure 6.8: NC π^o ID distributions for the signal, background and total MC are shown in the first π^o K.E bin (left) and last π^o $cos\theta$ bin (right) before and after fit. The black points are for the signal weighted fake-data sample.

π^o $cos\theta$.

Signal estimate in reco space re-weights the response matrix a set number of times and then is projected on to true variable in the weighted response matrix. The number of times signal estimate re-weights the response matrix is termed as iterations/regularization parameter. A low value of regularization parameter biases the result towards the input truth whereas, a high value introduces large variance which does not guarantee a good prediction of truth [101].

This analysis makes use of average global correlation coefficient to optimize the

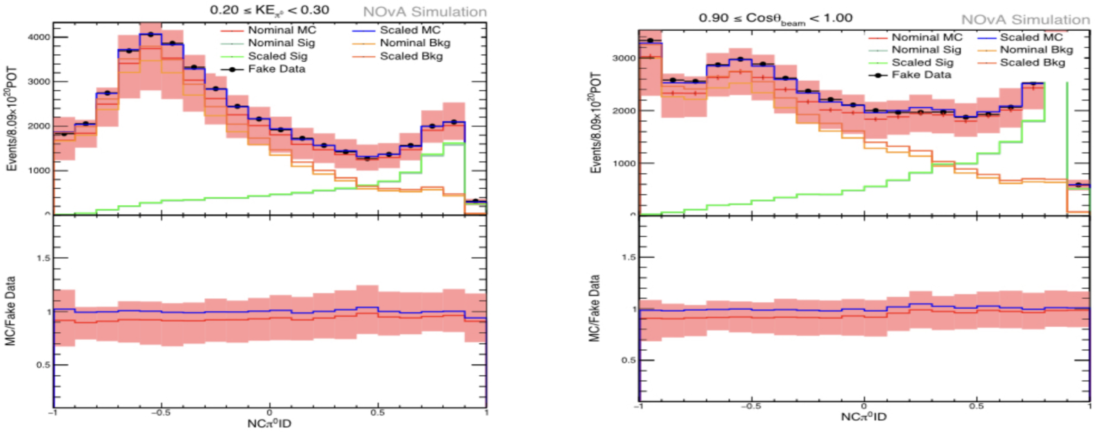

Figure 6.9: NC π^o ID distributions for the signal, background and total MC are shown in the first π^o K.E bin (left) and last π^o $cos\theta$ bin (right) before and after fit. The black points are for the background weighted fake-data sample.

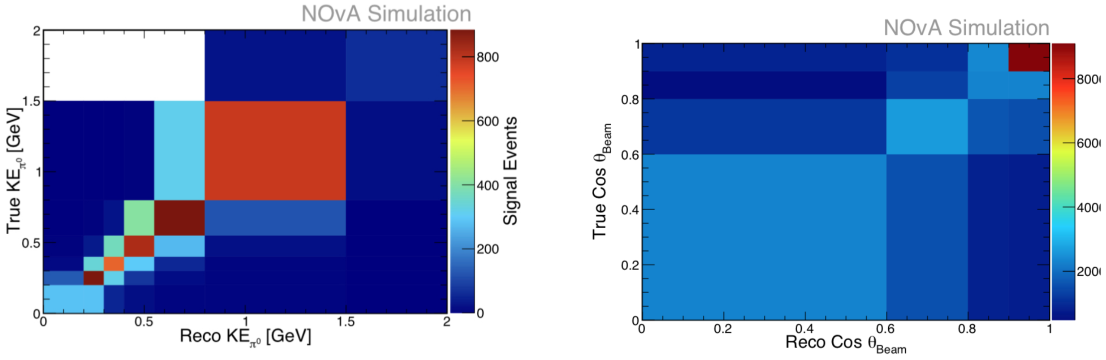

Figure 6.10: Figure shows the response matrices for π^o K.E (left) and π^o angle w.r.t beam (right).

number of iterations/regularization parameter.

$$\rho_j = \sqrt{1 - ((V_{xx})_{jj}(V_{xx})^{-1}_{jj})^{-1}} \tag{6.11}$$

where V_{xx} is a covariance matrix that takes covariance between truth bins into account. A characteristic curve for ρ_j similar to what is observed in [101] is seen for π^o K.E and π^o $cos\theta$ as shown in Figure 6.11. The more positive value of ρ introduces more smearing in the distribution. Therefore, to reduce the effect of the smearing we look for the minimum of this curve and is seen at 5 iterations for π^o K.E and 6 iterations for $cos\theta$. Unfolding is performed with the optimized number of iterations and results are shown in Figure 6.12. Here, statistically independent fake-data sample is used. In these distributions, black shows the background subtracted distribution and blue is the unfolded distribution which is then compared with the truth. Unfolded and truth distributions seem to match better. The results using various other fake-data samples are presented in [102].

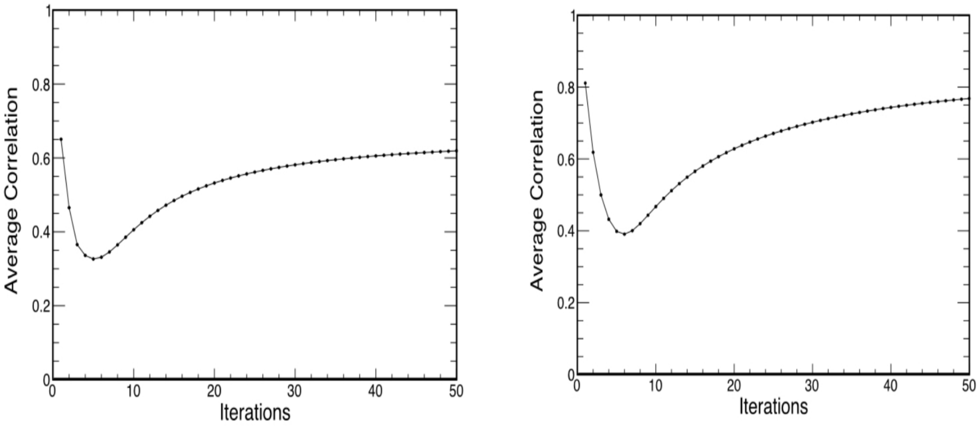

Figure 6.11: Figure shows average global correlation curve for π^o K.E (left) and π^o $cos\theta$ (right) with different number of iterations.

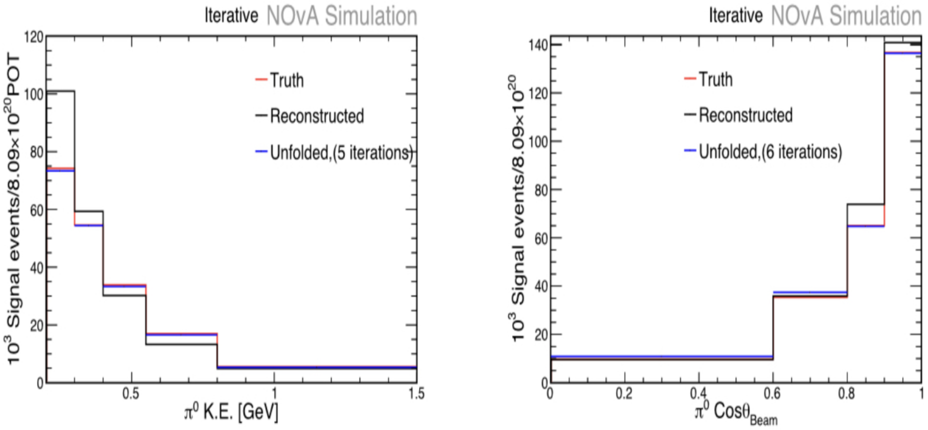

Figure 6.12: Figure compares the unfolded distributions (blue) to the truth distribution (red) for the π^o K.E (left) and $cos\theta$ (right). Also, the reconstructed variable distributions on which unfolding is done are shown (black).

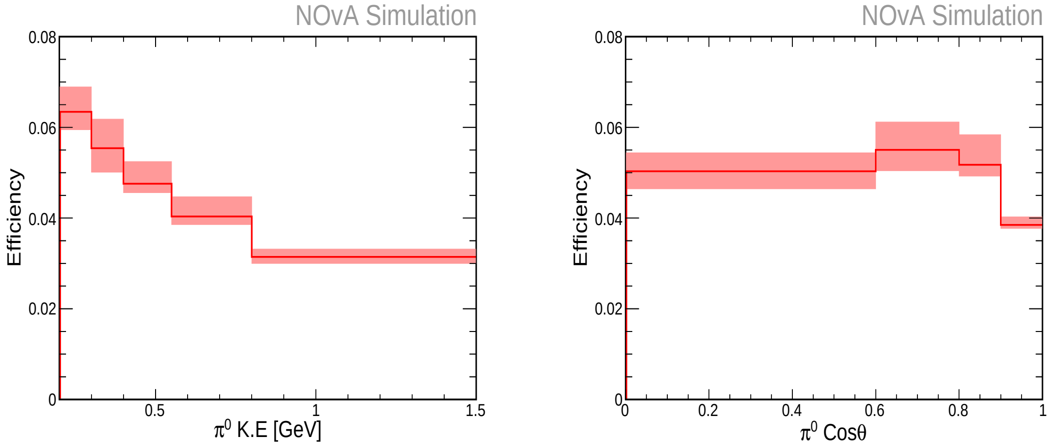

Figure 6.13: Efficiency of true signal events as a function of true K.E (left) and true $cos\theta$ (right). The systematic error band is with $\pm$ 1σ shift.

6.5 Efficiency Correction

The efficiency correction is applied to recover the true signal which is lost due to detector acceptance and selection cuts. Efficiency is defined as a ratio of true signal events after the pre-selection cuts to the true signal events in the true fiducial. Here, the denominator is NC interactions, in a true fiducial, with at least a π^o with true K.E $>$ 0.1 GeV whereas, the numerator term has an additional pre-selection cuts applied. We apply an efficiency correction to the unfolded signal estimate where the unfolding is done on the background subtracted signal estimate. Figure 6.13 shows the efficiency of true signal as a function of true K.E in left and true $cos\theta$ in right. The systematic error band is with $\pm$ 1σ shift.

6.6 Number of Target Nucleons

The cross-section measurement is reported as a cross-section per nucleon. The NOvA ND is not made up of a single material so the number of nucleons is determined in simulation using a random sampling within the specified fiducial volume. The algorithm generates "n 3D" points and for each sampling a point is selected and material is checked using the geometry files and mass of the rectangular volume is taken to be density of that material times volume. This is done 1 million times to get the true mass as consistent results were found using 10^6 to 10^9 points [104]. The results of the target count for the fiducial volume of this analysis are shown in Table 6.2. This gives a total mass of 55860 ± 387.304 kg. The statistical error is about 0.7% that comes from sampling the fiducial volume a finite number of times. The mass contributions from other material within the fiducial volume is shown in Table 6.3.

Table 6.2: The derived mass of fiducial volume by its atom type that is used to calculate the detector mass from Target Count

Element	Z	Fraction of Total Mass [kg]	Fraction of Total	Uncertainty [kg]
H	1	6019.27	0.107766	46.5799
C	6	37314.8	0.668065	304.377
N	7	14.4838	0.000259311	0.101469
O	8	1656.73	0.0296612	29.6912
Na	11	1.43978	2.57772e-05	0.0230366
S	16	53.2093	0.000952633	0.894056
Cl	17	8930.43	0.159886	143.528
Ca	20	14.5882	0.00026118	0.233411
Ti	22	1788.97	0.0320289	28.6236
Sn	50	66.1005	0.00118343	1.05761

Table 6.3: Mass contributions from different material within the fiducial volume.

Material	Density [g/cm^3]	Volume [cm^3]	Mass [kg]	Fraction of Total	Error in Mass[kg]
Air	0.001205	1.75707e+06	2.11727	3.79031e-05	0
Glue	0.98	404923	396.824	0.0071039	19.8412
PVC	1.4947	1.3548e+07	20250.1	0.362516	324.002
Scintillator	0.8576	4.10575e+07	35211	0.630343	211.266

6.7 Flux

This analysis uses an external package called “Package to Predict the FluX (PPFX) developed by the MINERvA Collaboration [88] to determine the flux for the NuMI beamline. PPFX determines the correction of the underlying hadronic model used in G4NuMI using all relevant data for the NuMI beam from external hadron production experiments. It also accounts for the correlation between neutrino types in any variable proportional to the neutrino yield. In the context of this analysis, the flux is calculated by inverting the standard cross-section equation.

$$\phi(E) = \frac{N(E)_{sig}}{N_{target}\frac{d\sigma(E)}{dE}} \tag{6.12}$$

where σ is the true cross section that GENIE records for every interaction it generates, N_{target} is the total number of targets in the fiducial volume, and N_{sig} is the total number of true signal interactions, weighted by PPFX, that occur within the fiducial volume. The derivation is discussed briefly in [105]. Figure 6.14 shows the results for the ν_μ and ν_e flux integrated in the NOvA ND using different fiducial volume than what is used in this analysis. The top plot shows the flux spectrum as corrected by PPFX. The error band corresponds to the hadron production and beam focusing systematics. The lower plot shows the ratio between the corrected flux over the prediction without any correction.

6.8 Systematic Uncertainties

Systematic uncertainties are addressed using systematically shifted simulation samples. The sources of systematic uncertainties include flux, neutrino-nucleus interactions and detector response. The cross-section is completely computed for each systematic shifted sample following the standard procedure that is discussed in this

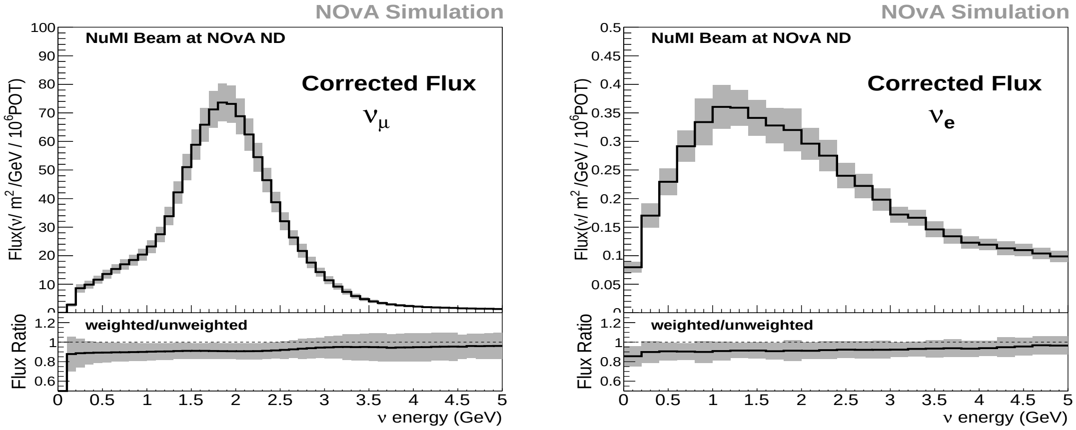

Figure 6.14: The ν_μ (left) and ν_e (right) flux integrated in the NOvA ND (-176 < X < 177 cm, -172 < Y < 179 cm and 25 < Z < 1150 cm). The band corresponds to the total beam uncertainty.

chapter.

- **Flux**: The systematic uncertainty on flux is determined by the PPFX. Figure 6.15 shows the hadron production fractional uncertainties for a muon neutrino in the NOvA ND. The total uncertainty is 8.1% around the peak region which is mainly due to the pions production when the primary proton beam hits the target, via nucleon interactions outside the target and interactions with incident mesons. An additional 4.7% uncertainty comes from the beam focusing [106]. The neutrino flux uncertainty is 9.4% in total. A detailed description is discussed in [88], [106].

- **Neutrino-nucleus interaction modeling**: Neutrino-nucleus interaction modeling uncertainties are determined using GENIE weights following a "multi-universe" approach [103]. It impacts the shape and normalization of both the signal and background distributions in each and every bin. In this analysis, we vary all the available GENIE parameters by $\pm1\sigma$ shift except the parameters for z-expansion modeling. The shifted spectra obtained from varying the GENIE parameters provide a $\pm1\sigma$ systematic error band. For each

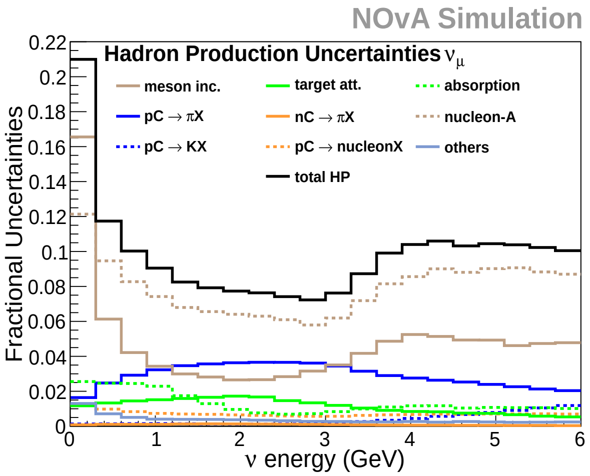

Figure 6.15: Figure shows the hadron production fractional uncertainties for a ν_μ in the NOvA ND.

universe, each GENIE parameter is shifted by a random fraction of sigma (generated from a normal distribution centered at zero) and the event is reweighted according to these shifts. A cross section is determined for each universe using the standard procedure discussed in this note. The multi-universe approach takes the correlations between all the universe into account allowing a consistent treatment of all the enabled GENIE parameters.

- **Detector response**: The uncertainties due to detector response include the uncertainties from calibration and light modeling. The systematic shifted simulation samples where the absolute energy scale is shifted up and down from their nominal values are used to assign uncertainty on the energy scale. In addition to normalization, these samples also include shape variation sample to consider the variation of calibrated energy response from being flat as a function of distance from the readout. Another contribution to detector response comes from light modeling. The scintillator response model includes cherenkov light production. The uncertainty on the light modeling comes from the uncertainty on overall light yield of the scintillator. These uncertainties are addressed using various systematic shifted samples.

The cross-section is calculated with each of the systematics to generate a systematic error band which determines the amount of uncertainty due to a particular systematic.

6.9 Flux Averaged Cross-section measurement

In this section, the flux averaged cross-section is measured using statistically independent fake-data sample. The standard cross-section equation as defined in equation 6.1 is:

$$\sigma = \frac{N^{sig}}{N_{Target}\phi\epsilon} \tag{6.13}$$

where, the number of signal events, N^{sig}, are estimated from the weighted NC π^o ID distribution for the signal events where the signal weights are obtained from the fit as described in section 6.1. The number of estimated signal events are 41321.6. In the denominator, the number of target nucleons are calculated in the fiducial volume and are 3.31×10^{31}, the neutrino flux is taken from 0 to 120 GeV and is $8.39 \times 10^{12}/cm^2/POT$ and then the efficiency correction is applied to the fake-data sample to recover the lost signal. The efficiency is calculated from the NC π^o ID distribution as the number of signal events after the pre-selection cuts divide by the total number of signal events in the fiducial volume and is 0.048. The flux averaged absolute cross-section with the fake-data sample comes out to be:

$$\sigma = 3.02 \times 10^{-39} cm^2/nucleons \tag{6.14}$$

The value is compared to the GENIE prediction for flux-averaged cross-section which is calculated using the same equation 6.13 except the efficiency correction term in denominator. For the GENIE prediction, the numerator is the integral taken from the true ν energy distribution. The number of target nucleons and flux is same. The

GENIE prediction for the flux-averaged absolute cross-section is:

$$\sigma = 2.77 \times 10^{-39} cm^2/nucleons \tag{6.15}$$

These values are compared in Figure 6.16. The NOvA neutrino flux is drawn with arbitrary units.

The same procedure will be used for measuring the cross-section using ND data.

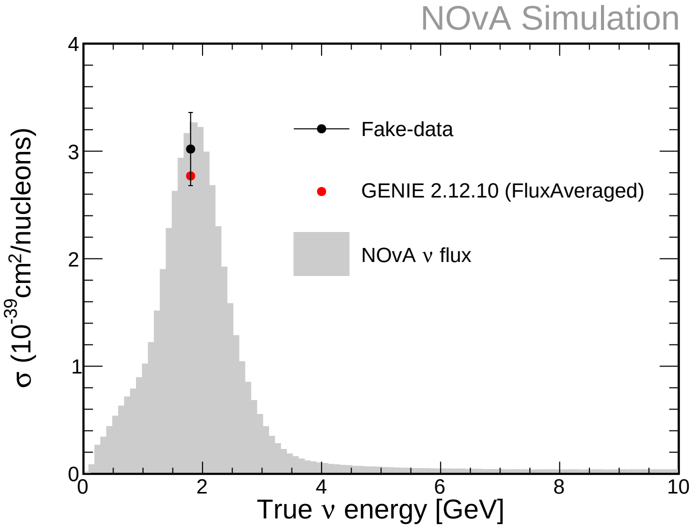

Figure 6.16: Figure compares the flux-averaged absolute cross-section for the GENIE prediction (Red) and statistically independent fake-data sample (Black) with the systematic uncertainty. The NOvA neutrino flux is drawn with arbitrary units

6.10 Differential Cross-section measurement

In this section, the differential cross-section w.r.t neutral pion kinematics is calculated in the analysis bins using equation 6.9. Here, again statistically independent fake-data sample is used. Figure 6.17 shows the differential cross-section w.r.t π^o K.E (left) and π^o $cos\theta$ (right). Red line in these figures is with the total MC, pink band represent $\pm 1\sigma$ systematic shift using all the systematics mentioned previously and black dots represent the cross-section in each of the analysis bins. Bottom panel shows the ratio of fake-data to total MC which stays close to 1.

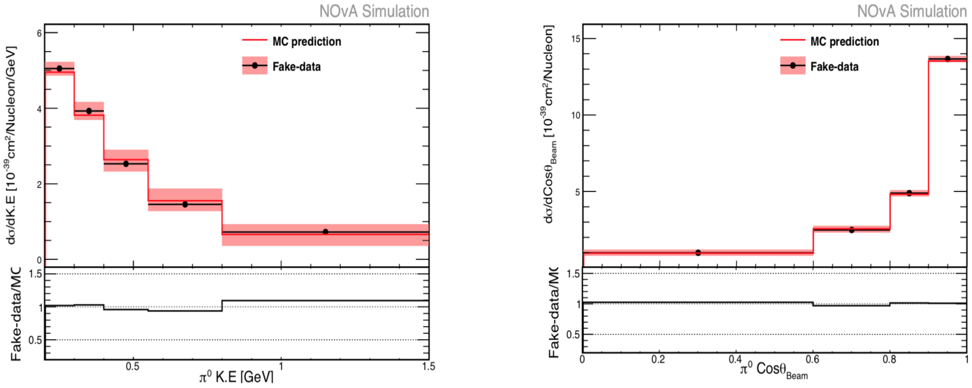

Figure 6.17: Differential cross-section is measured in analysis bins. Systematic error band includes all the systematics with ± 1 σ error. Bottom panel shows ratio of data to MC.

6.11 Measurements with the ND data

The detailed description of making an absolute and differential cross-section measurement w.r.t π^o kinematics using fake-data sample are given in the previous sections. In this section, the results with the ND data are shown. The template fit as is described in section 6.3 is performed using the ND data to determine the normalization of the signal, CC-background and NC-background components for the π^o K.E and π^o angle w.r.t beam direction. Figure 6.18 compares the ND data and MC distributions for π^o K.E (left) and angle (right). The error bars represent $\pm 1\sigma$ systematic error from the detector response, flux and cross section. The bottom panels in these distributions show the data to MC ratio.

The fit is performed in each of the analysis bins separately and completely independent of the neighboring bins as discussed in section 6.3. The weights obtained from the fit (as shown in Figures 6.19 and 6.20 for π^o K.E and π^o angle respectively)are then applied to the π^o K.E and π^o angle. Figure 6.21 compares the ND data and MC distributions for π^o K.E (left) and angle (right) with the weights applied. Ratio

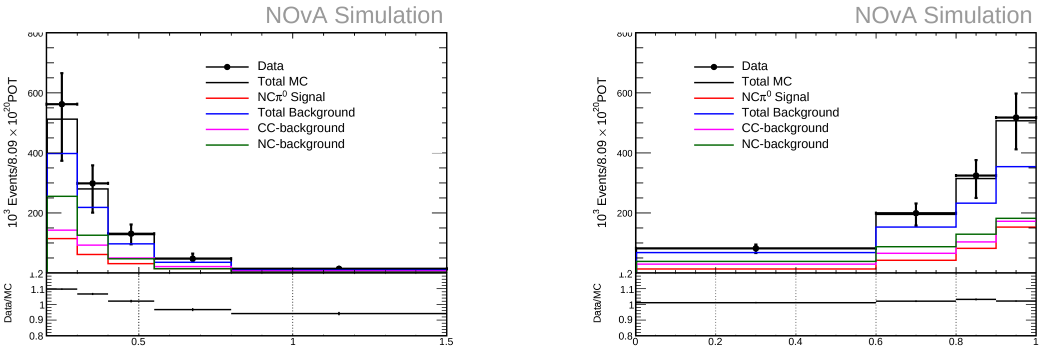

Figure 6.18: The distribution of events for π^o K.E (left) and π^o angle w.r.t beam (right) is shown in the analysis bins. The events in each bin are divided by the bin width.

plots are shown in the bottom panel of the distributions.

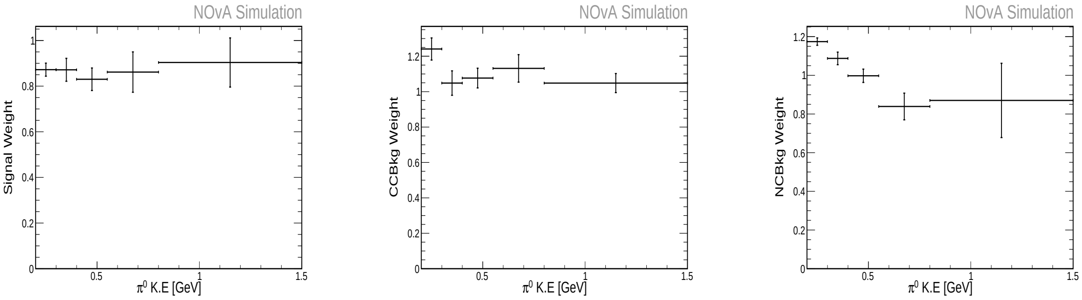

Figure 6.19: Figure shows the normalization of the signal like (left), CC-background like (middle) and NC-background like (right) components in π^o K.E bins.

.

The estimated signal obtained from the fit is unfolded to remove the detector effects. Figure 6.22 shows the distribution of π^o K.E (left) and angle (right) where, the signal estimate before and after unfolding is compared to the truth (true signal events at generator level). The events in each bin are divided by the bin width.

The unfolded signal estimate is used to compute the differential cross-section in π^o kinematics and is shown in Figure 6.23. Red line in these distributions represents the MC prediction and black dots are for the ND data in each bin. The error bars represent the statistical and $\pm 1\sigma$ systematic error. The bottom panel shows the ratio of data to MC. In all the energy bins and lower angle bins, MC over

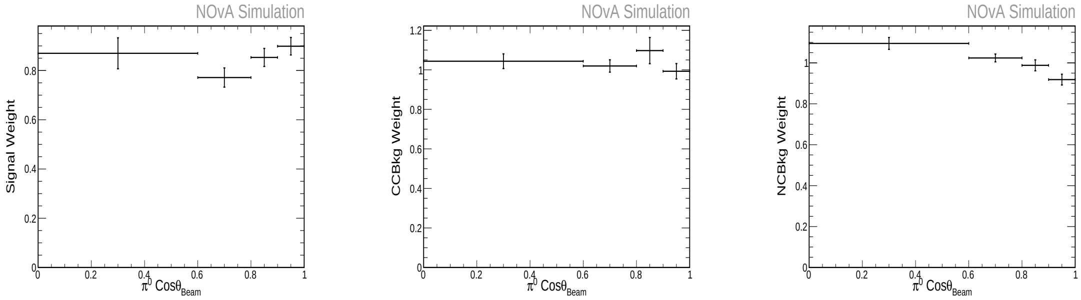

Figure 6.20: Figure shows the normalization of the signal like (left), CC-background like (middle) and NC-background like (right) components in π^o angle bins.

.

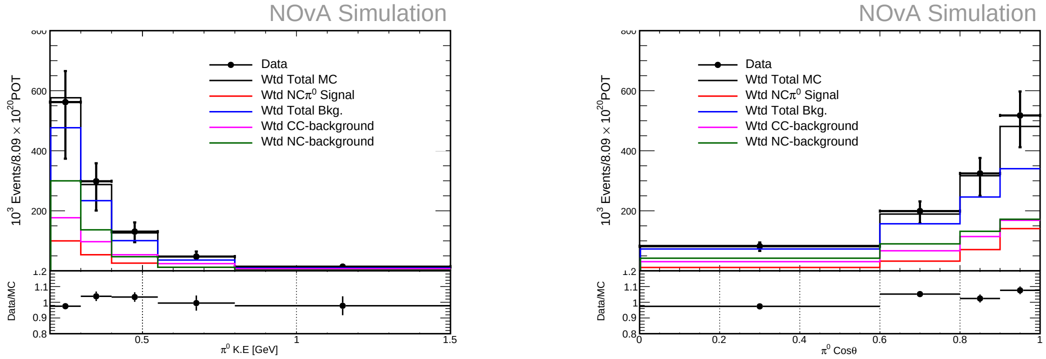

Figure 6.21: The distribution of events for π^o K.E (left) and π^o angle w.r.t beam (right) is shown in the analysis bins. The events in each bin are divided by the bin width.

predicts. However, in the higher angle bins MC under predicts. The differential cross-section with statistical and systematic uncertainties for π^o K.E bins and angle bins are reported in Tables 6.4 and 6.5 respectively.

Table 6.4: The differential cross section in each of the π^o K.E bins is reported along with statistical and systematic uncertainty.

K.E bin [GeV]	$\frac{d\sigma}{dK.E}$ $(10^{-39}cm^2/nucleon/GeV)$	Syst. unc.	Relative Syst. Unc.	Relative Stat. Unc.
0.2-0.3	4.46	± 0.36	8.2 %	1.1%
0.3-0.4	2.58	± 0.28	10.8%	1.4%
0.4-0.55	2.27	± 0.21	9.4%	1.4%
0.55-0.8	1.59	± 0.16	9.9%	1.6%
0.8-1.5	0.53	± 0.03	5.1%	1.7%

The overall uncertainties are within 5-15%.

Next, we also report the flux-averaged absolute cross section, the procedure of which

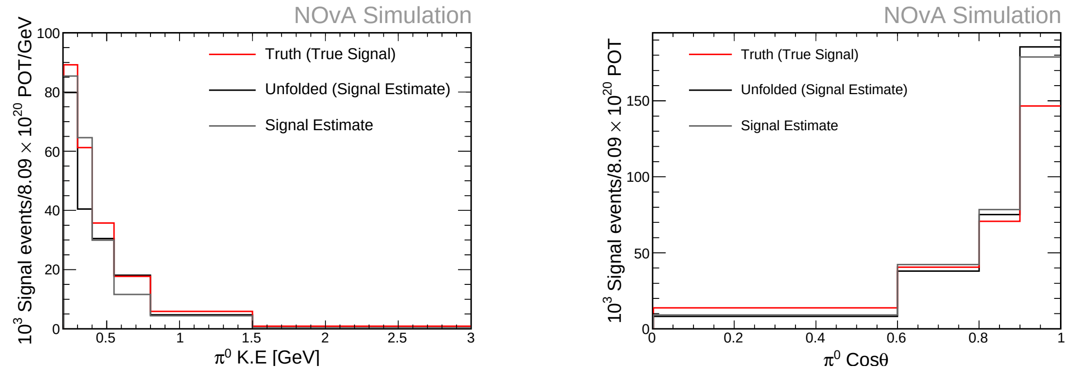

Figure 6.22: The distribution of estimated signal events before unfolding (Gray) and after unfolding (Black) is compared to the truth (Red) for π^o K.E (left) and π^o angle w.r.t beam (right). The events in each bin are divided by the bin width.

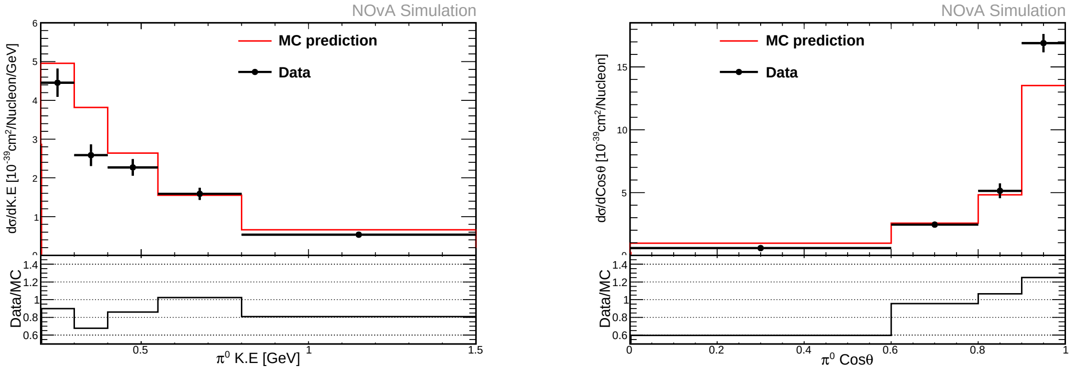

Figure 6.23: The differential cross-sections measured in the π^o K.E bins (left) and π^o angle bins (right).

is described in section 6.9. The flux-averaged cross section from the NOvA data is compared to the GENIE flux-averaged cross section and is shown in Figure 6.24.

$$\begin{gathered}\sigma(GENIE) = 2.77 \times 10^{-39} cm^2/nucleons \\ \sigma(NOvA) = (2.55 \pm 0.012(stat.) \pm 0.34(syst.)) \times 10^{-39} cm^2/nucleons\end{gathered} \tag{6.16}$$

The errors are the absolute statistical and systematic error. The statistical error is obtained from the number of estimated signal events and for calculating the systematic error, the cross-section is calculated with each of the systematic samples as described previously in this chapter.

Table 6.5: The differential cross section in each of the π^o angle bins is reported along with statistical and systematic uncertainty.

Angle bin	$\frac{d\sigma}{dcos\theta}$ $(10^{-39}cm^2/nucleon)$	Syst. unc.	Relative Syst. Unc.	Relative Stat. Unc.
0.0-0.6	0.57	± 0.04	7.7%	1.4%
0.6-0.8	2.44	± 0.25	10.1%	1.1%
0.8-0.9	5.14	± 0.58	11.4%	1.1%
0.9-1.0	17.05	± 0.73	4.3%	0.7%

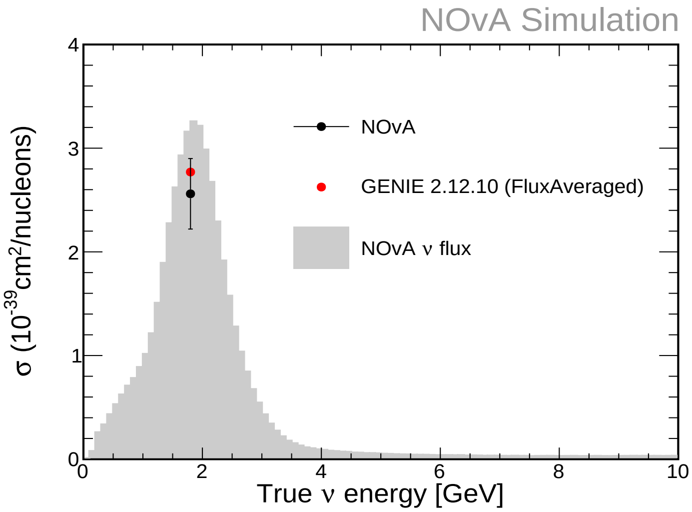

Figure 6.24: Flux-averaged cross-section measurement from the NOvA ND data (black point) is compared to the GENIE flux-averaged cross-section (red). The NOvA ν flux is shown in the same plot with arbitrary units.

6.12 Summary

In this chapter, the procedure required for making a cross-section measurement is discussed and is tested using various fake-data samples which gave reasonable results.

The differential cross-section measurements w.r.t π^o kinematics are reported. In all the energy bins and lower angle bins, MC over predicts. However, in higher angle bins, MC under predicts. The overall uncertainties are within 5-15%. The uncertainties in the analysis bins are dominated by the cross-section uncertainties (neutrino-nucleus interaction modeling) followed by the flux and detector response. The flux-averaged cross section is reported, $2.55 \pm 0.012(stat.) \pm 0.34(syst.)) \times 10^{-39} cm^2/nucleons$, which has the overall uncertainty ∼15%.

Chapter 7

Summary and Conclusions

The analysis done in this thesis is to measure the neutral current neutral pion (NC π^o) production cross section with the NOvA ND. NC interactions that produce π^o is an important background for the experiments looking for the ν_e appearance such as NOvA and next generation DUNE experiment. A 10% uncertainty on the NC background for the NOvA is dominated by π^o production cross section. So, it is very important to constrain this background. We have measured the flux-averaged absolute cross section for the NC π^o production channel as well as the differential cross section w.r.t neutral pion kinematics with uncertainties at a level of 5-15%.

$$\sigma(NOvA) = (2.55 \pm 0.012(stat.) \pm 0.34(syst.)) \times 10^{-39} cm^2/nucleons \tag{7.1}$$

The dominant source of uncertainty is from the neutrino-nucleus interaction modeling followed by the flux and detector response. The differential cross section measured in analysis bins, as shown in Figure 7.1, show differences between the data and MC but the measured absolute cross section matches with the MC prediction within the uncertainties.

Improvements in the systematics part of this measurement can be done to reduce the level of uncertainty to a few percent. One such improvement can be from the on-

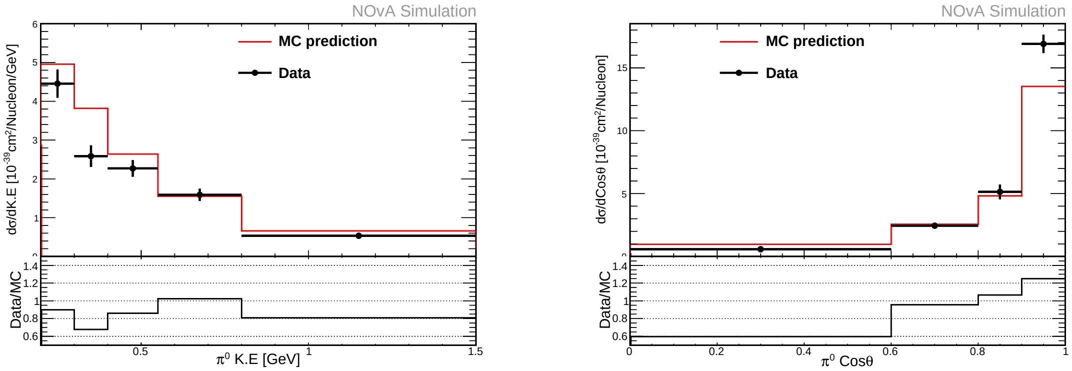

Figure 7.1: The differential cross-sections measured in the π^o K.E bins (left) and π^o angle bins (right).

going NOvA test beam studies where the uncertainties from the detector response can be reduced. Additionally, deep learning algorithms can be used to better identify the NC π^o events which is very important for measuring the cross section. Additionally, we have performed the simulation studies to optimize the neutrino and anti-neutrino event yield, by re-configuring the NOvA target and changing the horns position, for the off-axis NOvA detectors using G4NuMI simulation program. The studies have shown that the shorter target performs better than the standard NOvA target as it gives more neutrino and anti-neutrino yield for the NOvA detectors. The simulation results using G4NuMI are compared to the another simulator FLUGG. The comparison shows that the two simulation programs - G4NuMI and FLUGG predict different neutrino and anti-neutrino event yield which is further found to be connected to the difference in the pion production, that produce neutrinos and anti-neutrinos. Furthermore, we found that the target part that is situated close to the focusing system is 50% more efficient in producing neutrinos and anti-neutrinos as compared to the target part that is far away from the focusing system. These studies motivate for exploring a new target design which can further enhance the neutrino and anti-neutrino yield for the off-axis placed NOvA detectors. We have proposed a new design - Minimal NOvA target design that has shown increase in the neutrino and anti-neutrino event yield as compared to the standard NOvA target design. The gain in event yield is about 15% in comparison to the standard

NOvA event yield. The Minimal NOvA target design has been discussed with the target experts in Accelerator Division (AD) at Fermilab and they are carrying out the engineering studies for this new design.
Simulation studies required to upgrade the NOvA target are also performed along with the experts from AD. This upgrade is a part of Proton Improvement Plan that aims to increase the NuMI beam power from 700 kW to 1.2 MW. It is suggested to increase the width of the graphite fins in the target with increased beam spot size which is required to handle the increased beam intensity. Simulations are performed after modifying the fin width and beam spot size which show 3% reduction in the neutrino event yield as compared to the standard NOvA target which might be acceptable in comparison to the 30% increase in the beam power. Various other studies to upgrade the NOvA target in near future are currently going on.

The studies in this thesis are useful for the next generation long-baseline neutrino experiment such as DUNE. DUNE would be using the increased NuMI beam intensity so will be benefitted from the simulation studies of the standard NOvA target and new Minimal NOvA target design. Also, the information from the NC π^o production cross-section measurements can be used by neutrino community to better understand the underlying models in neutrino event generators. This will further improve the uncertainty on the oscillation measurements of the current and future long-baseline neutrino experiments.

Bibliography

[1] P. Hernandez, “Neutrino Physics-2013 TASI Lectures”, *[hep-ex] arXiv:1708.01046 (2017).*

[2] B. Pontecorvo, “Neutrino Experiments and the Problem of Conservation of Leptonic Charge”, *JETP Lett. 6 (1957) 429.*

[3] Luca Nanni, “Fermi theory of beta decay”, *[hep-ex] arXiv:1803.07147 (2018).*

[4] C. D. Ellis and W. A. Wooster, “The Continuous Spectrum of β-Rays”, *Nature 119 (1927) 563-564.*

[5] Wolfgang Pauli, “Letter to the physical society of Tubingen”, *Physics Today, vol.9 (1930).*

[6] E. Fermi, “Trends to a Theory of beta Radiation. (An Italian)”, *Nuovo Cim., vol. 11 (1934) p.1.*

[7] David Griffiths, “Introduction to Elementary Particles”, *(WILEY-VCH Verlag GmbH and Co. KGaA).*

[8] H. Bethe and R. Peierls, “The neutrino”, *Nature, vol. 133 (1934) p. 532.*

[9] B. Pontecorvo, “Inverse beta process”, *Camb. Monogr. Part. Phys. Nucl. Phys. Cosmol., vol. 1 (1991) p.25.*

[10] F. Reines and C. L. Cowan, “The neutrino”, *Nature, vol. 178 (1956) p.446.*

[11] C. L. Cowan, F. Reines, F. B. Harrison, H. W. Kruse, and A. D. McGuire, "Detection of the free neutrino: A Confirmation", *Science, vol. 124 (1956) p.103.*

[12] G. Danby et al., "Observation of High-Energy Neutrino Reactions and the Existence of Two Kinds of Neutrinos", *Phys.Rev.Lett. 9 (1962) 36.*

[13] K. Kodama et al., "Observation of tau neutrino interactions", *Phys.Lett. B504 (2001) 218.*

[14] K. Hirata et al., "Observation of a neutrino burst from Supernova SN1987A", *Phys.Rev.Lett. 58 1490 (1987).*

[15] R. M. Bionta et al., "Observation of a neutrino burst in coincidence with supernova 1987A in the Large Magellanic Cloud", *Phys.Rev.Lett. 58 (1987) 1494.*

[16] M. Tanabashi et al., "Particle Data Group", *Phys.Rev. D98 (2018) 030001.*

[17] S. Schael et al., "Precision electoweak measurements on the Z resonance", *Phys.Rept. 427 (2006) 257.*

[18] E. Graverini, "Heavy Neutrino Searches from MeV to TeV", *[hep-ex] arXiv:1611.07215v1 (2016).*

[19] K. A. Olive et al., "Review of Particle Physics", *Chin.Phys. vol. C38 (2014) p.090001.*

[20] K. Assamagan et al., "Upper limit of the muon-neutrino mass and charged pion mass from momentum analysis of a surface muon beam", *Phys.Rev. vol. D53 (1996) 6065.*

[21] R. Barate et al., "An Upper limit on the tau-neutrino mass from three-prong and five-prong tau decays", *Eur.Phys. J. vol. C2 (1998) 395.*

[22] Samoil Bilenky, "Introduction to the Physics of Massive and Mixed Neutrinos", *(Springer Publishing) (1969).*

[23] L. Cardani, "Neutrinoless Double Beta Decay Overview", *[hep-ex] arXiv:1810.12828 (2018).*

[24] S. P. Mikheyev and A. Yu. Smirnov, *Proc. of the 6th Moriond Workshop on massive Neutrinos in Astrophysics and Particle Physics, Tignes, Savoie, France Jan. 1986 (eds. O. Fackler and J. Tran Thanh Van) (1986) p.355.*

[25] R. Leitner, on behalf of the Daya Bay collaboration, "Recent results of the Daya Bay reactor neutrino experiment", *Nuclear and Particle Physics Proceedings, (2017) 285.*

[26] Y. Abe et al.., "Improved measurements of the neutrino mixing angle θ_{13} with the Double Chooz detector", *[hep-ex] arXiv:1406.7763 (2014).*

[27] Soo-Bong Kim, "New Results from RENO and Prospects with RENO-50", *[hep-ex] arXiv:1412.2199 (2014).*

[28] M. H. Ahn et al. (K2K Collaboration), *Phys.Rev. D74 (2006) 072003.*

[29] P. Adamson et al. (MINOS Collaboration), *Phys.Rev.Lett. 112 (2014) 191801.*

[30] K. Abe et al. (T2K Collaboration), *Phys.Rev. D91 (2015) 072010.*

[31] M. A. Acero et al. (NOvA Collaboration), *Phys.Rev. D98 (2018) 032012.*

[32] Kevin McFarland, "Neutrino Interactions", *[hep-ex] arXiv:0804.3899 (2008).*

[33] H. Hassanabadi, A. Armat, L. Naderi, "Relativistic Fermi-Gas Model for Nucleus", *DOI: 10.1007/s 10701-014-9836-7 (2014).*

[34] A. Bodek, M. E. Christy, B. Coopersmith, "Effective Spectral Function for Quasielastic Scattering on Nuclei", *Eur.Phys.J. C74 (2014) no.10, 3091.*

[35] R. Shneor at al., “Investigation of proton-proton short-range correlations via the C-12(e, e-prime pp) reactions”, *Phys.Rev.Lett. 99 (2007) 072501.*

[36] C. Andreopoulos et al., “The GENIE Neutrino Monte Carlo Generator”, *[hep-ex] arXiv:1510.05494 (2015).*

[37] D. Pershey, *NOVA Internal document 30291 (2018).*

[38] D. Rein and L. M. Sehgal, “Neutrino-excitation of baryon resonances and single pion production”, *Ann.Phys. (NY) 133 (1981) 79.*

[39] Janet M. Conrad et al., “Precision Measurements with High Energy Neutrino Beams”, *[hep-ex] arXiv:hep-ex/9707015 (1997).*

[40] J.A. Formaggio, G.P. Zeller “From eV to EeV: Neutrino Cross Sections Across Energy Scales”, *[hep-ex] arXiv:1305.7513 (2013).*

[41] D. Rein and L. M. Sehgal, “PCAC and the deficit of forward muons in π^+ production by neutrinos,” *Phys.Lett. vol. B657 (2007) 207.*

[42] S. J. Barish et al., “Observation of Single-Pion Production by a Weak Neutral Current”, *Phys.Rev.Lett. 33 (1974) 448.*

[43] M. Derrick et al., “Study of single-pion production by weak neutral currents in low-energy νd interactions”, *Phys.Rev. D23 (1981) 569.*

[44] E. A. Hawker, submitted to NuInt’02 proceedings, to be published in Nucl. Phys. B Proc. Suppl.

[45] W. Krenz et al., “Experimental Study of Exclusive one-pion production in all neutrino-induced neutral current channels”, *Nucl.Phys. B135 (1978) 45.*

[46] S.Nakayama et al., (K2K Collaboration) *[hep-ex] arXiv:hep-ex/0408134 (2014).*

[47] Y. Kurimoto et al., (SciBooNE Collaboration) *[hep-ex] arXiv:0910.5768 (2010).*

[48] A. A. Aguilar-Arevalo et al., (MiniBooNE Collaboration) *[hep-ex] arXiv:0911.2063*, *Phys.Rev. D81 (2010) 013005.*

[49] K. Abe et al., (T2K Collaboration) *Phys.Rev. D97 (2017) 032002.*

[50] P. Adamson et al., (MINOS Collaboration) *Phys.Rev. D77 (2008) 072002.*

[51] L. Fields et al., (MINERvA Collaboration) *Phys.Rev.Lett. 111 (2013) 022501.*

[52] C. Anderson et al., (ArgoNeuT Collaboration) *Phys.Rev.Lett. 108 (2012) 161802.*

[53] A Proposal to FNAL to run MINOS with the Medium Energy NuMI beam, *Internal MINOS document 7923 (2011)*, *Fermilab Proposal P1016, 2011.*

[54] The NOvA Technical Design Report, (2007).

[55] P. Adamson et al., "The NuMI Neutrino Beam", *[hep-ex] arXiv:1507.06690 (2015).*

[56] Srubabti Goswami and Newton Nath, "Implications of the latest NOvA results", *[hep-ex] arXiv:1705.01274 (2017).*

[57] Eric Lewis Flumerfelt, "DAQ Software Contributions, Absolute Scale Energy Calibration and Background Scale Evaluation for the NOvA Experiment at Fermilab", *DOI: 10.2172/1221342 (2015).*

[58] C. Backhouse, A. Radovic and P. Singh, "Calibration Technical Notes", *NOVA Internal document 13579 (2018).*

[59] S. Agostinelli et al. (GEANT4 Collaboration), *Nucl.Instrum.Meth. A506 (2003) 250.*

[60] L. Aliaga et al. (MINERvA Collaboration), *Phys.Rev. D94 (2016) 092005.*

[61] K. Bays, A. Mislivec, G. Pawloski, J. Wolcott, “NOvA 2018 cross-section tune tech note”, *NOVA Internal document 27755 (2018).*

[62] Hagmann C, Lange D and Wright D, *2007 Nuclear Science Symp. Conf. Rec. (Honolulu, HI) vol 2 (IEEE) pp 1143-1146.*

[63] A. Aurisano, “The NOvA Detector Simulation”, *NOVA Internal document13577 (2015).*

[64] Rene Brune, “ROOT Data Analysis Framework”. *[Online]. Available at http://root.cern.ch.*

[65] M. Baird, “Slicing Module Comparison Technical Note”, *NOVA Internal document 9195 (2013).*

[66] Duda, R. O. and P. E. Hart, “Use of the Hough Transformation to Detect Lines and Curves in Pictures”, *Comm. ACM, Vol. 15 (1972) pp.11-15.*

[67] M. Baird, “Global Vertex Reconstruction beginning with a Modified Hough Transform”, *NOVA Internal document 8241 (2012).*

[68] Mark D. Messier, “Vertex Reconstruction Based on Elastic Arms”, *NOVA Internal document 7530 (2012).*

[69] E. Niner, “Vertex Clustering with Possibilistic Fuzzy-K Means Algorithm”, *NOVA Internal document 7648 (2012).*

[70] Nicholas J Raddatz, “KalmanTrack Technical Note”, *NOVA Internal document 13545 (2015).*

[71] A. Aurisano et.al, “A convolutional neural network neutrino event classifier”, *J.Instrum. 11 (2016) P09001.*

[72] P. Adamson et al., (NOvA Collaboration), *Phys.Rev.Lett 118 (2017) no.23, 231801.*

[73] D. Ayres et al, *NOvA Proposal to Fermilab (2005).*

[74] D. Ayres et al., "NOvA Conceptual Design Report", *NOVA Internal document 536 (2006).*

[75] P. Adamson et al., *[hep-ex] arXiv: 1601.05022v1*, also as *FERMILAB-PUB-15-262-ND (2016).*

[76] J. Hylen, *NOvA Internal document 3453 (2009).*

[77] T. Bohlen et al., "The Fluka Code", *Nuclear Data Sheets vol. 120 (2014) pp. 211-214.*

[78] A. Ferrari, P.R. Sala, A. Fasso, and J. Ranft, "FLUKA: a multi-particle transport code" *CERN-2005-10 (2005).*

[79] Geant4 Collaboration, "Toolkit Developers Guide". *[Online]. Available at http://cern.ch/geant4.*

[80] S. Agostinelli et al., *Nuclear Instruments and Methods A506, 250 (2003), and IEEE Transaction on Nuclear Science vol 53, page 270 (2006).*

[81] Daisy Kalra, John W. Cooper, G. Brunetti and J. Tripathi, "NuMI off Axis Beam Studies for NOvA - Part I", *NOVA document 16233 (2017).*

[82] Daisy Kalra, John W. Cooper, G. Brunetti and J. Tripathi, "NuMI off Axis Beam Studies for NOvA - Part II", *NOVA document 16233 (2018).*

[83] D. Kalra, *NOVA Internal document 13193-v2 (2015).*

[84] D. Kalra, *NOVA Internal document 13767 (2015).*

[85] D. Kalra, *NOVA Internal document14033 (2015).*

[86] D. Kalra, *NOVA Internal document 17921 (2017).*

[87] D. Kalra, *NOVA Internal document 30876 (2018).*

[88] L. Aliaga, "NuMI Beam Prediction for the NOvA 2017 Analyses", *NOVA Internal document 23441 (2017).*

[89] K. Bays, A. Mislivec, G. Pawloski, J. Wolcott, "NOvA 2018 cross-section tune tech note", *NOVA Internal document 27755 (2018).*

[90] J. Wolcott and K. Bays, "Cross section central value tune and uncertainties for the 2017 analyses", *NOVA Internal document 23264 (2017).*

[91] J. Wolcott, H. Gallagher, T. Olson and T. Mann, "GENIE central value tune and uncertainties for Second Analysis", *NOVA Internal document 15214 (2017).*

[92] D. Kalra, "Technical note on NC π^0 cross-section measurement", *NOVA Internal document 36381 (2018).*

[93] N. Raddatz, "ReMId Technical Note", *NOVA Internal document 11206 (2014).*

[94] A. Hoecker, P. Speckmayer, J. Stelzer, J. Therhaag, E. von Toerne, H. Voss, "TMVA - Toolkit for Multivariate Data Analysis", *[hep-ex] arXiv:0911.2063 (2009).*

[95] A. Aurisano et al., "A convolutional Neural Network Neutrino Event classifies", *[hep-ex] arXiv:1604.01444 (2016).*

[96] D. Kalra, *NOVA Internal document 18402 (2017).*

[97] D. Kalra, *NOVA Internal document 22034 (2017).*

[98] D. Kalra, *NOVA Internal document 24119 (2017).*

[99] D. Pershey, *NOVA Internal document 25089 (2017).*

[100] D. Kalra, *NOVA Internal document 30396 (2018)*.

[101] Stefan Schmitt, "Data Unfolding Methods in High Energy Physics", *[hep-ex] arXiv:1611.01927 (2016)*.

[102] D. Kalra, *NOVA Internal document 30591 (2018)*".

[103] Shih-Kai Lin, "GENIE Systematic Uncertainties with the Multi-universe approach in CAFAna", *NOVA Internal document 21635 (2017)*.

[104] K. Sachdev, *NOVA Internal document 15787 (2016)*.

[105] C. Backhouse, "Derivation of flux", *NOVA Internal document 15910 (2016)*.

[106] L. Aliaga, *FERMILAB-THESIS-2016-03*.

Chapter 7

Summary and Conclusions

The analysis done in this thesis is to measure the neutral current neutral pion (NC π^o) production cross section with the NOvA ND. NC interactions that produce π^o is an important background for the experiments looking for the ν_e appearance such as NOvA and next generation DUNE experiment. A 10% uncertainty on the NC background for the NOvA is dominated by π^o production cross section. So, it is very important to constrain this background. We have measured the flux-averaged absolute cross section for the NC π^o production channel as well as the differential cross section w.r.t neutral pion kinematics with uncertainties at a level of 5-15%.

$$\sigma(NOvA) = (2.55 \pm 0.012(stat.) \pm 0.34(syst.)) \times 10^{-39} cm^2/nucleons \tag{7.1}$$

The dominant source of uncertainty is from the neutrino-nucleus interaction modeling followed by the flux and detector response. The differential cross section measured in analysis bins, as shown in Figure 7.1, show differences between the data and MC but the measured absolute cross section matches with the MC prediction within the uncertainties.

Improvements in the systematics part of this measurement can be done to reduce the level of uncertainty to a few percent. One such improvement can be from the on-

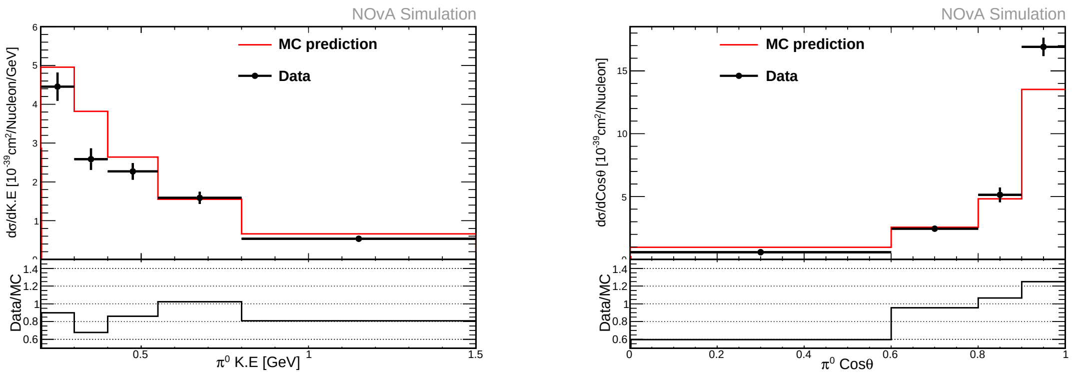

Figure 7.1: The differential cross-sections measured in the π^o K.E bins (left) and π^o angle bins (right).

going NOvA test beam studies where the uncertainties from the detector response can be reduced. Additionally, deep learning algorithms can be used to better identify the NC π^o events which is very important for measuring the cross section.

Additionally, we have performed the simulation studies to optimize the neutrino and anti-neutrino event yield, by re-configuring the NOvA target and changing the horns position, for the off-axis NOvA detectors using G4NuMI simulation program. The studies have shown that the shorter target performs better than the standard NOvA target as it gives more neutrino and anti-neutrino yield for the NOvA detectors. The simulation results using G4NuMI are compared to the another simulator FLUGG. The comparison shows that the two simulation programs - G4NuMI and FLUGG predict different neutrino and anti-neutrino event yield which is further found to be connected to the difference in the pion production, that produce neutrinos and anti-neutrinos. Furthermore, we found that the target part that is situated close to the focusing system is 50% more efficient in producing neutrinos and anti-neutrinos as compared to the target part that is far away from the focusing system. These studies motivate for exploring a new target design which can further enhance the neutrino and anti-neutrino yield for the off-axis placed NOvA detectors. We have proposed a new design - Minimal NOvA target design that has shown increase in the neutrino and anti-neutrino event yield as compared to the standard NOvA target design. The gain in event yield is about 15% in comparison to the standard

NOvA event yield. The Minimal NOvA target design has been discussed with the target experts in Accelerator Division (AD) at Fermilab and they are carrying out the engineering studies for this new design.
Simulation studies required to upgrade the NOvA target are also performed along with the experts from AD. This upgrade is a part of Proton Improvement Plan that aims to increase the NuMI beam power from 700 kW to 1.2 MW. It is suggested to increase the width of the graphite fins in the target with increased beam spot size which is required to handle the increased beam intensity. Simulations are performed after modifying the fin width and beam spot size which show 3% reduction in the neutrino event yield as compared to the standard NOvA target which might be acceptable in comparison to the 30% increase in the beam power. Various other studies to upgrade the NOvA target in near future are currently going on.

The studies in this thesis are useful for the next generation long-baseline neutrino experiment such as DUNE. DUNE would be using the increased NuMI beam intensity so will be benefitted from the simulation studies of the standard NOvA target and new Minimal NOvA target design. Also, the information from the NC π^o production cross-section measurements can be used by neutrino community to better understand the underlying models in neutrino event generators. This will further improve the uncertainty on the oscillation measurements of the current and future long-baseline neutrino experiments.